

AD707151

AFCRL-70-0224

EXPLODING WIRE PHENOMENA

by

Theodore Korneff

William Simmons

Herbert Goronkin

Physics Department

Temple University

Philadelphia, Pennsylvania 19122

Contract No. F19628-67-C-0250

Project No. 8608

Task No. 860804

Unit No. 86040401

FINAL REPORT

Period Covered: 1 March, 1967 through 28 February, 1970

March 31, 1970

Contract Monitor: Allen G. Rubin

Space Physics Laboratory

This document has been approved for public
release and sale; its distribution is unlimited

Prepared

for

AIR FORCE CAMBRIDGE RESEARCH LABORATORIES

OFFICE OF AEROSPACE RESEARCH

UNITED STATES AIR FORCE

BEDFORD, MASSACHUSETTS 01730

07-20-1968

DATE _____
C _____

ALL INFORMATION CONTAINED HEREIN IS UNCLASSIFIED
DATE 07-20-1968 BY SP-6 [redacted]

DIST.

Qualified requestors may obtain additional copies from the Defense Documentation Center. All others should apply to the Clearinghouse for Federal Scientific and Technical Information.

ABSTRACT

This report describes:

- A. Experiments to determine the shunting effect of occluded and self-generated vapor produced by an exploding wire in a vacuum.
- B. The investigation of the striation mechanism in exploding wires. These striations have been examined by high speed sequential frame cameras to see if they have an axial drift.
- C. Calculations on the order of magnitude of the Hall energy. Results show that for a given sample, about 13% more energy is required to melt the sample than is accounted for in simple thermodynamic arguments.
- D. The development of an experimental flash x-ray technique for determining the instantaneous density of the vapor produced by an exploding wire.
- E. The development of a 3-color optical pyrometer with fast response time. The unit, in bread-board form, has been calibrated, and used to obtain preliminary results from exploding wires. The results are expressed in the form of a trace on a cathode ray oscilloscope whose vertical displacement is proportional to the temperature.

T. Korneff
W. Simmons
H. Goronkin

II

TABLE OF CONTENTS

	PAGE
ABSTRACT.....	I
INTRODUCTION.....	1
CURRENT DISTRIBUTION IN A VACUUM.....	2
STRIATIONS IN EWP.....	3
HALL ENERGY IN EXPLODING WIRES.....	5
Introduction	5
Theory.....	7
Results.....	13
References.....	14
X-RAY MEASUREMENTS ON VAPOR DENSITY IN EWP.....	15
Introduction.....	15
Experimental Goals.....	16
Experimental Procedure.....	16
Description of Results.....	20
Tin Wire.....	21
Copper Wire.....	22
Gaussian Expansion.....	23
Conclusions.....	26
References.....	28
List of Illustrations.....	30
THREE-COLOR OPTICAL PYROMETER.....	56
Introduction.....	56
Discussion of Method.....	56
Circuit Theory and Calibration.....	57
Results.....	60
Table I.....	62
Table II.....	63
References.....	64
List of Illustrations.....	65
APPENDIX I No. 26 Cu Wire- 7kV Density Curves.....	80
APPENDIX II No. 18 Tin Wire- 7kV Density Curves.....	90
APPENDIX III No. 18 Tin Wire- 10kV Density Curves.....	102
APPENDIX IV Equipment Setup For Vapor Density Measurements....	114
APPENDIX V Related Contracts and Publications.....	119

INTRODUCTION

This report describes the scope of the work undertaken at the Temple University Physics Department under contract F19628-67-0250 covering the period March 1, 1967 to February 28, 1970. The main effort was to investigate the feasibility of determining the instantaneous vapor density of the expanding cylinder of gas produced in an exploding wire experiment.

Also, investigations were pursued on the shunting effect of copper vapor at reduced pressures; the striation mechanism; energy considerations in the initial prevaporization stages of the explosion; and the completion, calibration, and preliminary use of an electronic 3-color optical pyrometer. The research resulted in several papers being reported at pertinent conferences, publications in scientific journals and books, and a student thesis. Material not reported before, or published in condensed form will be presented and expanded upon in this report the bibliography included with this report is not intended to be all inclusive. For more detailed bibliographies, one should consult the pertinent references.

CURRENT DISTRIBUTION IN A VACUUM

This investigation explores the current sheath surrounding an exploding copper wire in a vacuum. For such a case, a sheath of plasma appears around the wire at a very early stage of the explosion. Together with the ionization of the ambient atmosphere, this develops into a cylinder of highly conductive vapor. This effect, which is responsible for the disappearance of the dwell at low pressures, shunts a large part of the total discharge current. In this present investigation (Ref. 1, 2, and 3), the spatial distribution of the current at various stages of the explosion is studied by means of the Rogonski coil method. Details on coil construction and calibration are found in Ref. 2. In the past, researchers have tacitly assumed that the current density is proportional to the brightness of the image, as seen in high speed optical cameras. This is not necessarily valid. We have compared framing camera studies with simultaneous Rogonski coil studies and have found the the intensity of the radiation does not correspond to the current density for the low pressure cases. The current expands much faster than the image (Ref. 1, 2). The results can be summarized as follows:

- (1) there is no expansion of current before the transposition point, which is indicated by the notch in the total current waveform.
- (2) for copper wire ($l = 4$ cm, $r = 0.02$ cm) exploded at a pressure of 1 micron, the expansion rate for the leading edge of the current distribution was 10^5 to 10^6 cm/sec.
- (3) radial expansion decreases as the pressure increases.
- (4) the current distribution is not necessarily proportional to the brightness of the photographic image of the exploding wire. At low pressure, the current distribution expands faster than the image.
- (5) the current distribution does not reduce to zero as the total current goes to zero. There appears to be an inverse skin effect, much like that described by Haines (Ref. 11).

STRIATIONS IN EWP

Striations in exploding wires have been examined in sequential frame studies to investigate the possibility that gas discharge type striations are formed in the electron-vapor sheath (Ref. 4,5). These electrical striations, due to localized space charge formed by impact, move in the direction of majority electric current carrier motion. Explosions were carried out on samples immersed in distilled water in order to impede outgassing which could mask striations. No. 28 copper wire samples in 1 and 2 cm lengths were connected across a 45 microfarad capacitor bank charged from 3 kV to 8 kV. The striation formation may be mechanical or electrical. Mechanical processes would be based on material separation or imperfections, either in the bulk or on the surface. Electrical processes would be based upon the interaction of large surface currents or thermally generated sheath currents interacting with metal vapor or liquid. For the mechanical case, striations would be visible by virtue of ionized gasses at "hot spots." For the electrical case, striations would be visible by metal atom recombination radiation. Electrical striations have one striking property which distinguishes them from mechanical striations. The diffusion of the carriers is ambipolar. Thus, if electrons dominate, the striations will move toward the anode, while they will drift toward the cathode if ion concentration dominates. A high speed framing camera was used to supply ten photographs taken at intervals of 0.45 microseconds, for each explosion. Within the range of electrical fields used in this experiment, no movement of striations was observed. An experiment was designed to bring out the possible nature of mechanical striations. Copper wire was annealed in a nitrogen-hydrogen atmosphere at 700°C for 2 hours and slow-cooled at the rate of 100°C/hr. Control wires (unannealed) and test wires (annealed) were compared by etching the surfaces and inspection showed that the annealing has substantially reduced grain boundary density. There are fewer striations, on the average, for the annealed wires than the control wires.

The results of this investigation are that it is not likely that low velocity electrical striations are present, and that the existence of mechanical striations has been firmly established.

HALL ENERGY IN EXPLODING WIRES

I. Introduction

The energy deposited in an electrically exploded wire is determined from the current through the wire, the voltage across the wire, and the circuit inductance. When the energy residing in the wire is measured, it is found that more energy has been delivered than is required to melt the sample.^(r) So the question is raised as to the need for an extra amount of energy to melt the wire when it is heated by large current densities.

The experimental situation by which large currents are "dumped" into the wire results in times to melt on the order of microseconds. The short periods of time involved might suggest the possibility of a thermal lag to account for the observed melting after an excess energy has been delivered. Inertial effects of this type are characterized by a thermal time constant which is the time for a thermal instability to decay to 0.37 of its original value. In normal pure metals this relaxation time is on the order of 10^{-11} sec.^(r) Compared to the microseconds required to melt the sample it can be concluded that the thermal current is in equilibrium with the applied fields and there can be no thermal lag.

It might be argued that the energy discrepancy can be explained by nonuniform heating across the specimen cross-section due to the transient skin effect. In such a case the large density of electrons near the surface would result in local rapid heating while the interior remained cooler due to the relative scarcity of energetic charge carriers. Haines^(r) has shown that for the transient skin effect to be important, the natural period of the discharge circuit must be on the order of the time $\frac{\mu \sigma a^2}{18}$, μ is the permeability, σ is the conductivity and a is the sample radius. In this characteristic time, less than 10^{-7} sec., for the samples examined below, surface currents diffuse into the interior, so this effect is also not appreciable.

Attempts have been made to explain the energy unbalance by considering the sample resistance change with time due to increasing temperature.^(r) In general, this method assumes a form for the temperature dependence of resistance and solves the discharge circuit equations for the current as a function of time. By casting the current function into a power series in time and subtracting the series elements elements associated with a non-exploding low resistance sample, the response of the sample to the discharge is obtained. Results thus obtained show general correlation with experiment but still fail to account for all the energy delivered to the wire. Implicit in such arguments is that the measured energy excess is not real, i.e., by determining the correct behavior of the wire resistance with time and temperature, and from it, computing the energy in the wire at any time, the apparent energy difference will disappear. In every case the theory constructed to diminish the energy gap has been macroscopic, depending on the circuit equations, and ignoring electronic processes in the metal wire sample. Such treatments have not solved the problem. Attempts to show that the energy disparity is due to non-ohmic effects^(r) have been shown by subsequent experiments to have no validity.^(r) The non-ohmic current observation was probably the result of circuit inductance not measured in the relevant experiment.^(r)

It is proposed below that prior to melting, at least part of the "missing" energy can be attributed to charge separation by the Hall effect. The large current densities in exploding wire experiments result in magnetic fields large enough to cause substantial charge separation. It will be shown below that the energy required to maintain the separation can account for all of the energy placed in the wire. The theory applied here also provides a means for indicating in some cases whether the particular wire with a given set of current and voltage waveforms melts from the exterior or interior.

II. Theory

The wire to be exploded is in series with an inductor and a capacitor which is charged by an external power supply. The capacitor is rapidly discharged through the series R-L-wire circuit. The wire has a radius small enough that resultant current densities can exceed 10^5 or 10^6 amps/cm². Such large current densities give rise to appreciable ohmic heating and an orbital magnetic field. The magnetic field acts on the wire to deflect negative charge carriers away from the center until equilibrium is established between the force exerted on the charges by the magnetic field and the radial electric field established by the space charge of electrons. Since the current changes rapidly with time, so does the magnetic field and the resulting radial electric field, or Hall field.

We will consider the period of time from the onset of current through the wire to the time of melting. This constitutes 1/5 to 1/4 of a cycle for the discharge circuit with a negligible resistance rod in place of the wire. During this time we will assume that Fermi-Dirac statistics remain valid, radiation energy losses and thermionic emission are negligible, the metal wire remains ohmic (the current is always proportional to voltage to the first power). The Boltzmann equation will be written in cylindrical coordinates for the wire in the presence of longitudinal and radial electric fields E_z and E_r respectively, and orbital magnetic field due to the current B_ϕ . The distribution function in the presence of these fields is assumed to be linear in the field-free distribution function. Finally the longitudinal and radial current densities are written and the Hall field is derived. In cylindrical coordinates the electron distribution function is

$$f(r, \phi, z, v_r, v_\phi, v_z) \quad (1)$$

The Boltzmann equation for the distribution is

$$\left(\frac{\partial f}{\partial t} \right)_{\text{coll}} = -v_r \frac{\partial f}{\partial r} - v_z \frac{\partial f}{\partial z} - a_r \frac{\partial f}{\partial v_r} - a_z \frac{\partial f}{\partial v_z} \quad (2)$$

The force exerted by the electrical and magnetic fields (\underline{E} and \underline{B}) on electrons is

$$m \underline{a} = -e \underline{E} - e \underline{v} \times \underline{B} \quad (3)$$

which reduces to

$$\begin{aligned} a_r &= -\frac{e}{m} (E_r + v_z B_\phi) \\ a_\phi &= 0 \\ a_z &= -\frac{e}{m} (E_z - v_r B_\phi) \end{aligned} \quad (4)$$

Following Lorentz^(r) and Gans^(r) the collision term is simplified by assuming that electrons make only elastic collisions, scattering is isotropic, and the distribution function when fields are present, f , is related to the distribution function when no fields are present, f^0 , by the relation

$$f = f^0 + v_z \chi_1 + v_r \chi_2 \quad (5)$$

where χ_1 and χ_2 are small undetermined functions which depend only on the scalar quantity $v = \sqrt{v_z^2 + v_r^2}$. Deviations from equilibrium are assumed to be small:

$$v_z \chi_1, v_r \chi_2 \ll f^0 \quad (6)$$

This last assumption is valid for the model under consideration since the electric field is small during the first quarter cycle. The sample resistance is on the order of $10^{-2} \Omega$ and the maximum current is on the order of 10^4 amps so the voltage drop across a short (1 or 2 cm) sample is on the order of hundreds of volts. Similarly the magnetic field is on the order of 10^{-3} weber/cm².

Following Seitz

$$\left(\frac{df}{dt} \right)_{dr,ft} = \frac{v}{\ell} (v_z \chi_1 + v_r \chi_2) \quad (7)$$

and at equilibrium

$$\left(\frac{df}{dt} \right)_{dr,ft} = \left(\frac{df}{dt} \right)_{coll} \quad (8)$$

Eq 2,4,5,7,8 are combined to give

$$\begin{aligned} -\frac{v}{\ell} (v_z \chi_1 + v_r \chi_2) &= v_r \frac{\partial f^0}{\partial r} + v_z \frac{\partial f^0}{\partial z} - \frac{e}{m} (E_r + v_z B_\phi) \left(\frac{\partial f^0}{\partial v_r} + \chi_2 \right) \\ &\quad - \frac{e}{m} (E_z - v_r B_\phi) \left(\frac{\partial f^0}{\partial v_z} + \chi_1 \right) \end{aligned} \quad (9)$$

The derivatives with respect to v_r , v_z can be replaced by the derivative with respect to electron energy, ϵ , if

$$\epsilon = \frac{1}{2} m v^2 \quad (10)$$

Using the substitution 10 in eq. 9 and equating coefficients of equations relating χ_1 , χ_2 to the distribution function can be found.

$$\chi_1 = -\frac{l}{v} \frac{f_1 - s f_2}{s^2 + 1} \quad \chi_2 = -\frac{l}{v} \frac{f_2 + s f_1}{s^2 + 1} \quad (11)$$

where l is the mean free path,

$$s = \frac{e l}{m v} B_z = \mu B_z \quad (12)$$

μ is the electron mobility and

$$f_1 = \frac{\partial f^0}{\partial z} - e E_z \frac{\partial f^0}{\partial \epsilon} \quad f_2 = \frac{\partial f^0}{\partial r} - e E_r \frac{\partial f^0}{\partial \epsilon} \quad (13)$$

The current in the r and z directions are

$$J_z = -e \int v_z f d\sigma \quad (14)$$

$$J_r = -e \int v_r f d\sigma$$

where in cylindrical coordinates

$$d\sigma = 4\pi v^2 dv \quad (15)$$

The temperature in the z direction is assumed to be uniform while a radial gradient can exist.

$$\frac{\partial f^0}{\partial z} = 0 \quad \frac{\partial f^0}{\partial r} \neq 0 \quad (16)$$

When the Hall field is established

$$J_r = 0 \quad (17)$$

Using eqs. 5, 15, 17 in 14

$$J_z = -4\pi e \int v_z^2 \chi_1 v^2 dv$$

$$0 = -4\pi e \int v_r^2 \chi_2 v^2 dv \quad (18)$$

$$\text{let } v_r^2 = v_z^2 = \frac{1}{3} v^2 \quad (19)$$

Using the eqs. 11 and 13 in 18

$$J_z = -\frac{4\pi e}{3} \int \frac{l v^3 dv}{s^2 + 1} \left(e E_z \frac{\partial f^0}{\partial \epsilon} + s \frac{\partial f^0}{\partial r} - e s E_r \frac{\partial f^0}{\partial \epsilon} \right) \quad (20)$$

$$0 = \int \frac{l v^3 dv}{s^2 + 1} \left(\frac{\partial f^0}{\partial r} - e E_r - e s E_z \frac{\partial f^0}{\partial z} \right)$$

Substitute $\epsilon = 1/2 mv^2$ in 20 and let $c/V = \frac{4\pi}{h^3} (2m)^{3/2}$ (21)

$$f^0 = 2 \left(\frac{m}{h} \right)^3 f(\epsilon) = 2 \left(\frac{m}{h} \right)^3 \left[1 + \exp \left(\frac{\epsilon - \epsilon'}{kT} \right) \right]^{-1} \quad (22), (23)$$

$f(\epsilon)$ is the Femi-Dirac distribution function. In the range of temperatures of interest, i.e., below the boiling point, the Fermi energy ϵ' is

$$\epsilon' \cong \epsilon^0 = \frac{h^2}{2m} \left(\frac{3n_0}{8\pi} \right)^{2/3} \quad (24)$$

Where n_0 is the electron concentration and ϵ_0 is the Fermi energy at absolute zero. Let

$$\begin{aligned} L_1 &= c/V \int \frac{\epsilon l}{s^2+1} \frac{\partial f(\epsilon)}{\partial \epsilon} d\epsilon \\ L_2 &= c/V \int \frac{\epsilon l s}{s^2+1} \frac{\partial f(\epsilon)}{\partial \epsilon} d\epsilon \\ L_3 &= c/V \int \frac{\epsilon l s}{s^2+1} \frac{\partial f(\epsilon)}{\partial r} d\epsilon \\ L_4 &= c/V \int \frac{\epsilon l}{s^2+1} \frac{\partial f(\epsilon)}{\partial r} d\epsilon \end{aligned} \quad (25)$$

Then eqs. 20 become

$$\begin{aligned} J_z &= \frac{e}{3} \sqrt{\frac{2}{m}} (-e E_z L_1 + e E_r L_2 - L_3) \\ 0 &= -e E_r L_1 - e E_z L_2 + L_4 \end{aligned} \quad (26)$$

E_z can be eliminated and equations 26 can be solved for the Hall electric field

$$E_r = \frac{3}{e^2} \sqrt{\frac{m}{2}} \frac{s}{1+s^2} \frac{J_z}{L_1} + \frac{L_4}{e L_1} \quad (27)$$

The first term on the right is the isothermal Hall field.

$$E_r = R_H J_z B_\phi + \frac{L_4}{e L_1} \quad (28)$$

where R_H is the Hall constant. The second term is of special interest since it will show the effect of a temperature gradient.

The mean free path is independent of energy since the medium is ohmic for the magnitude of electric fields observed. Also the magnetic fields are small enough so that $s \ll 1$. Under these conditions the second term in eq (28) reduces to

$$\frac{L_4}{e L_1} = \frac{\int \epsilon \frac{\partial f(\epsilon)}{\partial r} d\epsilon}{e \int \epsilon \frac{\partial f(\epsilon)}{\partial \epsilon} d\epsilon} \quad (29)$$

Now

$$\frac{\partial f(\epsilon)}{\partial r} = \frac{\partial f(\epsilon)}{\partial T} \frac{\partial T}{\partial r} = \kappa T \frac{\partial f(\epsilon)}{\partial \epsilon} \frac{\partial}{\partial T} \left[\frac{\epsilon - \epsilon'}{\kappa T} \right] \frac{dT}{dr} \quad (30)$$

Combining eqs. 29 and 30

$$\frac{L_H}{e L_1} = \frac{- \int_0^\infty \left[\frac{\epsilon}{T} + T \frac{\partial}{\partial T} \left(\frac{\epsilon'}{T} \right) \right] \epsilon \frac{dT}{dr} \frac{\partial f}{\partial \epsilon} d\epsilon}{e \int_0^\infty \epsilon \frac{\partial f(\epsilon)}{\partial \epsilon} d\epsilon} \quad (31)$$

The integrals can be evaluated by using the property of the Fermi-Dirac distribution function

$$\int_0^\infty \epsilon \frac{\partial f}{\partial \epsilon} d\epsilon = -1 \quad (32)$$

$$\frac{L_H}{e L_1} = -\frac{1}{e} \frac{dT}{dr} \left[\frac{\epsilon'}{T} + T \frac{\partial}{\partial T} \left(\frac{\epsilon'}{T} \right) \right] = -\frac{1}{e} \frac{\partial \epsilon'}{\partial T} \frac{dT}{dr} \quad (33)$$

The factor $\frac{\partial \epsilon'}{\partial T}$ is just the electronic specific heat γT

$$\frac{\partial \epsilon'}{\partial T} = \gamma T \quad \gamma = \frac{\pi^2 k^2}{2 \epsilon_0} \quad (34)$$

The Hall field can now be rewritten in terms of experimentally meaningful quantities:

$$E_r = R_H J_z B_\phi + \frac{\gamma}{e} T \frac{dT}{dr} \quad (35)$$

The temperature gradient can be expected to be quite small since for copper, $\gamma = 7.5 \times 10^{-8} \text{ J/mole-deg}^2$ and the ratio γ/e is about $5 \times 10^{-11} \text{ volt/mole deg}^2$. E_r is on the order of volts/cm which shows that $\frac{dT}{dr}$ must be exceedingly small. So what is proposed is

that from the plot of current versus time the isothermal Hall field, E_{r1} , will be calculated and the instantaneous energy will be computed

$$U_1 = n_0 e \int_0^a E_{r1} dr \quad (36)$$

where n_0 is the electron concentration and a is the wire radius. The instantaneous energy in the wire, U_0 , will be calculated.

$$U_0 = \int_0^t I V dt - \frac{1}{2} L I^2 \quad (37)$$

The difference between U_0 and U_1 , consists primarily of the energy in the wire responsible for joule heating. Under some circumstances the time of melting can be observed as a notch on the current waveform. At this time the energy required for melting can be compared with the energy difference $U_0 - U_1 = U_2$. U_2 can be zero or on the order of experimental error. If so, the energy has all been taken into account. If U_2 is positive, melting occurs from the exterior while if U_2 is negative, melting occurs from the interior.

Results

Sample calculation for #22 Cu wire with

$$I = 1.5 \times 10^4 \text{ amps}$$

$$\text{radius } A = 3.56 \times 10^{-2}$$

$$l = 5 \text{ cm}$$

$$\text{area } \pi A^2 = 4 \times 10^{-3} \text{ cm}^2$$

$$J = I/A = 3.75 \times 10^6 \text{ amps/cm}^2$$

$$N = 1.3 \times 10^{23} \text{ electrons/cm}^3$$

$$R = 6.6 \times 10^{-5} \text{ cm}^3/\text{amp-sec}$$

$$B = \frac{\mu I}{2\pi A^2} r = \frac{\mu}{2} J r$$

$$E_{r1} = R_H B_\phi J = \frac{\mu R_H}{2} J^2 r$$

$$V_1 = \int_0^A E_r(r) dr = \frac{\mu R_H}{4} J^2 A^2$$

$$V_1 = .374 \text{ volt} \times 10^{-2}$$

$$n = NAl = 2.6 \times 10^{21} \text{ electrons}$$

$$U_1 = nV_1 = 9.7 \times 10^{20} \text{ ev} = 1.5 \text{ joules}$$

Energy required to melt sample

$$U_m = Ms(T_m - T_o) + Mlf$$

$$= (.178 \text{ gm}) \left[.418 \frac{\text{joule}}{\text{gm}^\circ\text{K}} (1063^\circ\text{K}) + 205 \text{ joules/gm} \right]$$

$$= (.178) [650] = \underline{\underline{11.6 \text{ joules}}}$$

Therefore the wire will not melt until at least

$$U_1 + U_m = 1.5 + 11.6 = 13.1 \text{ joules}$$

have been placed in the sample. As can be seen, the total energy put into the wire up to melting is about 13% higher than would be expected in thermodynamic arguments.

REFERENCES USED IN THIS PROPOSAL (NOT IN ORDER OF APPEARANCE)

- (1) F. H. Webb et al, Phys Fluids 3, 318 (1960)
- (2) L. N. Borodovskaja and S. Lebedev, Sov Phys JETP, 1, 71 (1955)
- (3) C. P. Nash and C. W. Olsen, Phys Fluids I, 209 (1964)
- (4) A. Hobson and C. K. Manka, J. Appl. Phys. 37, 1897 (1966)
- (5) B. Stenerhag et al, Z. Physik 198, 172 (1967)
- (6) F. D. Bennett, Phys Fluids 9, 471 (1966)
- (7) F. D. Bennett, Phys Fluids 7, 147 (1964)
- (8) T. J. Tucker, J. Appl. Phys. 30, 1841 (1959)
- (9) F. D. Bennett and J. W. Marvin, Rev. Sci, Instr. 33, 1218 (1962)
- (10) M. G. Haines, Proc. Phys. Soc. 74, 576 (1959)
- (11) W. Ehrenberg, Electronic Conduction in Semiconductors and Metals, Clarendon Press (1958)
- (12) F. Seitz, The Modern Theory of Solids, McGraw-Hill (1940)
- (13) C. Kittel, Introduction to Solid State Physics, John Wiley and Sons, Inc. (1963)

X-RAY MEASUREMENTS ON VAPOR DENSITY IN EWP

Introduction

Historically, the first published results for x-ray studies of exploding wires are found in 1959. Schaafs (Ref. 12) describes a flash x-ray unit and presents some drawings of typical radiographs. Muller (Ref. 13) presents several excellent radiographs, taken by G. Thomer, to substantiate his optical data. He presents both sides and axial views of an exploding wire. In the axial view, the formation of an expanding "hollow" cylinder of vapor is clearly shown. In 1965, Chace (Ref. 14) describes some preliminary survey work of exploding wires and voils, and Kulgavchuk and Novoskol'tseva (Ref. 15) present pulsed x-ray data on wires exploded in air and in polyethylene tubing. In the last two cases, radiographs of sideviews of the exploding wires were presented. In 1968, Fansler and Shear (Ref. 16) published a definitive work featuring the onset and development of striations in exploding wires as seen by pulsed x-rays, correlating the events with respect to voltage and current waveforms. In consultation with W. G. Chace, it was decided that we would try to devise a method for measuring the instantaneous density of an expanding cylinder of vapor by utilizing flash x-rays and the axial method pioneered by Thomer.

The mechanism for the vaporization of an exploding wire is under active investigation by many people (See Ref. 17 for an excellent summary and bibliography). Streak photography (Ref. 18) and x-ray radiographs (Ref. 16) are currently supplanting Kerr-cell photography and spectroscopic techniques. X-ray investigators have been primarily concerned with the onset and development of density striations, which are oriented transverse to current flow in the expanding cylinder produced by an exploding wire. The present work deals with pulsed x-ray beam parallel to the wire axis, thus obtaining a representation of the radial density. If several such radiograms are taken at sequential time intervals, then a plot of vapor density can be shown with respect to radius and time.

The axial radiogram was chosen because of the cumulative effect on x-ray absorption by about 5 cm of wire vapor. Side views barely show the sheath surrounding the core of an exploding wire and the hope was that the longer absorption path in an axial view would bring out detail not possible otherwise. Also, the geometry would allow simple measurements of the radial variation in vapor density.

Since the flash x-ray unit is a single-shot device, only one radiogram can be obtained per wire explosion. Thus a different wire must be exploded for each new time delay and care must be taken to ensure the repeatability of the explosions. Each radiograph produces a complete density versus radius graph for a given delay time.

Experimental Goals

The primary goal of the flash x-ray utilization program was to ascertain if meaningful and precise measurements could be made in the exploding wire experiment. It was soon established that instantaneous density measurements were possible.

The results, to date, are the following (1) a simple correspondence has been shown to exist between the sheath (as seen in a flash radiograph) and the optical size of the expanding vapor, (2) the density of copper and tin vapors, expanding at rates of about 10^5 cm/sec, have been plotted as a function of radius and time, (3) initial evaluations have been made of the net radial mass flow, as a function of radius and time, by comparison of density curves separated by short time intervals.

Experimental Procedure

Each explosion is recorded several ways: (1) visually, with a Faraday Effect camera, (2) with x-rays, in the form of a flash radiograph, (3) electrically, with the total-current waveform, (4) the display of timing pulses from the visual camera and x-ray unit on the current waveform oscillograph. Each radiograph is calibrated with an eight step wedge made of the wire material under investigation

(tin and copper). This enables one to normalize each radiograph with respect to the background level on the developed film. Thus each radiograph will have its particular film density vs vapor density calibration.

The experimental setup is diagrammed in fig. 1. The x-ray unit used has a dual-tube configuration. The two tubes fire simultaneously. Tube A produces the axial radiograph. It is placed as far away from the wire as possible so as to secure an approximation to parallel x-rays in the beam. However distance reduces image density so the 80 cm was arrived at as a compromise.

Tube B was used to monitor each explosion to see whether a uniform cylinder was produced. At lower voltages on the capacitor bank exploding the wires, some wires do not go off as uniform cylinders, thus marring density measurements. These events can be easily distinguished by radiograph B and discarded. The tubes were fired by a capacitor bank charged to 100 kV. The spot diameter in each tube was 1.8 mm, and the film used was Kodak Royal Blue enhanced by a Radelin fine grain intensifier.

In fig. 2, the diagram shows the data secured on the film. First, the radiograph of the vapor cylinder, second, the image of the calibrated wedge (placed close to the vapor image), and third, and image of two rods spaced a known distance apart, so that distances can be determined on the radiograph. In order to measure the change in enlargement ratio between the two ends of the cylinder, one set of rods is placed even with the bottom of the cylinder, and another set even with the top of the cylinder. Measurements show that the enlargement factor changes by about 5%.

The components of a radiograph are shown in fig. 3. In A, are shown the four steps of a typical wedge. Instead of an eight step wedge, we employ two four step wedges, with the vise the same in each, but the first step of one wedge one-half that of the second. Thus we effectively obtain eight steps, closely spaced. B shows the axial pattern obtained by tube A of fig. 1. The very dense object is the wire holder. The cylinder can be seen to be circular in cross-section, obscuration due to the wire holders occuring late in the explosion.

Figure 3 was taken 25 microseconds after the start of the current. The radiograph presented by the monitor tube, the side view, is shown in C. The upper and lower holders can be seen, as well as the vapor cloud between the holders. The sheath, or outer cylinder can be made out, and the end effect can also be seen. This would be a radiograph that would be discarded because the end effect produces an uneven density in the core of the cloud, masking the true density of the 5 cm cylinder under observation. Figure 4 shows the wire configuration before explosion. The 45 degree bends are usually out in such a way that the vapor does not affect the density of the vertical cylinder appreciably.

Once a good radiograph is selected, it is scanned by the microphotometer so that the scan moves along a diameter. The results for a typical scan are shown in figure 5. Here, the dashed line indicates the path taken by the microphotometer through the diameter of an axial radiograph. Above it, is the scan of this path as found by the microphotometer. After the scan, the wedges are scanned, to calibrate the microphotometer scale in true density. A typical microphotometer and wedge tracing are shown in figure 6.

To convert from microphotometer tracing to a density-radius curve, the mathematical steps shown in figure 7 are used. Curve A is the microphotometer trace, curve B is the calibration curve obtained by drawing a smooth curve through the eight wedge step points, and curve C is the density-radius curve obtained by transferring curve A off of curve B (as shown by several dashed lines). This is done by a computer program which also smooths the data to produce curve C. Several tests with various x-ray voltages and development lines have shown that curve B has an exponential form in agreement with the discussion on pages 100 to 104 of Ref. 9. The input to the computer program is a set of points, measured from the microphotometer curve, the wedge calibration points, and the total mass of the wire. The output curve C is then integrated by the computer to see if the correct total mass is obtained. For a

cylindrical geometry

$$M = 2\pi \int_0^R r m(r) dr$$

where M = total mass (known)

R = radius of expanding cylinder

m(r) = density in gm/cm²

In this self-consistent check, any integrations differing from the total mass by more than 10% are discarded. Since the wedge calibration curve is of the form

$$y = A(1 - e^{-Bt})$$

where A and B are obtained for each film, the constant B can be varied to obtain the correct mass upon integration, the corrected calibration curve is then used to produce a corrected density curve. This has been incorporated into the computer program in such a way that the micro-meter data and the total mass of the wire are used to produce the corrected density curve.

A typical density curve is shown in figure 8. The result is for 5 cm long copper wire exploded by a 45 microfarad capacitor bank charged to 10kV. This particular curve is for a time 8.2 microseconds after the current has begun and falls just after the rapid fall in current in the first pulse. The arrow on the I(t) curve shows the location in time for the density curve. The vapor cloud has attained a radius of 8 mm and has a decided dip in the density of the core. The leading edge has not yet produced any noticeable piling up of material as the vapor expands into air at atmospheric pressure.

Description of Results

Because of the opaque vapor produced in the exploding wire, internal events are masked and had to be inferred from optical, shock wave and electrical conductivity studies. With flash x-ray, the structure of striations was made possible, and with axial radiographs, density variations in the expanding cylinder may now throw some light on the condition of the wire before rupture. The set of pictures shown in figure 9 illustrate the masking effect of the expanding cloud and vigorous end effects. These were recorded with a camera utilizing a Faraday Effect shutter. They illustrate the rapid expansion of the wire after the first frame. Figure 10 shows this expansion effect in more detail. The top curve is a current waveform showing the first pulse of current, the sudden drop in current as the wire vaporizes, and the resurge. Below this waveform is a graph of the diameter of a copper wire as a function of time as measured with x-rays both graph and current waveform have the same time axis. There is no appreciable expansion until the current starts to fall. At this point, the wire is vaporizing. The current drops because of the rapidly increasing resistance, and at the same time, the expansion curve shows a rapidly changing diameter. The data for the diameter points was obtained by making measurements on the side view radiographs. During this time, the wire is too high in density to make axial density plots feasible. At the present time, axial density plots cannot be made until the wire has expanded to about four times its original radius for copper, and about 10 times its original diameter for tin.

Tin Wire

Tin wire 0.1 cm in diameter (B & S gauge no. 18) and 5 cm long has been measured with the axial flash x-ray technique. A typical set of axial radiographs and total current waveform are shown in figures 11 and 12. The initial capacitor bank voltage for the tin wire in figure 11 was 7kV and for figure 12, 10kV. In each case, the density profiles show an expanding core and sheath. The sheath forms due to the piling up of inner core material as the cloud expands into air at atmospheric pressure. The core appears to expand at a lower rate and as it grows, the material in it falls in density for two reasons, volume change and a net radial flow of material into the sheath. At all times, however, the core seems to have maximum density at the axis. Figure 13 correlates the results of measurements on the radius of the core and sheath using x-rays and the visual diameter seen by visual high speed photography (fig. 9). As can be seen, the visual diameter and x-ray measurements of the sheath coincide, within experimental error. For the tin wire shown in fig. 13, the x-rays have followed the sheath out to about 35 microseconds and show a noticeable slowing down of the sheath (which is about 4 cm in diam. at this time). The sheath and core expand at different rates, about 6×10^5 cm/sec for the sheath, and about 3×10^5 cm/sec for the core. For an appreciable time, the two cylinders expand linearly with time. The corresponding density versus time curves appear in fig. 14. They are tin wire exploded at 7kV. Only several of the total obtained in this series are shown here, for clarity of presentation. A complete set is shown in Appendix II. A is the original radius. The difference in time between curves B and C is only about 5 microseconds, but the change in density is dramatic. As the tin vapor expands the core density drops, maintaining a peak in density along the axis. The incipient sheath structure can be seen in curve B, is further defined in C, and is clearly formed in curve D at about 1.6 cm radius. This sheath moves out the diffuses slightly in the subsequent curves. There is not much change in the sheath position in curves E and F, as the vapor cloud has approached its maximum expansion. Since the

sheath density is nearly constant from curves C to F, this means that here must be a net flow of mass radially outward to maintain this density as the sheath expands. At the same time, the core density is rapidly decreasing.

Copper Wire

Several diameters of copper wire, 5 cm long, were analyzed at 7kV and 10kV initial voltage on the capacitor bank. Data were acquired for No. 28, 26, and 24 copper wire. In figure 15, the combined results of numerous radiographs enabled us to plot the change in diameter as a function of time for both No. 28 and 24 copper wire, exploded at 7kV. The progress for both the sheath and core can be seen. The data for both wires has been put on the same time scale. Zero on this scale signifies the beginning of current flow. The No. 28 wire, being smaller in mass, vaporizes sooner. However, it is quite interesting to note that the slopes for the sheath expansions are the same, and, unexpectedly, the respective core expansions are also very similar. The sameness of the sheath expansions may be argued on the grounds that the final gas temperatures are the same, and they are both expanding into air at atmospheric pressure.

The similarity of core expansions, thus, seems to imply a near sameness of temperature, and pressure in the vapor cloud. For the No. 28 copper wire, the separation of core, and sheath could not be seen until the diameter had exceeded 4 mm. Figure 16 shows several axial radiographs for No. 26 copper wire exploded at 10 kV. Figure 17 shows results for a very early attempt to obtain axial radiographs. Most of the radiographs contain troublesome end effects (the dense, small core). The recognition of these end effects made future data more reliable. However, the pictures illustrate an important effect seen in copper vapor. Both the No. 26 and 24 copper vapor show a core that is "hollow." Actual density measurements with a microphotometer show that the internal core density does not go to zero. Both wires also show the enhancement of the sheath with time, implying a radial mass flow from the core to the

sheath. A summary of density-radius measurements is shown in figures 18 and 19. Figure 18 shows how the density for No. 26 copper vapor varies with time for a selected set of density curves. A complete set of curves for No. 26 Cu wire is shown in Appendix I. The results for No. 24 Cu wire exploded at 10kV are summed up in figure 19. Here the sudden decrease in core axial density can be seen peaking in density just before 0.6 cm radius. In curve G, the sheath has expanded to 1.4 cm radius.

Gaussian Expansion

An attempt to evaluate the radial mass flow is presented here. If one takes two density-radius curves separated by a small time increment and integrates the mass under each curve up to a radius r , then the difference between the two masses would represent the mass lost or gained in the volume represented by the integration limit in the time increment. Using the experimental data available, several curves of dM/dt , having the units $\text{gm/cm}^2\text{-sec}$ were prepared for tin wire exploded at 10kV (figure 20). Differences were taken for all time-adjacent pairs of curves and the three presented seem to be the "best" of the lot. They are deemed valuable only in showing that with refinement, reasonable results can be expected. There is at least a 10% error due to the fact that the total radius has changed significantly between time intervals. However, one cannot take time intervals too close because a difference is involved, and the data spread can cause havoc for such cases. The three curves selected are a compromise. The total time interval between A and C is 4.14 microseconds. The maximum radial flow occurs at .42 cm for case A and moves out with time. There is a large change in the peak rate of flow from A to B, which then appears to remain constant. It should also be noted that the series of curves for tin in figure 20 are mirrored in the equivalent curves for copper as shown in figure 21. There is the same rapid decrease in the peak flux and a subsequent broadening of the peak. These results should be compared to the results one obtains from a spreading gaussian,

figure 22. The curves show plots of the function

$$\rho(r,t) = \frac{\rho_0}{\sqrt{\pi} a_0 \sqrt{1 + \frac{t^2}{\tau^2}}} e^{-\frac{r^2}{a_0^2(1 + \frac{t^2}{\tau^2})}} \quad (1)$$

which when integrated will produce the mass of an equivalent wire.

$$\text{mass} = \int_0^{\infty} \rho(r,t) dV \quad (2)$$

where $dV = 2\pi L r dr$, the volume increment in cylindrical coordinates, and ρ is the volume density, independent of the z -coordinate.

Such a spreading gaussian is typical of the solution of a diffusion equation with a delta function of density as the initial condition. The resulting diffusion with time produces a spreading gaussian. Equation (1), above, was used to obtain the radial mass flow for a gaussian at three time intervals,

Where τ is an effective time constant having to do with the rapidity of the spreading of the gaussian. The plots shown in figure 23 were obtained by evaluating the following equation numerically,

$$\text{mass flux} = \frac{1}{2\pi RL} \int_0^R \frac{[\rho(r, \tau + \delta\tau) - \rho(r, \tau)]}{\delta\tau} 2\pi r dr \quad (3)$$

where R is the radius at which point the mass flux is to be evaluated, $\delta\tau$ is $\frac{1}{10}\tau$, and $2\pi RL$ is the area through which the mass is flowing. The results (figure 23) are very similar to the experimental results shown in figures 20 and 21, for tin and copper, respectively. The qualitative results show that the density function in both cases quickly assumes a gaussian distribution with perturbations due to the initial conditions. Copper, for example, has a prominently depressed axial density but still produces a gaussian-like mass flow. Figure 23 also implies that the vapor expansion is

an impulsive event whose later form has been predetermined by the original event. There would thus be hope of ascertaining initial conditions by evaluating the vapor expansion more precisely.

Conclusions

- A. The method outlined here for determining the instantaneous density of vapor appears to be quite successful. One can easily separate and follow the sheath and core. A set of density functions can be plotted as a function of radius and time.
- B. A definite relationship has been established between the photodiameter and the x-ray sheath diameter for the expanding vapor. A definite core structure and its subsequent change with time has been obtained.
- C. Mass flow data shows that appreciable energy is not added during the expansion phase for tin. For copper, except for a "hollow" core, mass flow from the core surface resembles gaussian flow.
- D. Copper vapor, with its "hollow" core, implies that an appreciable initial temperature gradient existed in the wire fluid at rupture.
- E. The curves for tin and copper both agree with Bennett's assumption (Ref. 18) that the expansion takes the form of a hollow cylinder, i.e. the sheath, with a radius that is increasing linearly with time. Although his work was at low densities, it seems to carry through into atmospheric pressure.
- F. The two cylinders, i.e. core and sheath; expanding at different constant velocities could give rise to the two shock waves sometimes observed by Bennett.

G. Future work could involve:

- a. refining the mass flow data acquisition so that a more precise picture of the flow of metal vapor within the explosion can be obtained.
- b. exploration of the nature of the temperature gradient implied by the copper wire data. Possibly one could try Fe or Ni wire, which decreases in resistance above the melting point, in order to compare those results with copper, and tin, which shows no such gradient effect.
- c. The use of faster film in order to bring out more detail, or to follow the expansion further in time.

REFERENCES

1. Chern, D. C. and Korneff, T. "Current Distribution for Wire Exploded in Vacuo," Exploding Wires Vol. 4, p. 173, Plenum Press, 1968.
2. Chern, D. C. and Korneff, T. "Current Distribution for Wire Exploded in a Vacuum," AFCRL-68-0328, Scientific Report No. 1, May, 1968.
3. Chern, D. C. "Current Distribution for Wire Exploded in Vacuo" M. A. Thesis, Temple University, 1967.
4. Goronkin, H. "Striations in EWP," AFCRL-68-0671, Scientific Report No. 2, Oct., 1968.
5. Goronkin, H. "Striations in Fast Wire Explosions," J. Appl. Phys. 39, 11, Oct. 1968.
6. Korneff, T. and Chace, W. "A Study of Exploding Wires by X-Rays Directed Parallel to the Wire Axis," Paper presented at APS meeting, Washington, D. C., 1969.
7. Korneff, T. and Chace, W., "A Method of Determining Density-Radius Relations During Wire Explosions" Unpublished. Submitted to Rev. Sci. Instr., March, 1970.
8. Korneff, T., "The Density of Copper and Tin Vapor as a Function of Time in EWP Experiments," Paper presented at APS meeting, Chicago, Ill., Jan, 1970.
9. Physics of Industrial Radiology, Halmshaw, Ed., American Elsevier Pub. Co., 1966.
10. Korneff, T. et al, "Study of High Energy, High Density Discharges and High Temperature Measurements as Applied to Exploding Wires" AFCRL-67-0276, Final Report, May 1967.
11. Haines, M. G., "The Inverse Skin Effect," Proc. Phys. Soc., Vol 75, pt. 5, 576-584 (1959).
12. Schaafs, W., "Beobachtungen an Elektrischen Drahtexplosionen," Z. angew. Physik 11, 63-65 (1959).
13. Miller, W. "Studies of Exploding Wire Phenomenon by Use of Kerr Cell Schlieren Photography," Exploding Wires Vol. 1, Chace and Moore, Eds), Plenum Press, N. Y. (1959).

14. Chace, W. G., "Use of X-Rays in Exploding Wire Studies" Bull. Am. Phys. Soc. 10, 166 (1965).
15. Kul'gavchuk, V. M. and Novoskol'tseva, G. A., "X-Ray Study of Kinetics of Heating and Evaporation of Exploding Wires," Sov. Phys. Tech. Phys. 11, No. 3, 406-412 (1966).
16. Fansler, K. S. and Shear, D. D., "Correlated X-Ray and Optical Streak Photographs of Exploding Wires," Exploding Wires, Chace and Moore (Eds) Vol 4, Plenum Press, N. Y. (1968).
17. Bennett, F. D., "High Temperature Exploding Wires," BRL Report No. 1339 (1966).
18. Bennett, F. D., et al, "Qualitative Interferometry of Expanding Metal Vapor," BRL Report No. 1454 (1969).

LIST OF ILLUSTRATIONS

- Figure 1 Geometry with respect to wire and film cassettes for the dual flash x-ray system.
- Figure 2 The information on the radiograph consists of the axial vapor density, two calibrated step wedges, and brass rods at the top and bottom of the vapor cloud, used to calibrate distance on the radiograph.
- Figure 3 Examples of results obtained with the axial and side radiographs. (A) One of the wedges. (B) The axial view showing the circular cross-section of the vapor cloud and the wire holders. (C) A side view showing the vertical cross-section of vapor that is radiographed. Note the end effects, where the density is greater.
- Figure 4 The wire holders are brought out from the main discharge circuit so that the axial x-ray tube will have a clear view of the wire. The plastic-mounted jig is used to shape and straighten the wire after it is clamped by sliding the unit forward, along the wire holders, exerting pressure on the wire, and then retracting it.
- Figure 5 In the bottom diagram, the path scanned by the microphotometer is shown superimposed on an axial radiograph. The corresponding record of the scan is shown above.
- Figure 6 Typical microphotometer scan for an axial radiograph and a calibrated wedge.
- Figure 7 The diagram illustrating the mathematical procedure used to transfer microphotometer data into a density curve. Both the microphotometer trace and density curve use the radius as abscissa. The density is transformed by means of the curve B which is a smooth curve drawn through the wedge calibration points. The resultant density curve has been smoothed by a computer program.

- Figure 8 A typical density (gm/cm^2) versus radius curve for copper wire. This one was made 8.2 microseconds after the current began in the wire. The arrow on the current waveform indicates the position of the density measurement.
- Figure 9 Optical pictures of exploding wires taken with the Faraday effect camera. They show the end effects, expansion of the vapor cloud, striations, and arcing on the surface of the vapor cylinder.
- Figure 10 The correlation of radial expansion with current waveform. The dots are experimental points as obtained from side radiographs. This indicates that the most rapid expansion, occurs just after the current peak.
- Figure 11 Respective axial and side radiographs for tin wire 1 mm in diam, 5 cm long, exploded at 7 kV with a 45 mfd capacitor bank. All times indicated are with respect to the beginning of current.
- Figure 12 Axial radiographs for tin wire 1 mm in diam, 5 cm long, exploded at kV with a 45 mfd capacitor bank. All times indicated are in microseconds and are with respect to the beginning of current.
- Figure 13 The correlation of optical size to x-ray size for tin wire 1 mm in diam exploded at 7 kV. The optical size correlates with the x-ray sheath. An expanding core is also shown. All experimental points are single measurements.
- Figure 14 The density of tin wire 1 mm in diam exploded at 7 kV is shown as a function of radius and time. Selected density curves are shown for clarity. Delay times are with respect to the start of current.
- Figure 15 The diam versus time curves for 0.4 and 0.5 mm diam copper wire, 5 cm long, exploded at 7 kV. The two curves have been placed on the same scale to show the similarity in slopes.
- Figure 16 Axial radiographs for 0.4 mm diam copper wire 5 cm long exploded at ¹⁰kV with 45 mfd capacitor bank. Delays are with respect to the beginning of current.

Figure 17 Axial radiographs for 0.5 mm diam copper wire exploded at 7 kV. They show the troublesome end effects, which show up as a small dense core which does not expand. This is due primarily to the low initial voltage used.

Figure 18 The density of 0.4 mm diam copper wire, 5 cm long, exploded at 10 kV, represented as a function of radius and time. Selected curves are shown for clarity.

Figure 19 The density of 0.5 mm diam copper wire, 5 cm long, exploded at 10 kV, represented as a function of radius and time. Selected curves are shown for clarity.

Figure 20 The radial mass flux for 1 mm diam tin wire as a function of radius and time. Time in microseconds.

Figure 21 The radial mass (flux for 0.4 mm diam copper wire as a function of radius and time. Time in microseconds.

Figure 22 The spread of a gaussian as a function of time.

Figure 23 The radial mass flow calculated for an expanding gaussian.

EQUIPMENT SETUP

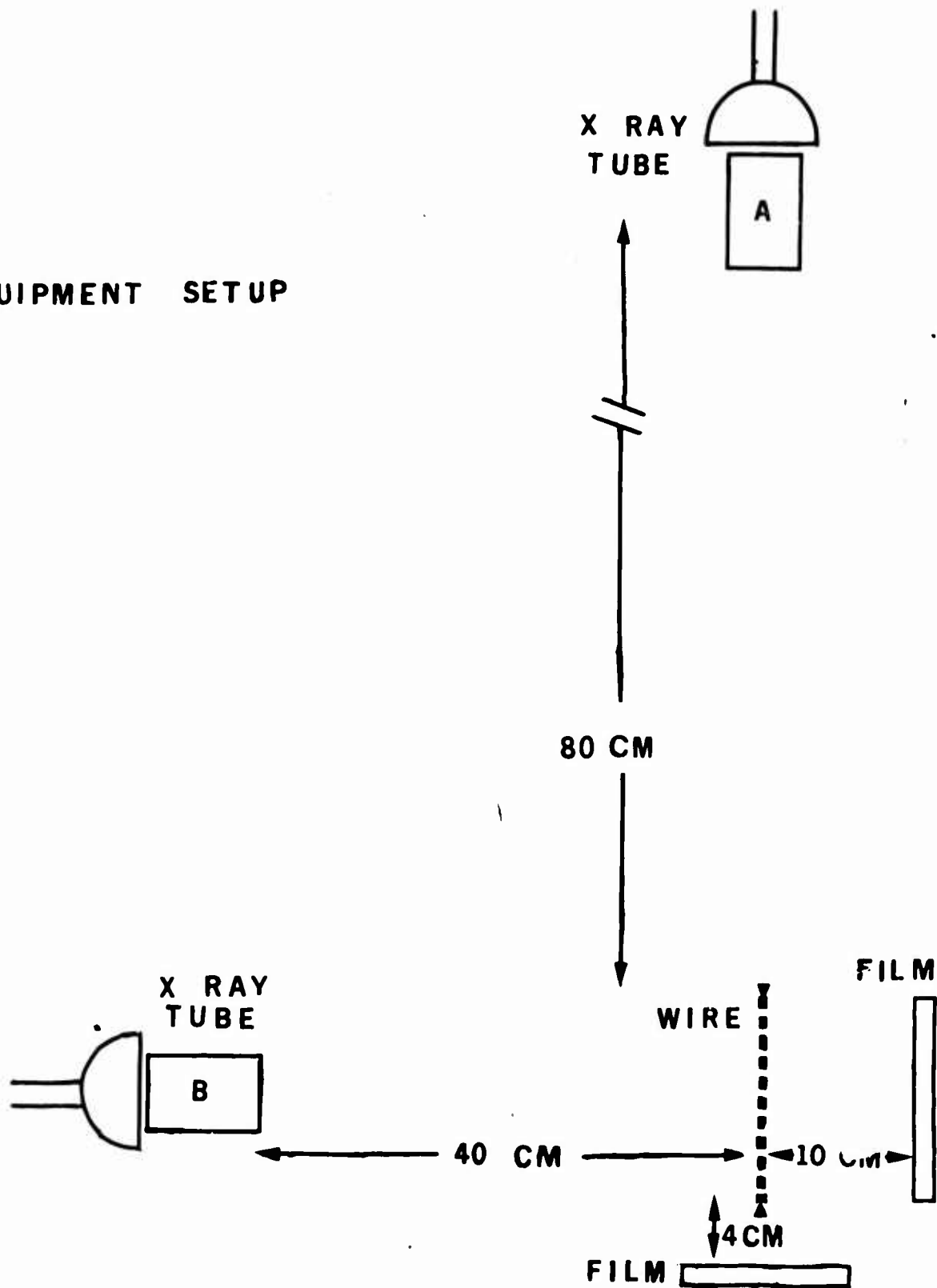


Figure 1 Geometry with respect to wire and film cassettes for the dual flash x-ray system.

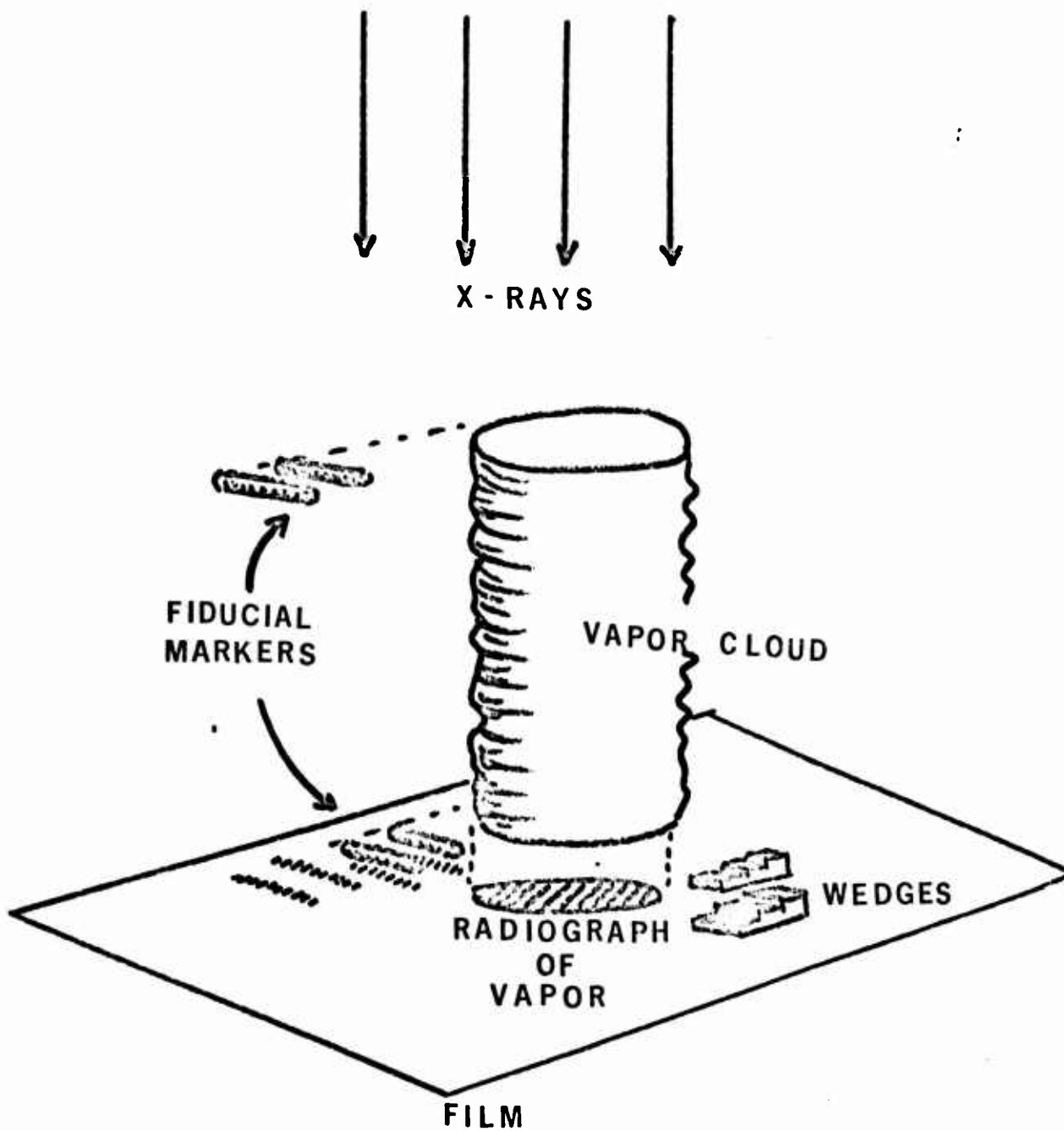


Figure 2 The information on the radiograph consists of the axial vapor density, two calibrated step wedges, and brass rods at the top and bottom of the vapor cloud, used to calibrate distance on the radiograph.

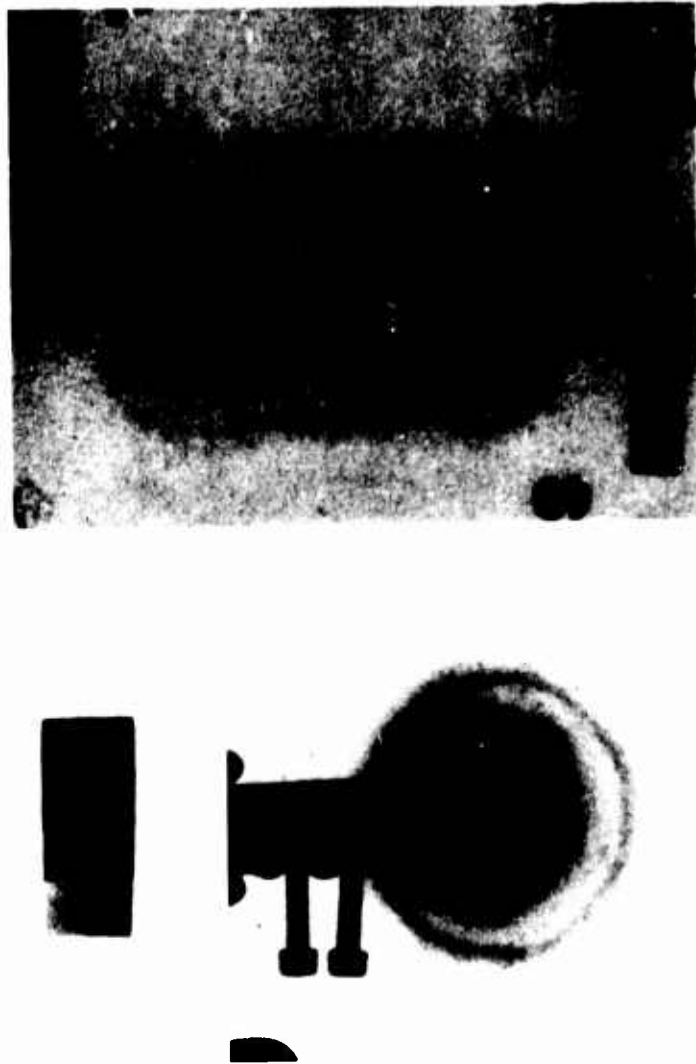


Figure 3. Examples of results obtained with the axial and side radiographs.

- (A) One of the wedges.
- (B) The axial view showing the circular cross-section of the vapor cloud and the wire holders.
- (C) A side view showing the vertical cross-section of vapor that is radiographed. Note the end effects, where the density is greater.



Figure 4. The wire holders are brought out from the main discharge circuit so that the axial x-ray tube will have a clear view of the wire. The plastic-mounted jig is used to shape and straighten the wire after it is clamped by sliding the unit forward, along the wire holders, exerting pressure on the wire, and then retracting it.

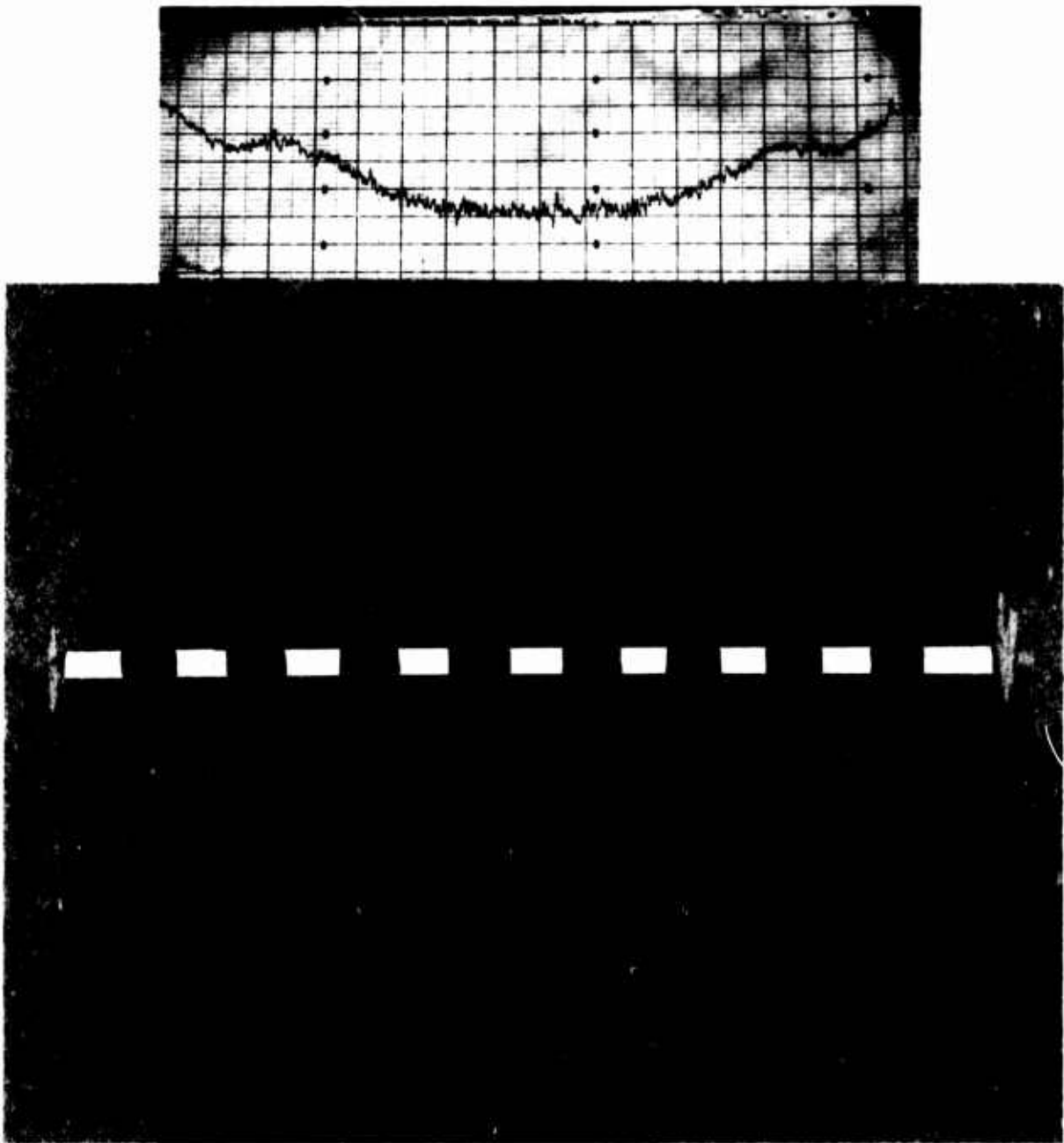


Figure 5. In the bottom diagram, the path scanned by the microphotometer is shown superimposed on an axial radiograph. The corresponding record of the scan is shown above.

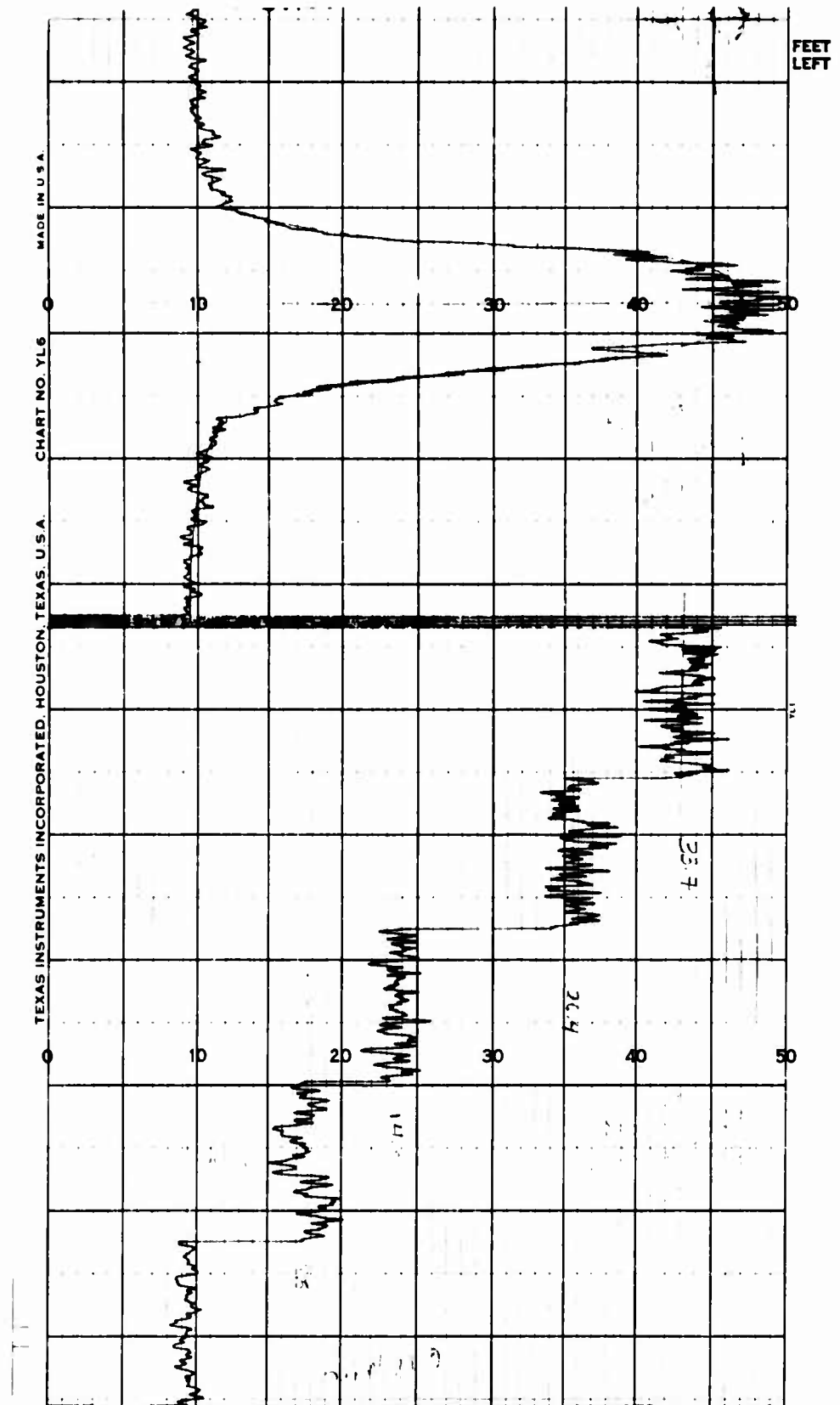


Figure 6. Typical microphotometer scan for an axial radiograph and a calibrated wedge.

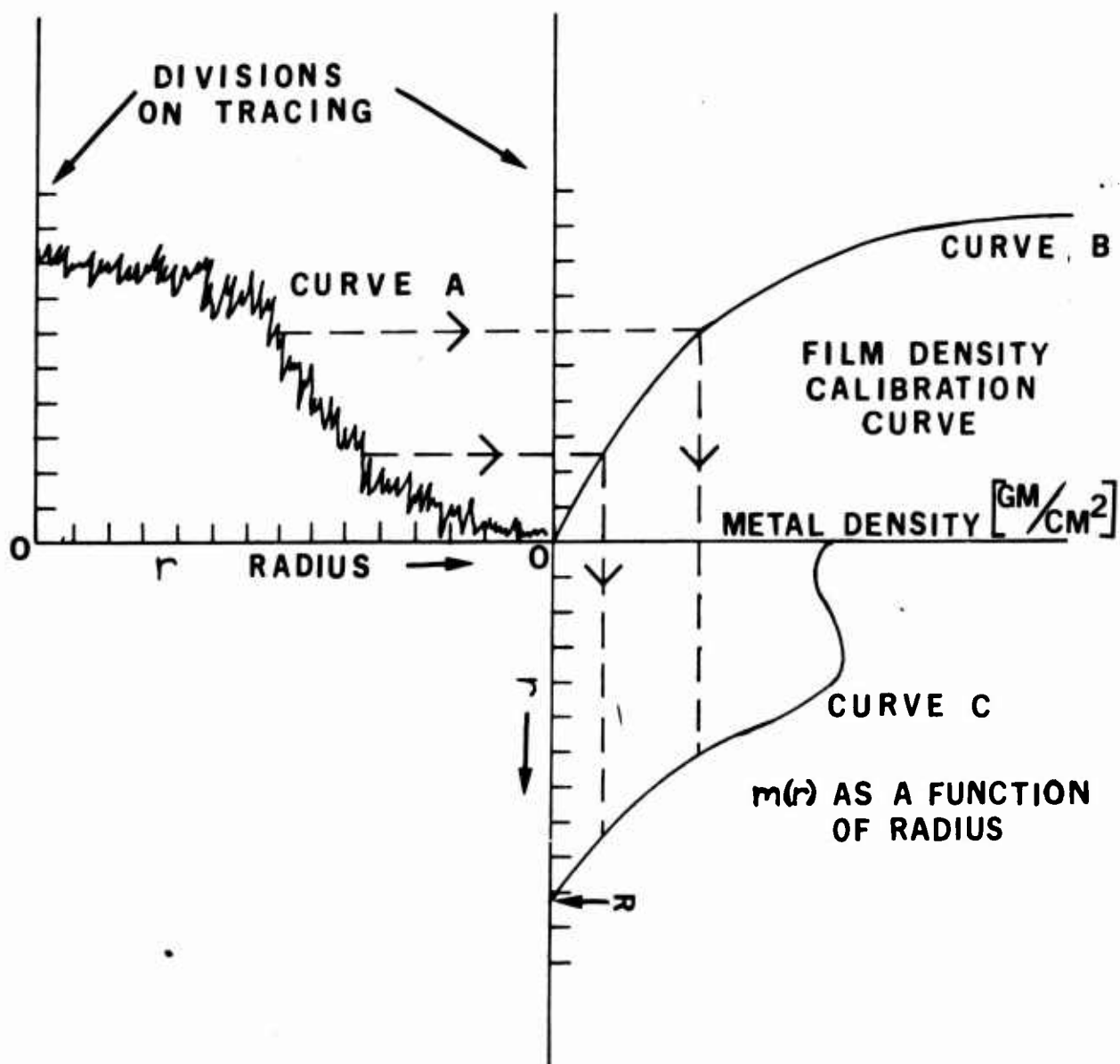


Figure 7 The diagram illustrating the mathematical procedure used to transfer microphotometer data into a density curve. Both the microphotometer trace and density curve use the radius as abscissa. The density is transformed by means of curve B, which is a smooth curve drawn through the wedge calibration points. The resultant density curve has been smoothed by a computer program.

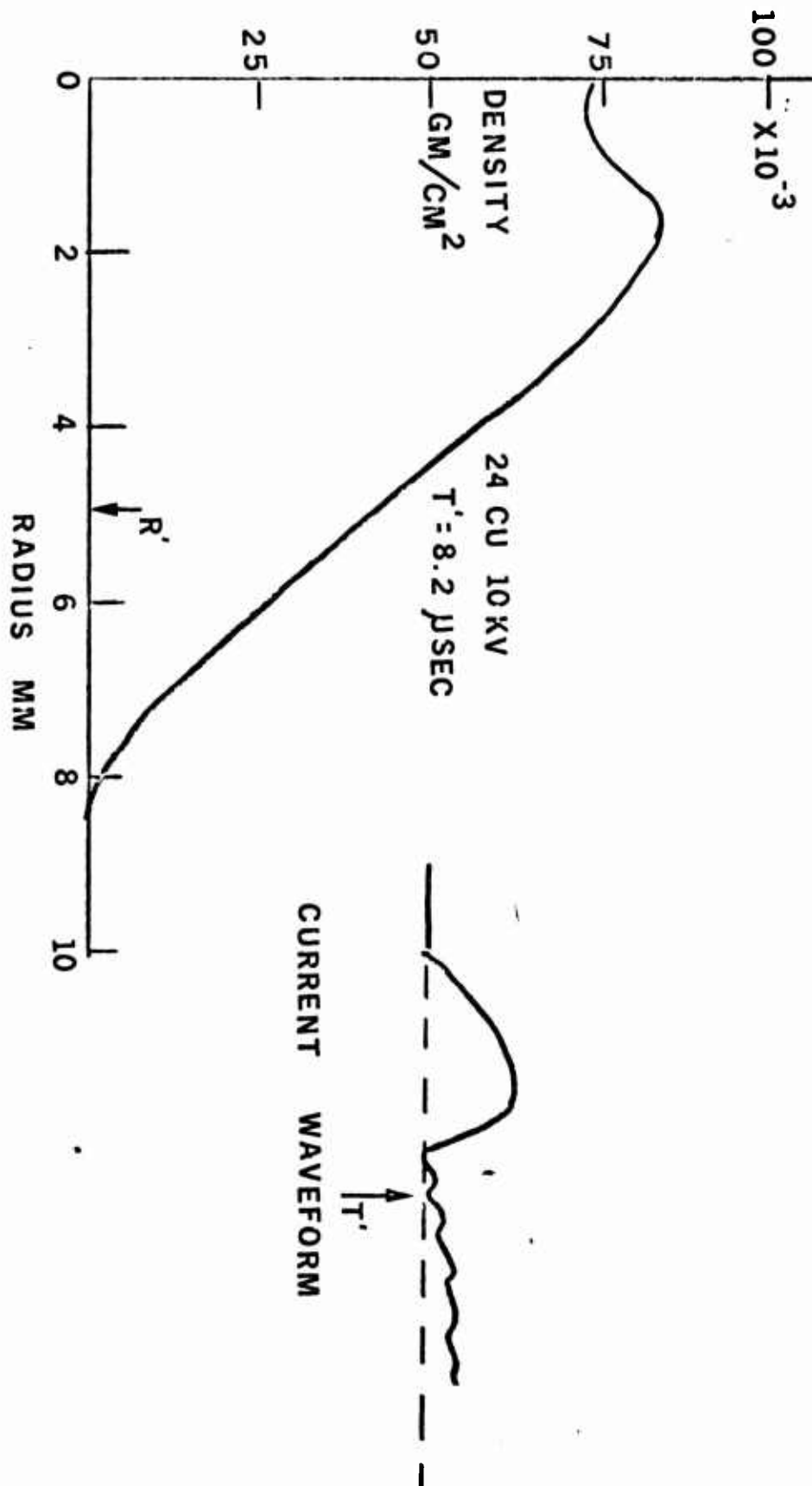
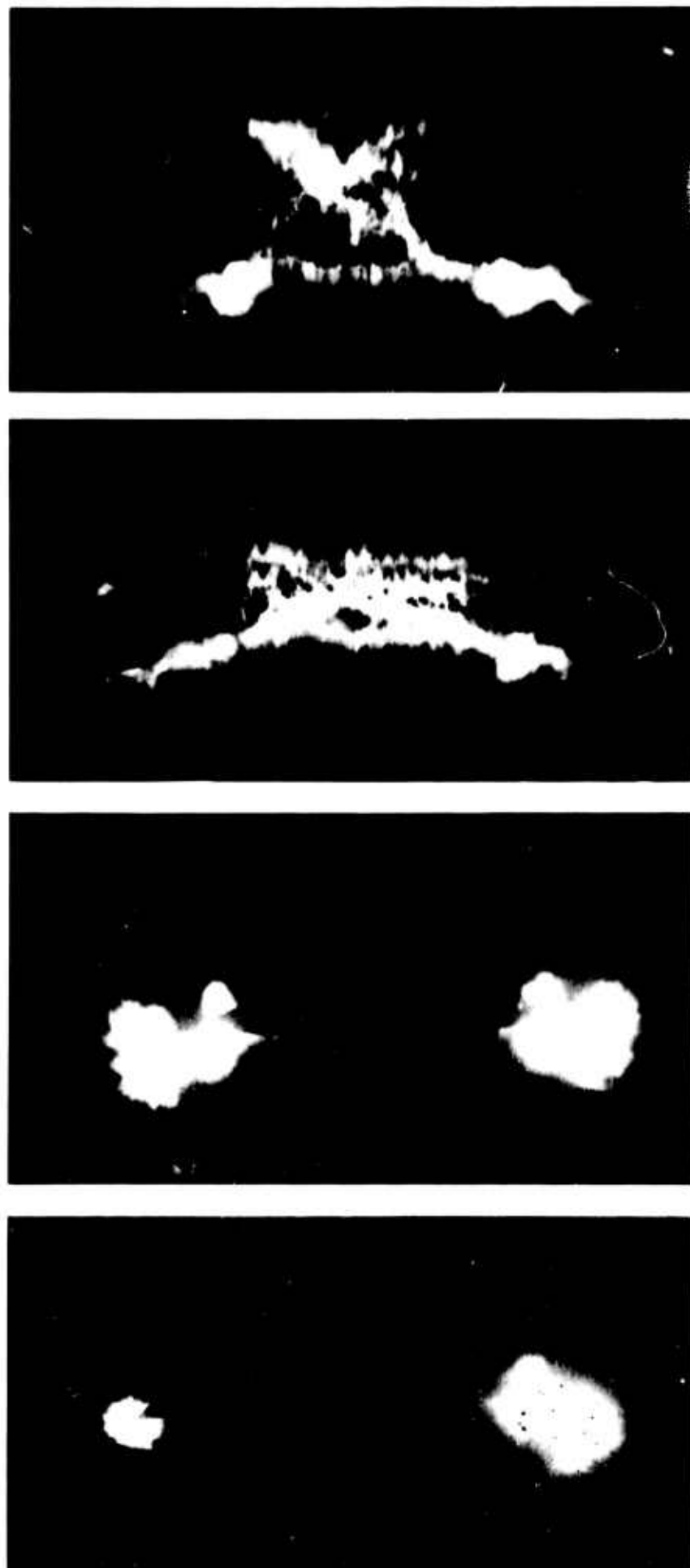


Figure 8 A typical density (gm/cm²) versus radius curve for copper wire. This one was made 8.2 microseconds after the current began to flow in the wire. The arrow on the current waveform indicates the position of the density measurement.

Visual Diam. #18 T_{in} 10kV



41

4.9 μ sec 6.0 9.2 11.2

Figure 9. Optical pictures of exploding wires taken with the Faraday effect camera. They show the end effects, expansion of the vapor cloud, striations, and arcing on the surface of the vapor cylinder.

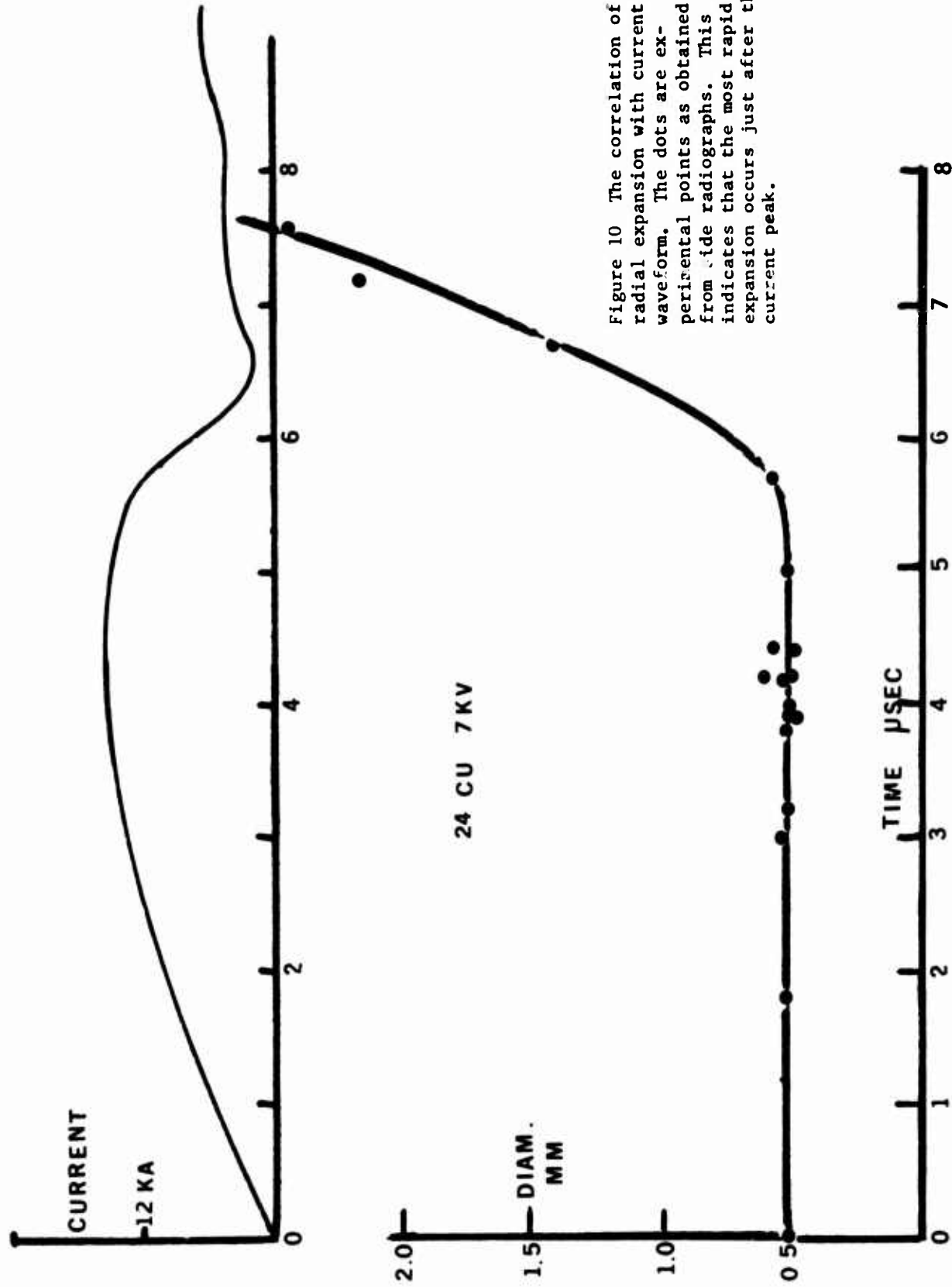


Figure 10 The correlation of radial expansion with current waveform. The dots are experimental points as obtained from side radiographs. This indicates that the most rapid expansion occurs just after the current peak.

Figure 10. The correlation of radial expansion with current waveform. The dots are experimental points as obtained from side radiographs. This indicates that the most rapid expansion occurs just after the current peak.

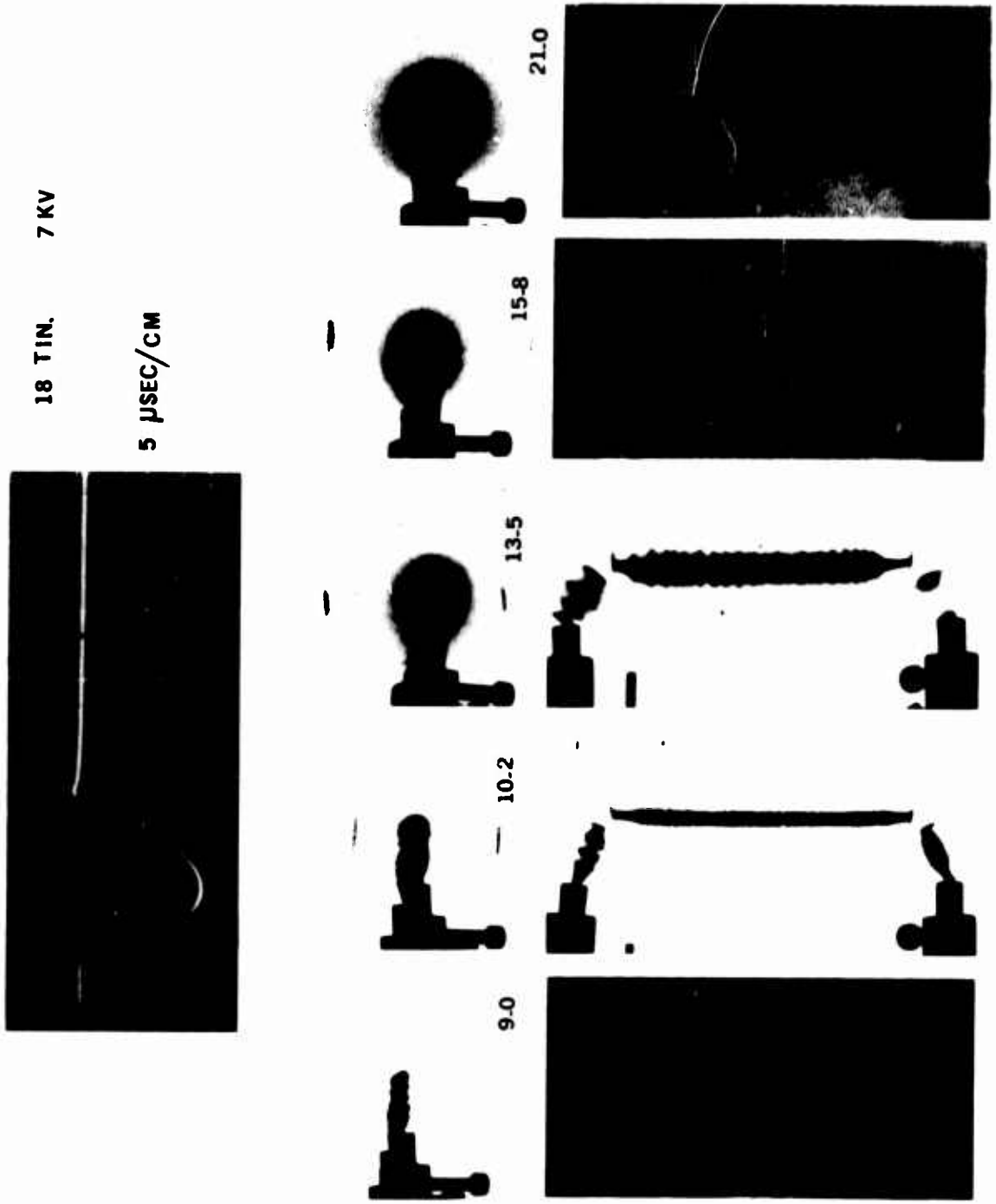


Figure 11. Respective axial and side radiographs for tin wire 1 mm in diam, 5 cm long, exploded at 7 kV with a 45 mfd capacitor bank. All times indicated are with respect to the beginning of current.

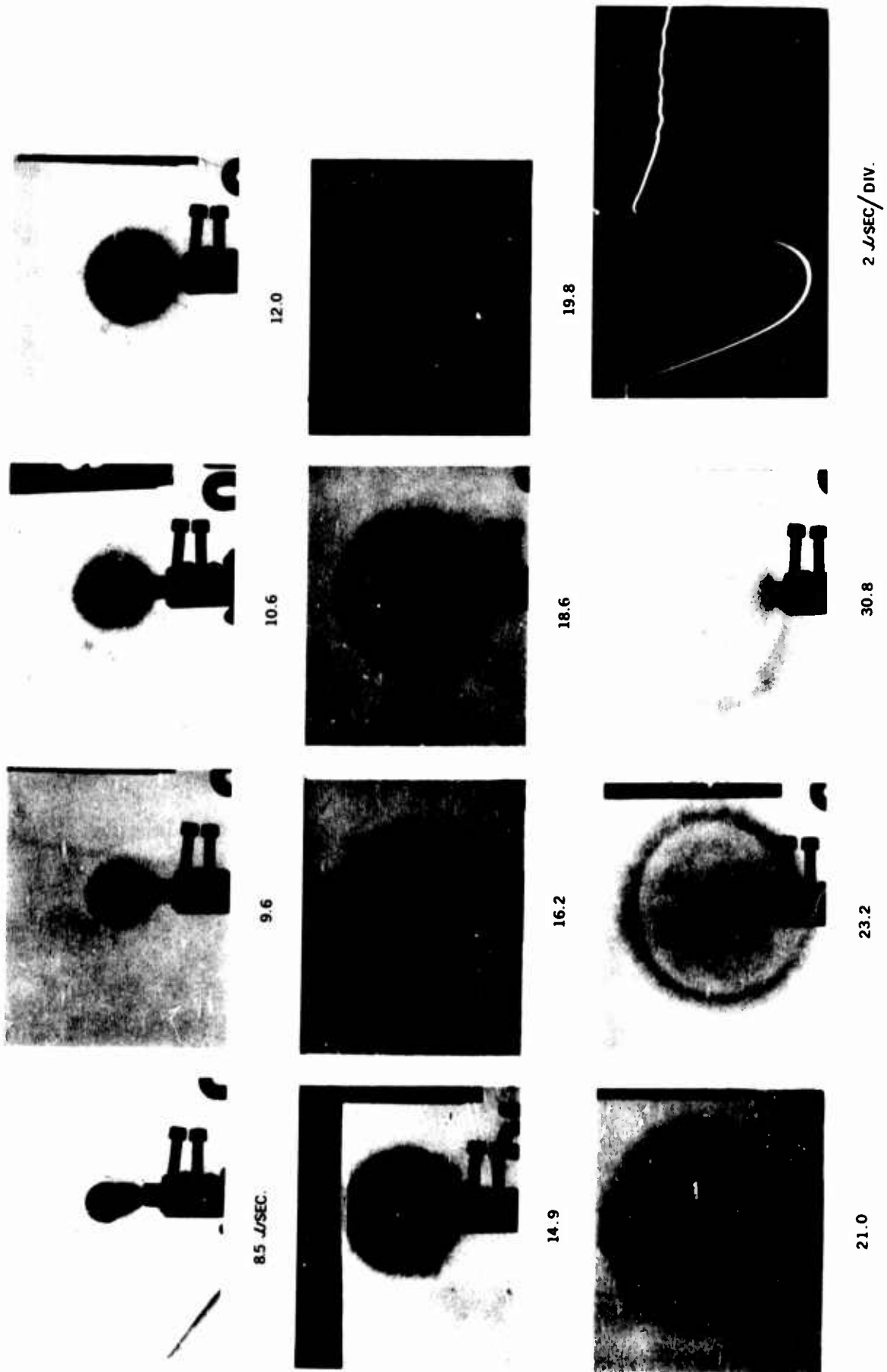
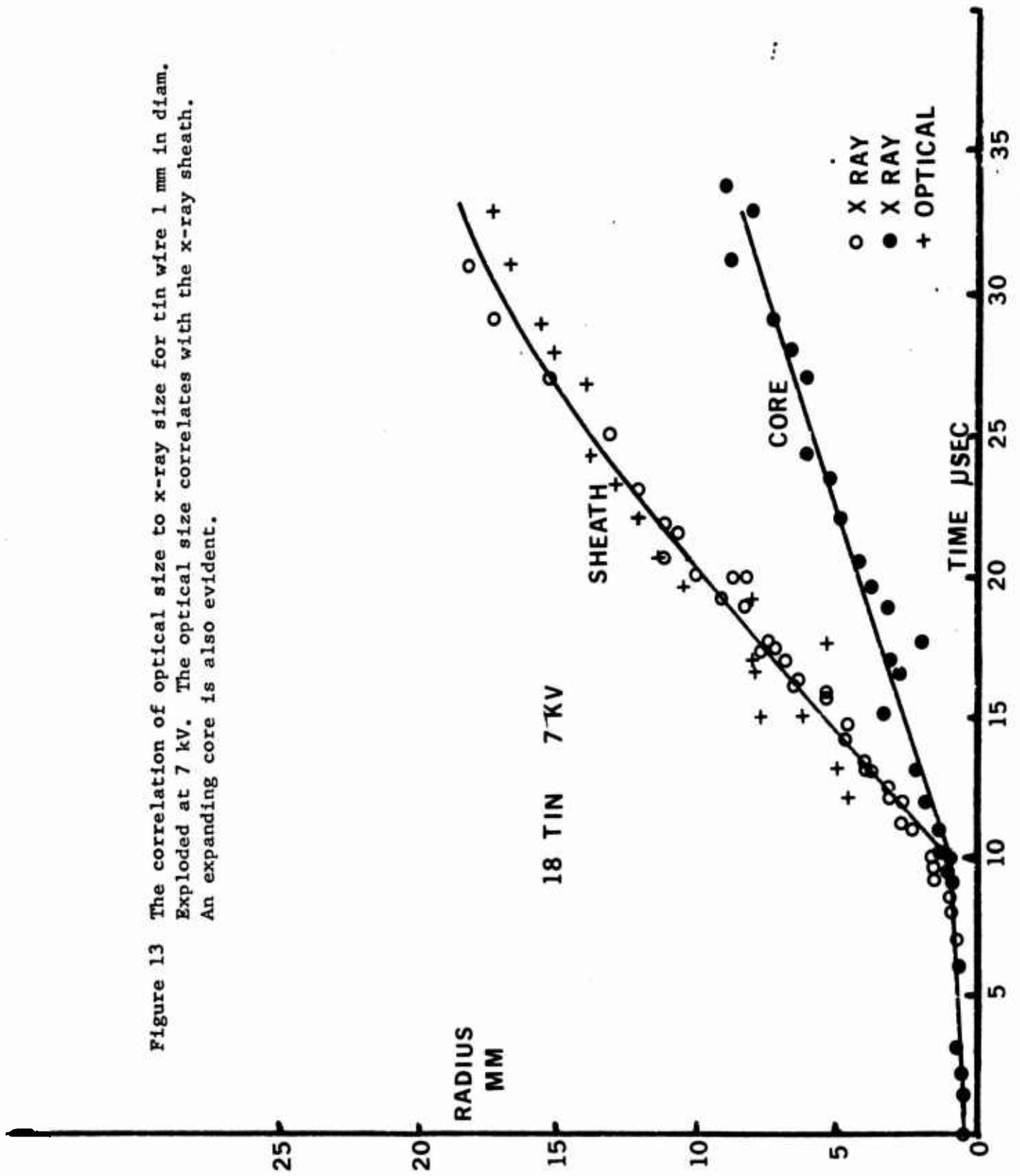
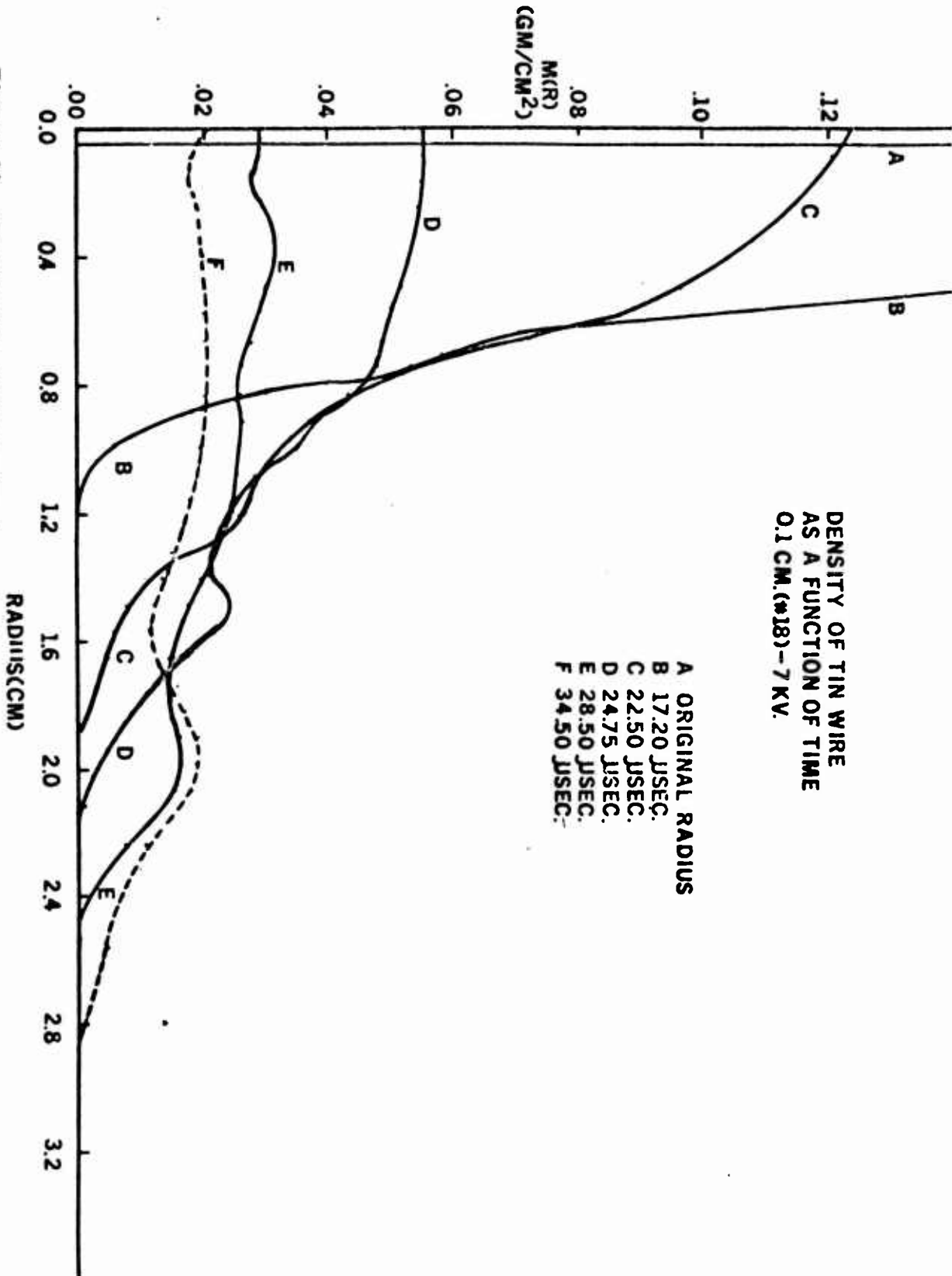


Figure 12. Axial radiographs for tin wire 1 mm in diam, 5 cm long, exploded at 10 kV with a 45 mfd capacitor bank. All times indicated are in microseconds and are with respect to the beginning of current.

Figure 13 The correlation of optical size to x-ray size for tin wire 1 mm in diam.
Exploded at 7 kv. The optical size correlates with the x-ray sheath.
An expanding core is also evident.





DENSITY OF TIN WIRE
AS A FUNCTION OF TIME
0.1 CM. (#18) - 7 KV.

A ORIGINAL RADIUS
B 17.20 μSEC.
C 22.50 μSEC.
D 24.75 μSEC.
E 28.50 μSEC.
F 34.50 μSEC.

Figure 14 The density of tin wire 1 mm in diam. exploded at 7 kV is shown as a function of radius and time. Selected density curves are shown for clarity. Delay times are with respect to the start of current.

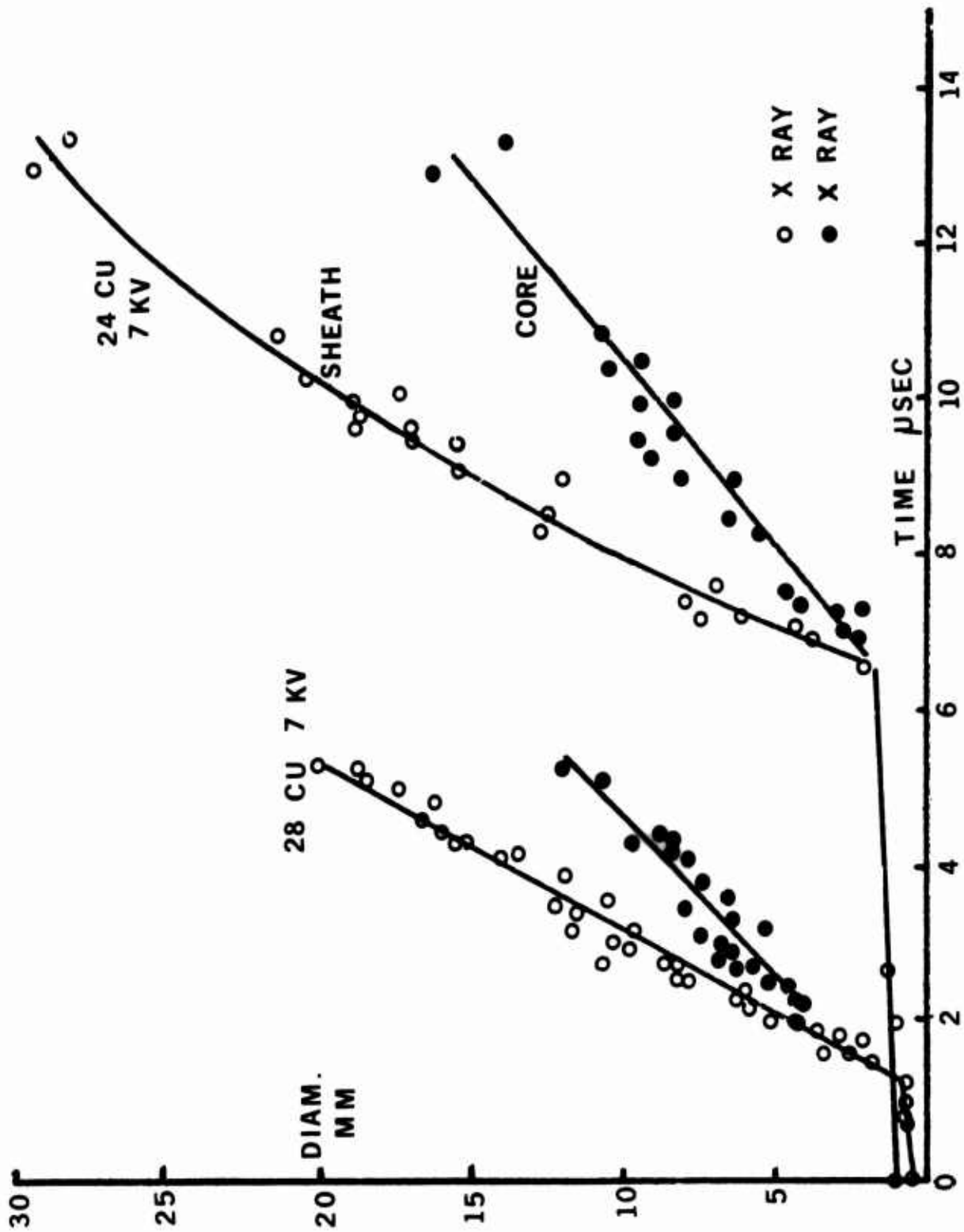


Figure 15. The diam versus time curves for 0.4 and 0.5 mm diam copper wire, 5 cm long, exploded at 7 kV. The two curves have been placed on the same scale to show the similarity in slopes.

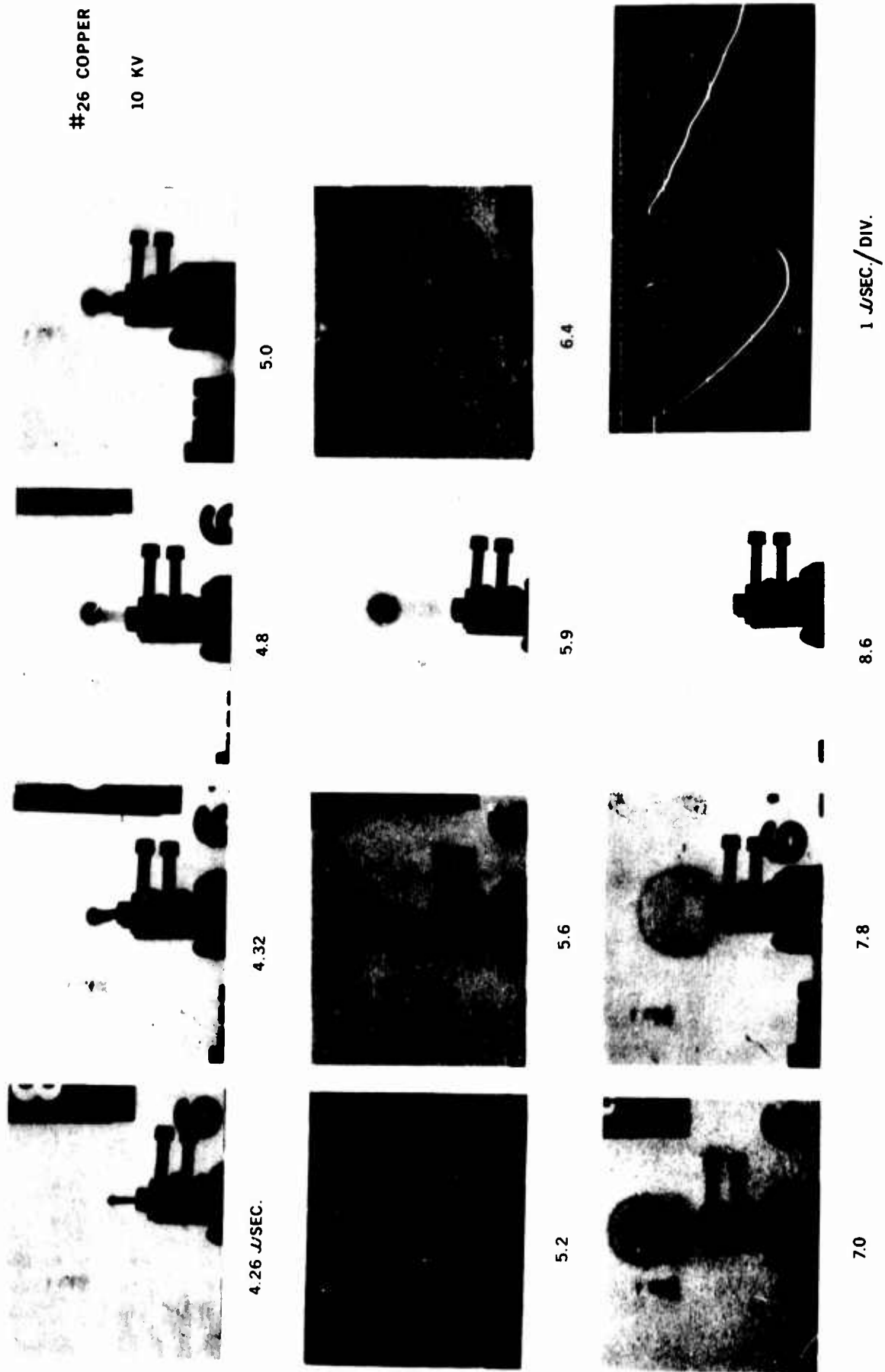


Figure 16. Axial radiographs for 0.4 mm diam copper wire 5 cm long exploded at 10 kV with a 45 mfd capacitor bank. Delays are with respect to the beginning of current.

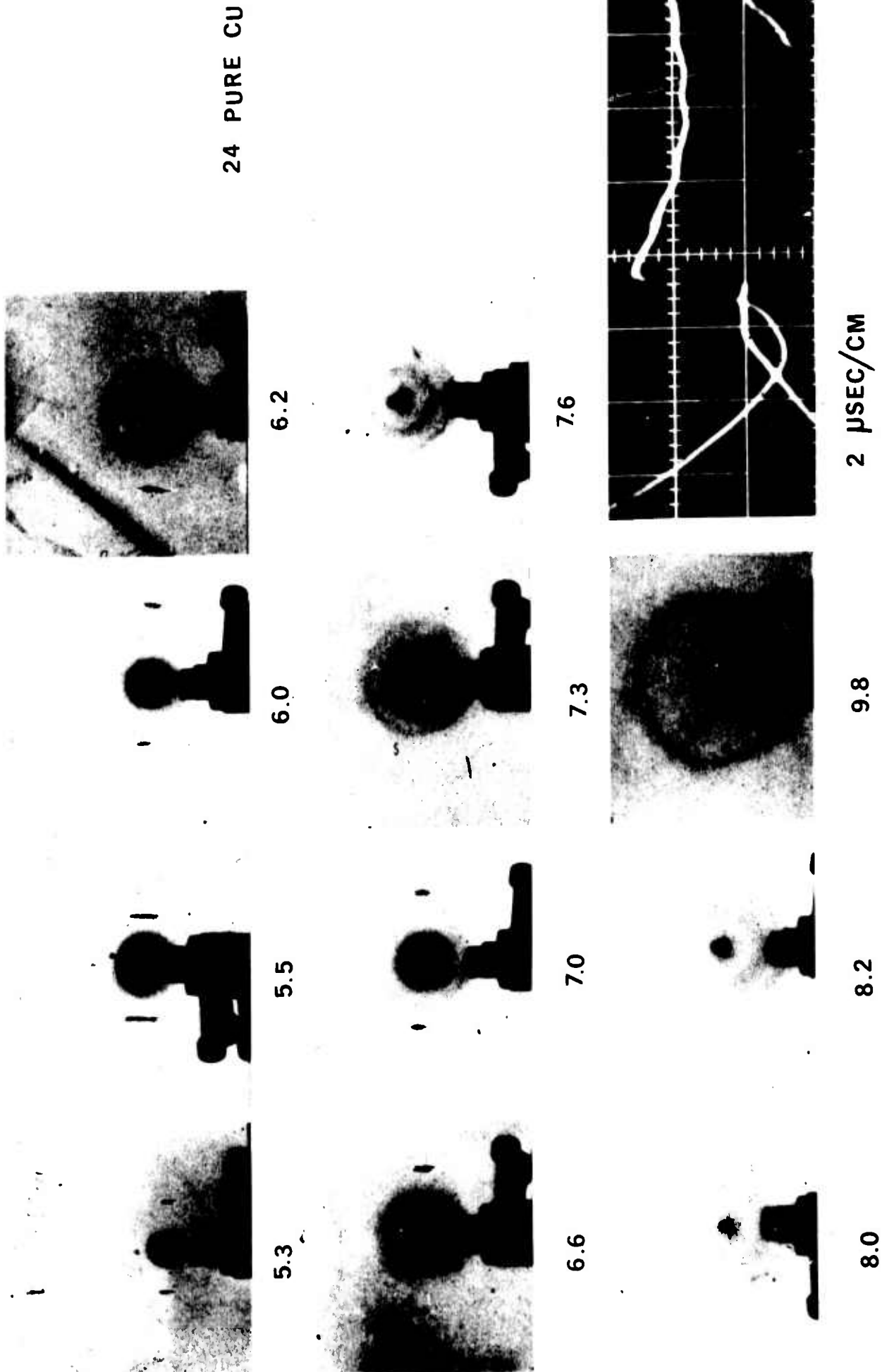


Figure 17 Axial radiographs for 0.5 mm diam copper wire exploded at 7 kV. They show the troublesome end effects, which show up as a small dense core which does not expand. This is due primarily to the low initial voltage used.

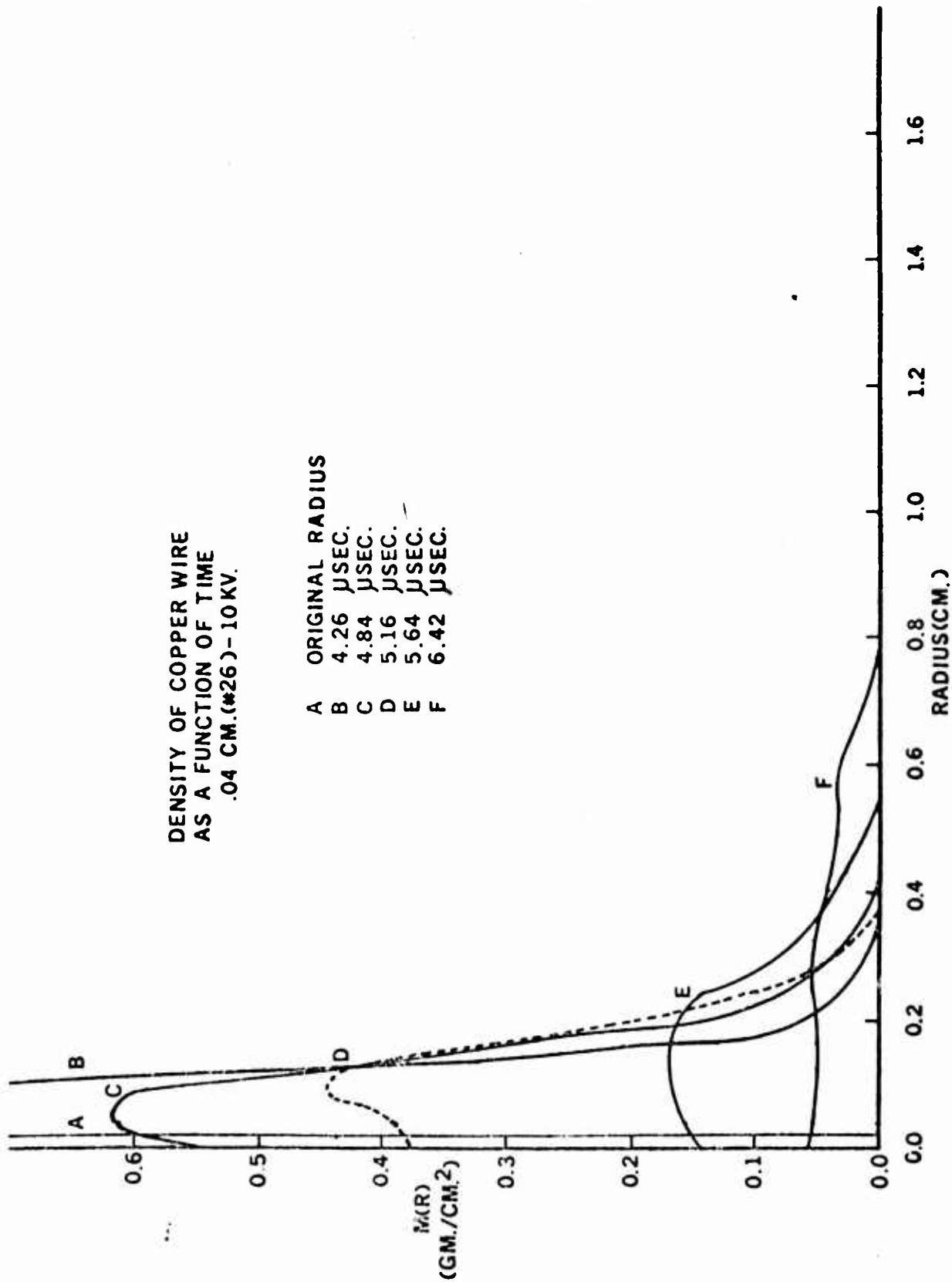


Figure 18 The density of 0.4 mm diam copper wire, 5 cm long, exploded at 10 kV, represented as a function of radius and time. Selected curves are shown for clarity.

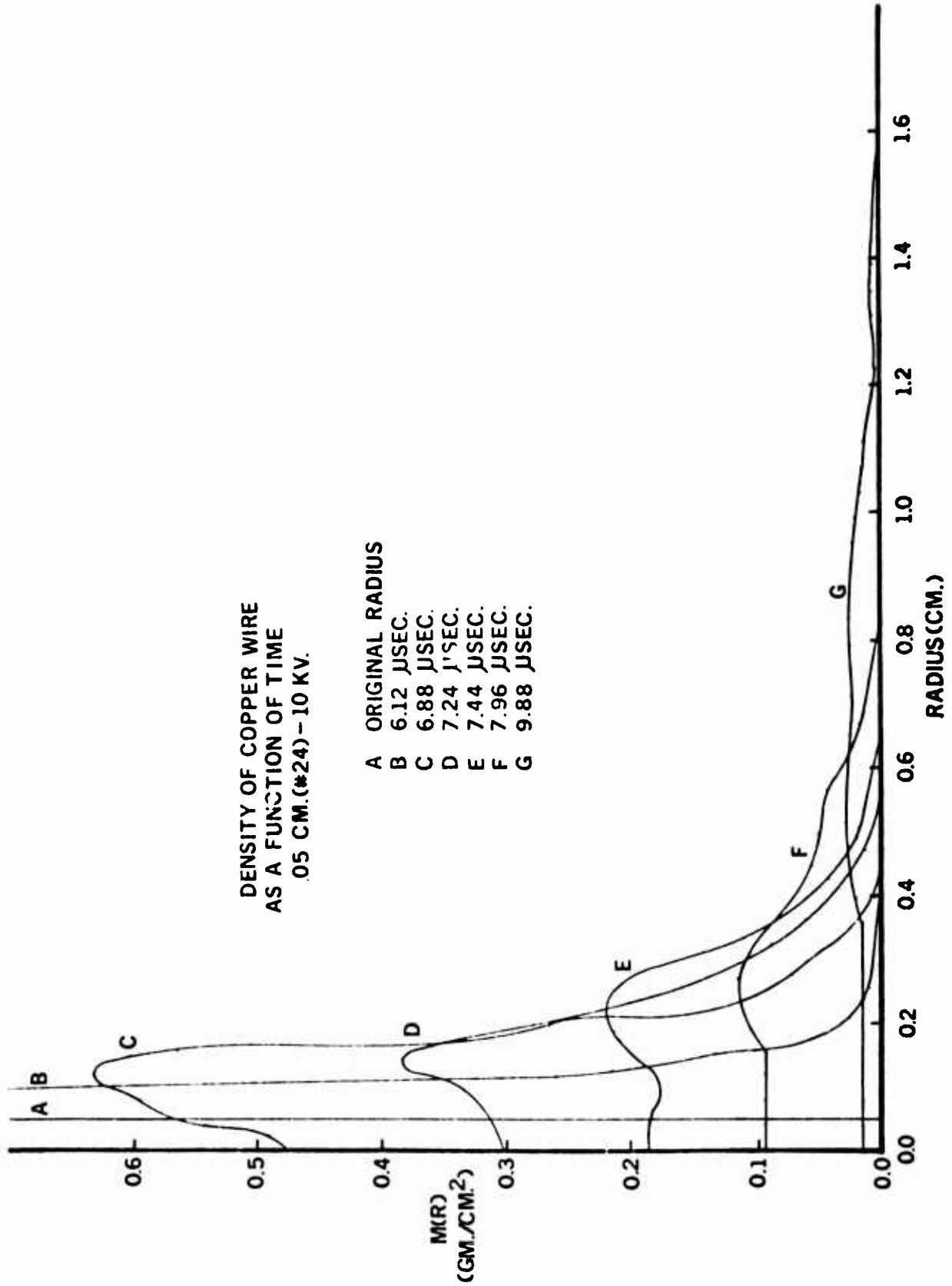


Figure 19 The density of 0.5 mm diam copper wire, 5 cm long, exploded at 10 kV, represented as a function of radius and time. Selected curves are shown for clarity.

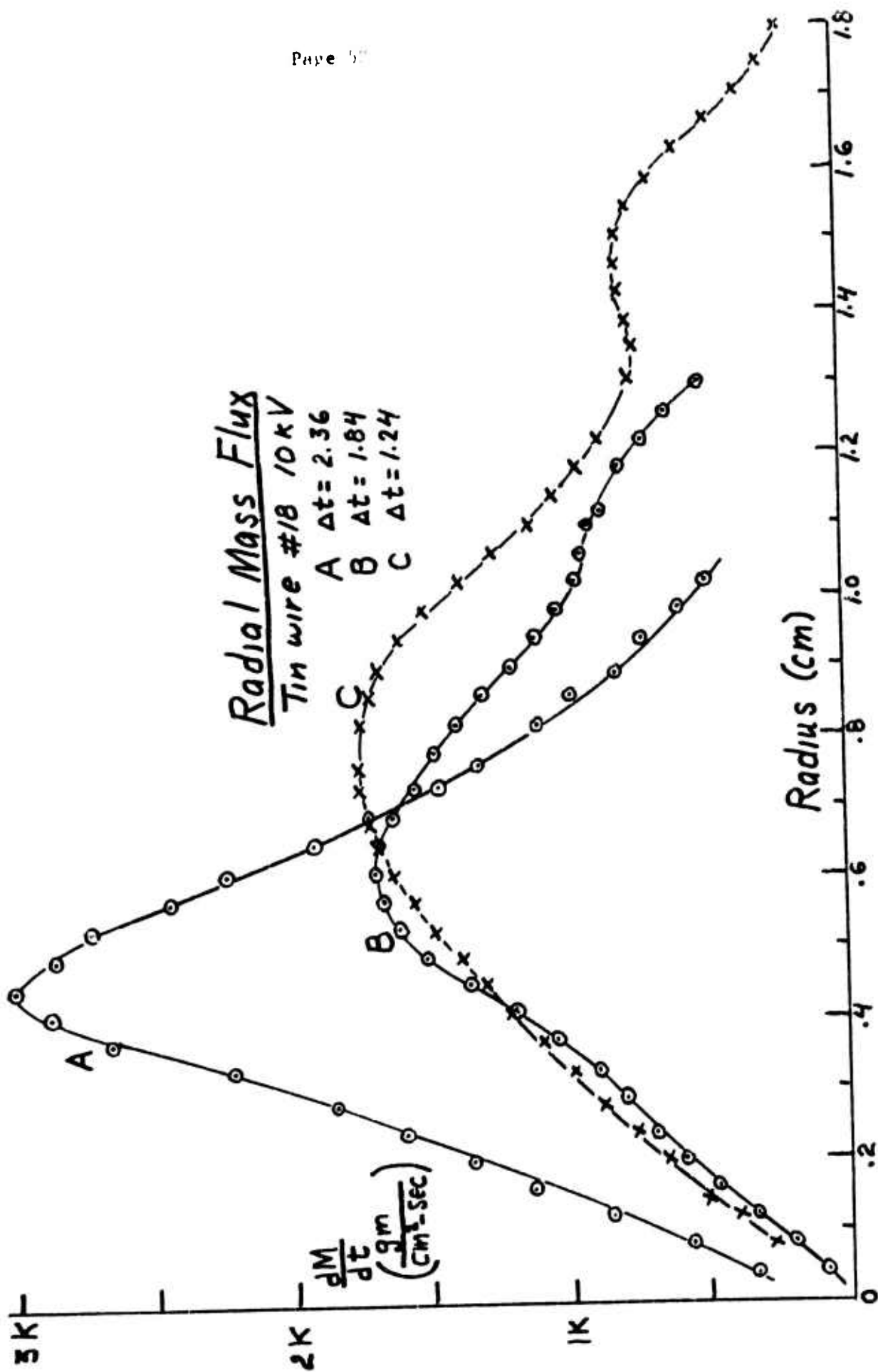


Figure 20 The radial mass flux for 1 mm diam tin wire as a function of radius and time.
Time in microseconds.

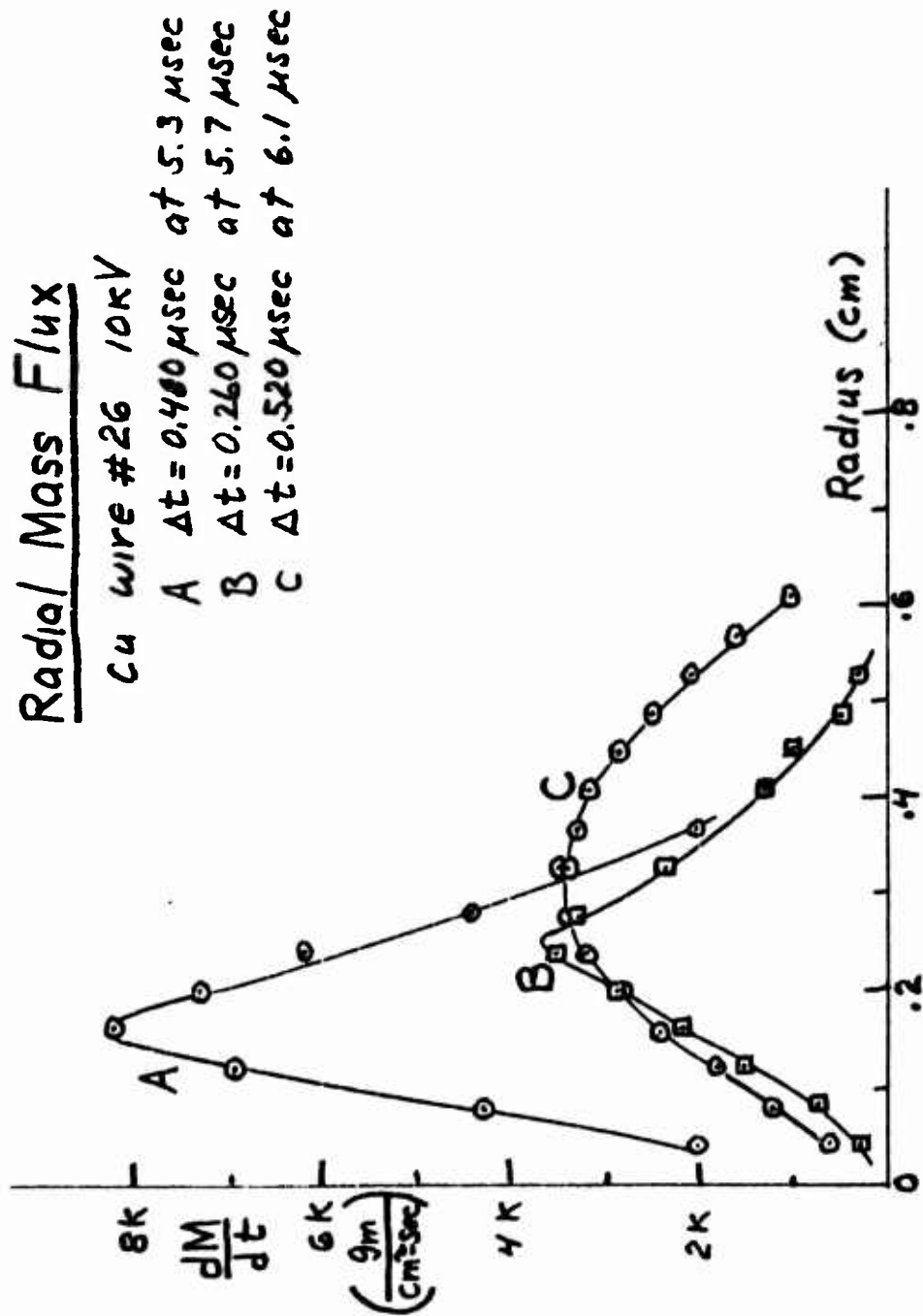


Figure 21 The radial mass flux for 0.4 mm diam copper wire as a function of radius and time. Time in microseconds.

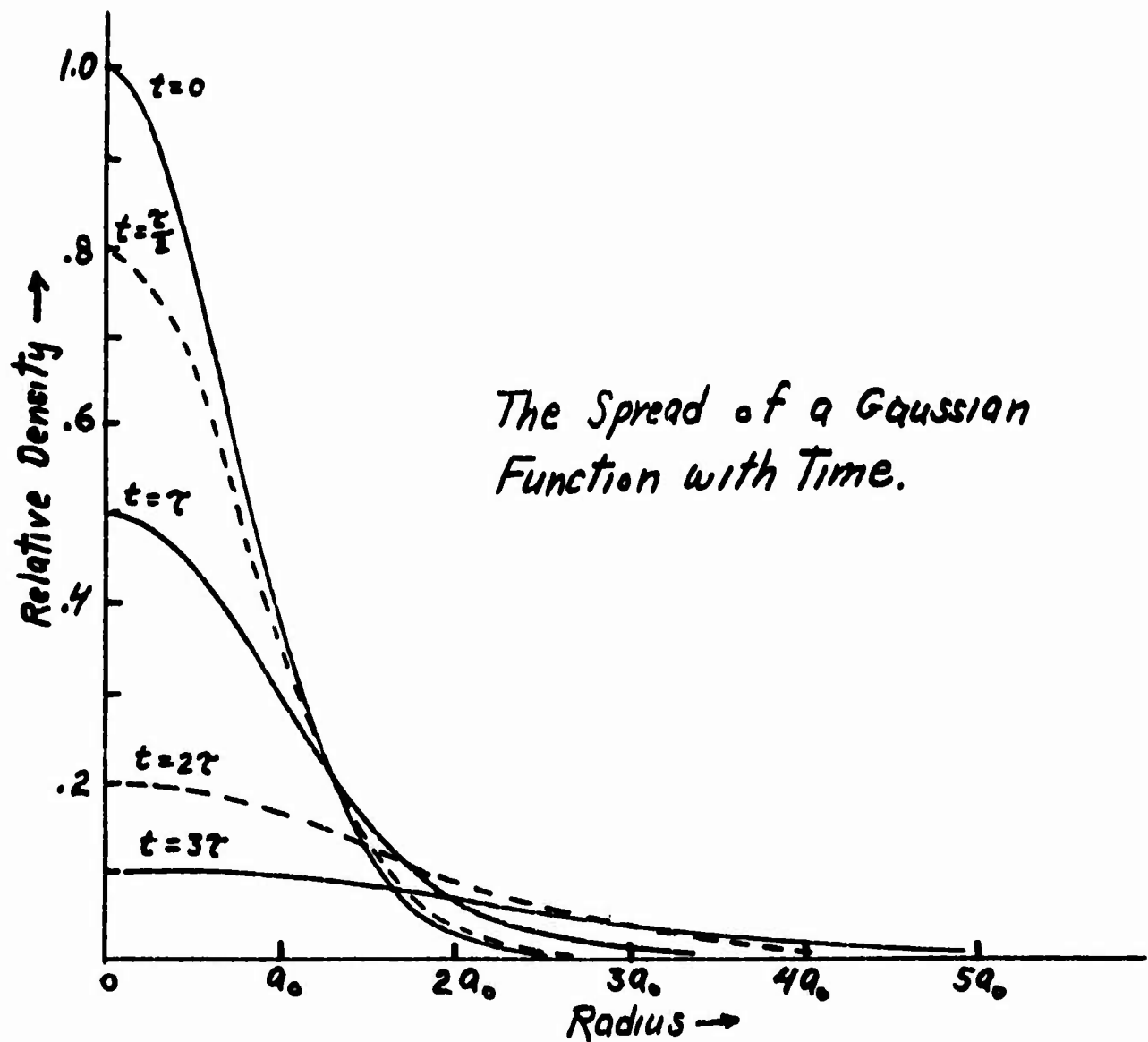


Figure 22 The spread of a gaussian as a function of time.

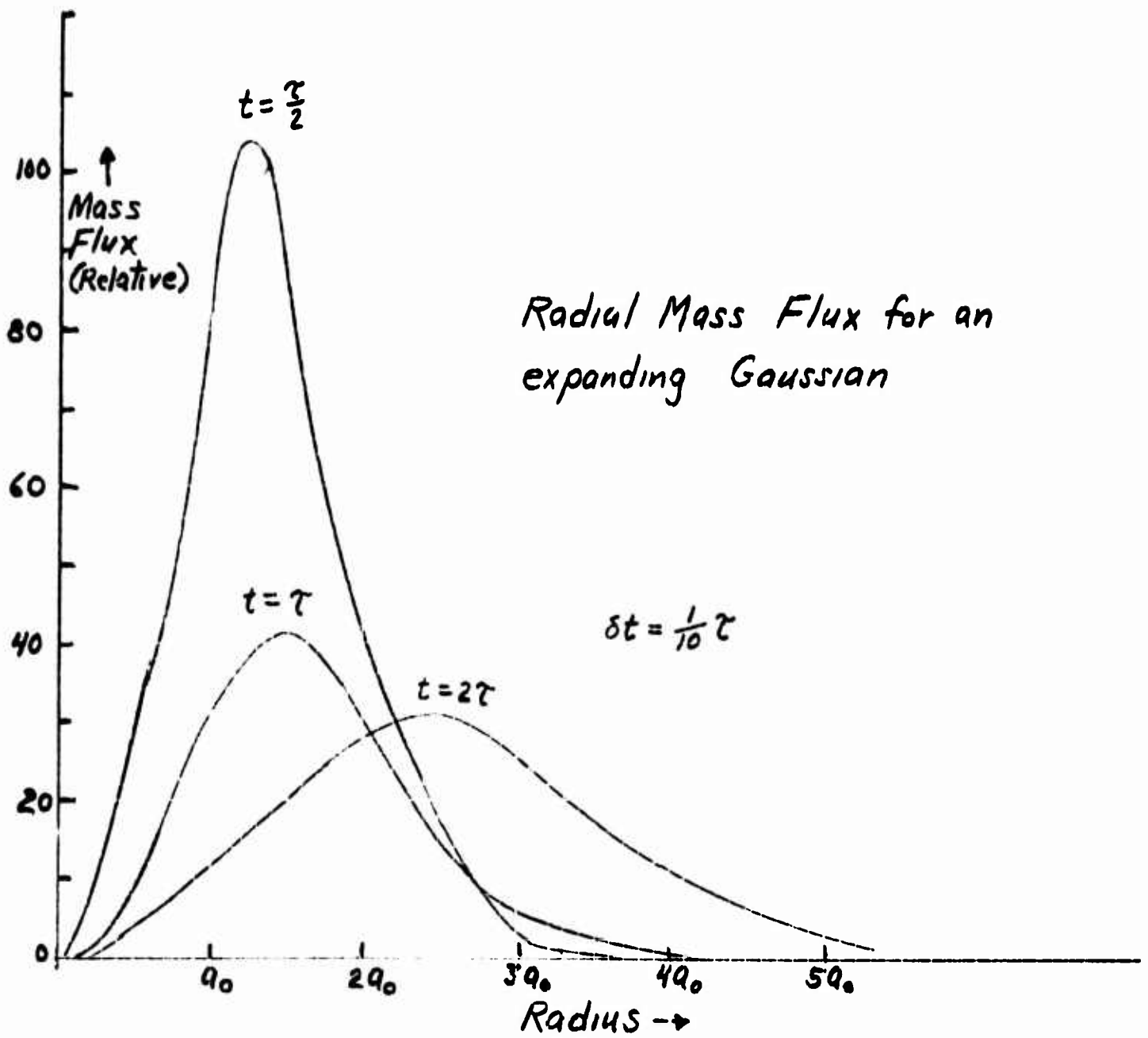


Figure 23 The radial mass flow calculated for an expanding gaussian.

OPTICAL PYROMETER

Introduction

The research on a three-color, fast response optical pyrometer is based on preliminary work initiated by J. L. Bohn, O. P. Fuchs, and R. K. Morton in Air Force Contract No. 19(604)-3076 (Ref. 1). The development has progressed to the point where a breadboard model has been used to obtain results for exploding wires. It involves the simultaneous sampling of the spectrum at three wavelengths and the electronic processing of the involved signals so that a resultant voltage displayed on a cathode ray oscilloscope will be proportional to the instantaneous temperature of the source.

Discussion of Method

The double ratio method used here was derived in Reference 1. In the course of the development, it was deemed practical to try to obtain the ratios by means of a logarithmic system, rather than a linear system. This would then involve differential amplifiers, rather than multipliers, see reference 3 for the discussion of this point. The basic approach centers upon a logarithmic photometer design developed by R. Zatzich at AFCRL, reference 2.

In the double ratio method, the temperature can be solved for producing the following working equation,

$$T \text{ (Kelvin)} = \frac{C_2 \left(\frac{2}{\lambda_2} - \frac{1}{\lambda_1} - \frac{1}{\lambda_3} \right)}{\ln \left(\frac{i_1 i_3}{i_2^2} \right) - 5 \ln \left(\frac{\lambda_2^2}{\lambda_1 \lambda_3} \right) - \ln \left[\tau(\lambda_1, \lambda_2, \lambda_3) \frac{F_1 C_1 / F_2 C_2}{F_3 C_3 / F_3 C_3} \right]} \quad (1)$$

Where i_1 , i_2 and i_3 , in the denominator are the ratios of intensities of the light received at wavelengths λ_1 , λ_2 and λ_3 respectively. With the proper selection of wavelengths, i.e. using appropriate filters, all terms other than the first in the denominator, become constants which can be evaluated. The working equation becomes,

$$T = \frac{A}{\ln\left(\frac{I_1 I_2}{I_1^2}\right) + B} \quad (2)$$

Labelling the intensities by the respective colors chosen for

$$T = \frac{A}{\ln\left(\frac{RB}{G^2}\right) + B} \quad (3)$$

This last expression relates directly to the three channel color outputs, red (R), green (G), and blue (B). The constants A and B are a function of the wavelengths chosen and the calibration of the circuit can be calculated.

In the device described here, the output is a voltage proportional to the variable term in the denominator $\ln(RB/G^2)$. Thus, if A and B are known, an oscilloscope vertical scale can be calibrated in $^{\circ}K$ from the given information and the voltage range of the output. It should be noted that because of the form of equation (3), the scale will be non-linear, and the voltage representing $\ln(RB/G^2)$ will have definite upper and lower bounds.

Circuit Theory and Calibration

Preliminary work on theoretical development and circuit design is presented in reference 3. The outputs of the logarithmic photometer circuits are proportional to the logarithms of the intensity of the incident radiation. The variable term in equation (3) can be determined by utilization of differential amplifiers, as shown in the block diagram of figure A. The final system for obtaining the ratio is the dotted section in the main schematic circuit diagram of figure D. This system utilized only one differential amplifier. As seen in figure A, the resultant output is $\ln R + \ln B = 2 \ln G$. The dotted insert block in figure D achieves the same output.

The logarithmic output of all three channels was checked by the use of calibrated neutral density filters having logarithmic increments in density. The output should change in linear steps for such an input.

Oscillogram No. 3, in figure B, shows the linearity of the output for the logarithmic attenuation. The highest level is zero attenuation, the second highest is the antilog of 0.3, the third highest is the antilog of 0.6, the fourth highest is the antilog of 0.9, and the lowest is for no light. This is one of three identical channels. In such a representation the more intense radiation produces a positive going signal with respect to the bottom of the well for no signal (the lowest line in No. 3, figure B).

Figure B, Oscillogram No. 1 illustrates the method used for obtaining balanced waveforms. The problem here is that one requires an output with the gate voltages cancelled out. The gated pulse is necessary for the operation of the photometer since it provides a feedback logarithmic control to which is added a voltage produced by the incident light. In the final channel mixing, all pulse amplitudes must cancel, leaving voltages proportional to the logarithm of the desired ratio. Oscillogram No. 2, figure B, shows the cancellation of two gates to form a zero reference level.

The primary gate pulses are generated by a General Radio pulse generator (model 1340). This generator sets the gate sampling time (gate width) for the event. Since the generator output is only 4 volts and the system amplifiers need 40 to 80 volts, an amplifier is shown in figure C, also in the final circuit schematic of figure D.

As was noted, instead of using the three differential amplifiers, as shown in figure A (even though the system works as expected) we are now using an operational amplifier as shown in figure D. Notice that $(1/10) \ln R$ is added to $(1/10) \ln B$, and $(2/10) \ln G$ is subtracted. With identical gate amplitudes fed into all three inputs, the resultant gate pulse is cancelled completely. Because this is now accomplished with only one amplifier, balancing and initial calibration is less critical. It should be noted that in calibrating a channel separately, one need only block off the light from the other two. This retains the cancelling effect of the gates. In preliminary checks of single channels, for proper triggering gate and light response, low voltage exploding wires and short time constant flash tube systems were used.

For example, oscillogram No. 4 in figure B is a 3 cm #40 copper wire exploded at 1800 volts (20Mfd). This was channel #3. The time base was 50 usec/cm., the vertical 20 volts/cm. Oscillogram No. 5 in figure B is a G. E. FT-220 flash tube fired at 1000 volts and .01 ufd. This was channel #2. The time base was 100 usec/cm. The vertical was 20 volts/cm. Oscillogram No. 6 in figure B is an FT-220 flash tube at 1000 volts and .01 ufd., shown on channel #2. Here the gate pulse voltage on the phototube was slightly reduced. The time base has been decreased to 20 usec/cm. and the vertical is 20 volts/cm. A block diagram of the system used to obtain this data is shown in figure E.

A delay unit has been incorporated into the circuit that allows the gate to occur before the flash event occurs. This delay may be set between zero and one millisecond, as desired. The gate width should be made long enough to incorporate the entire flash event. It should be noted here that proper balance of gate amplitudes must be.

The relative voltages for the three colors at this temperature are red 14.64, green 5.77, and blue 0.917. These are obtained from tabulated normalized values for black body radiation, see Table I under 2800°K. The proper ratio was then adjusted for in the following manner:

<u>2800 degrees Kelvin</u>		
<u>Wavelength</u>	<u>J</u>	<u>(volts) ln J</u>
Red 7031.4 angstroms	14,635	2.68102
Green 5341.4 angstroms	5,772	1.75267
Blue 3941.5 angstroms	0.917	-0.08665

It should be noted that it is necessary to make separate adjustments for cancelling gate signals and to maintain proper Red, Green and Blue light signal amplitudes. Controls for both gate light signal amplitude are shown in figure G.

Using the tabulated values to set up the desired ratio produces the following equation,

$$\ln R + \ln B - 2 \ln G = \quad (4)$$

$$2.68102 + (-0.08665) - 2(1.75267) = -0.91097$$

The voltage for the blue signal (B) is -0.08665 volts and is difficult to measure. However, if one adds $\ln x$ to each term,

$$(\ln X + \ln R) + (\ln X + \ln B) - (2 \ln X + 2 \ln G) = \quad (5)$$

$$\ln(RBX^2/G^2 X^2) = \ln(RB/G^2)$$

which is the desired ratio. In our case, we chose $\ln x = 4$ volts which makes the voltages in eq. (4).

$$6.68102 + 3.91335 - 11.50534 = -0.91097$$

Also, the gate signals for the red and blue are 25 volts, and the green is 50 volts. The final static calibration voltages inputted to the differential amplifier became

$$\text{Red} - 25 + 6.68102 = -18.31898 \text{ volts}$$

$$\text{Green} - 50 + 11.5053 = 38.4947 \text{ volts}$$

$$\text{Blue} - 25 + 3.9134 = -21.0866 \text{ volts}$$

Therefore, eq. (4) becomes,

$$-18.31898 - 21.0866 + 38.4947 = -0.9109 \text{ volts}$$

Figure H shows that the red and blue are negative output gate signals and the green gate is positive at the output of the differential amplifier. The system is thus calibrated for 2800°K at a logarithmic ratio of -0.9109.

Figure K is a diagram showing the placement of calibration lamp, triggering lamp for static measurements, rotating wheel, and amplifiers. Figures L, M and N are photos of the system proper.

Results

Figure I is data for a No. 24 copper wire exploded at 10kV. Oscillogram A is the temperature waveform and B is the corresponding current waveform. Both have a 10 microsecond/cm time base. The oscillograms have been aligned so that they have the same time axis. Both vertical sensitivities are 0.5 volts/cm. The vertical scale for the temperature waveform is shown calibrated in figure J. As can be seen, the lower temperature region is stretched out, and the high

temperature region is compressed. A temperature lower than 1800°K was not recorded because of signal sensitivity problems, which can be corrected. This represents an instantaneous measure of the surface temperature of an exploded wire in the solid-liquid-vapor phases. It is believed that the sudden high temperature indication, marked by the arrow in figure I, is due to a characteristic arc that forms on the surface of the vapor cloud in such explosions.

TABLE I

*(n) = power of 10 multiplier

<u>Wavelength</u>	<u>1800</u>	<u>2000</u>	<u>2200</u>	<u>2400</u>	<u>2600</u>
7031.4	2.5399(-1)*	7.888(-1)	1.9969(0)	4.332(0)	8.343(0)
5341.4	2.9271(-2)	1.2806(-1)	4.2954(-1)	1.1797(0)	2.7796(0)
3941.5	7.2919(-4)	5.3700(-3)	2.7531(-2)	1.0776(-1)	3.4016(-1)

<u>Wavelength</u>	<u>2800</u>	<u>3000</u>	<u>3200</u>	<u>3500</u>	<u>4000</u>
7031.4	1.4635(1)	2.3826(1)	3.6504(1)	6.3215(1)	1.3168(2)
5341.4	5.7720(0)	1.0885(1)	1.9080(1)	3.9151(1)	1.0200(2)
3941.5	9.1657(-1)	2.1570(0)	4.5607(0)	1.1986(1)	4.3516(1)

<u>Wavelength</u>	<u>5000</u>	<u>6000</u>	<u>8000</u>	<u>10,000</u>	<u>15,000</u>
7031.4	3.7033(2)	8.9230(2)	1.8323(3)	3.2385(3)	7.4950(3)
5341.4	3.9437(2)	9.7563(2)	3.0793(3)	6.2710(3)	1.7345(4)
3941.5	2.6560(2)	7.4499(2)	4.1050(3)	1.0459(4)	3.8410(4)

<u>Wavelength</u>	<u>20,000</u>	<u>25,000</u>
7031.4	1.2302(4)	1.7233(4)
5341.4	3.0657(4)	4.5070(4)
3941.5	7.6700(4)	1.2273(5)

TABLE II

The following is a table of Temperature, Ratio and ln Ratio:

Temperature(K)	$\frac{RB}{G^2}$	$\ln \left(\frac{RB}{G^2} \right)$
1800	0.2155	- 1.540
2000	0.2580	- 1.355
2200	0.2980	- 1.210
2400	0.3360	- 1.091
2600	0.3670	- 1.0024
2800	0.4020	- 0.9113
3000	0.4380	- 0.8255
3200	0.4500	- 0.7985
3500	0.4930	- 0.7073
4000	0.5500	- 0.5980
5000	0.6340	- 0.4560
6000	0.6970	- 0.3610
8000	0.7910	- 0.2345
10,000	0.8630	- 0.1473
15,000	0.9580	- 0.0430
20,000	1.0060	+ 0.0060
25,000	1.0400	+ 0.0390

REFERENCES

1. Bohn, J. L. et al, "Research Directed Toward the Attainment and Utilization of High Temperatures - Spectrophotometric Determination of High Temperatures" AFCRC Contract No. 19(604)-3076, Nov. 1960.
2. Zatzick, M. R. "Instrumentation for Geophysics and Astrophysics" AFCRC-TR-58-275, No. 11, Sept. 1959.
3. Korneff, T., "Study of High Energy, High Density Discharges and High Temperature Measurements as Applied to Exploding Wires" AFCRL-67-0276, Final Report, May, 1967.

LIST OF ILLUSTRATIONS

Figure A A block diagram of the ratio forming circuit.

Figure B Oscillograms for the optical pyrometer.

1. The gate voltages for the three channels.
2. Superimposed waveforms showing the cancellation of two gates.
3. The logarithmic response to light intensity of the photometer circuit. Filters with logarithmic changes in density were used.
4. Response of one channel to an exploding wire. The light response is the voltage variation at the bottom of the well.
5. Response of one channel to a flash tube.
6. Same as 5, with horizontal axis expanded.

All horizontal calibrations 100 microseconds/cm except for 6 which was 20 microseconds/cm.

Figure C Gate amplifier inserted between the gate generator and the grids of the gate drivers.

Figure D Schematic of the 3-channel optical pyrometer.

Figure E Block diagram of the system used to obtain light curves for a flash tube and exploding wire.

Figure F Schematic of the power supply for the three-channel optical pyrometer.

Figure G The network inserted between the photomultiplier and logarithmic amplifier to allow one to adjust gate and signal levels independently.

Figure H The signals presented to the differential amplifier in a static calibration for a known temperature source.

Figure I (A) The instantaneous temperature of a 0.5 mm diam copper wire exploded at 10 kV. (B) The corresponding current waveform for the exploding wire.

Figure J The temperature scale superimposed on the temperature curve of figure I. Temperatures below 1800°K were not recorded because of sensitivity problems.

Figure K The test stand and rotating shutter used to calibrate the pyrometer against a known temperature.

Figure L A photograph of the pyrometer and rotating shutter test setup.

Figure M A side view of the equipment diagramed in figure K.

Figure N From left to right, the optical pyrometer optical splitting unit, pyrometer chassis, gate generator, and recording oscilloscope. Units below comprise a small wire exploder used in initial tests.

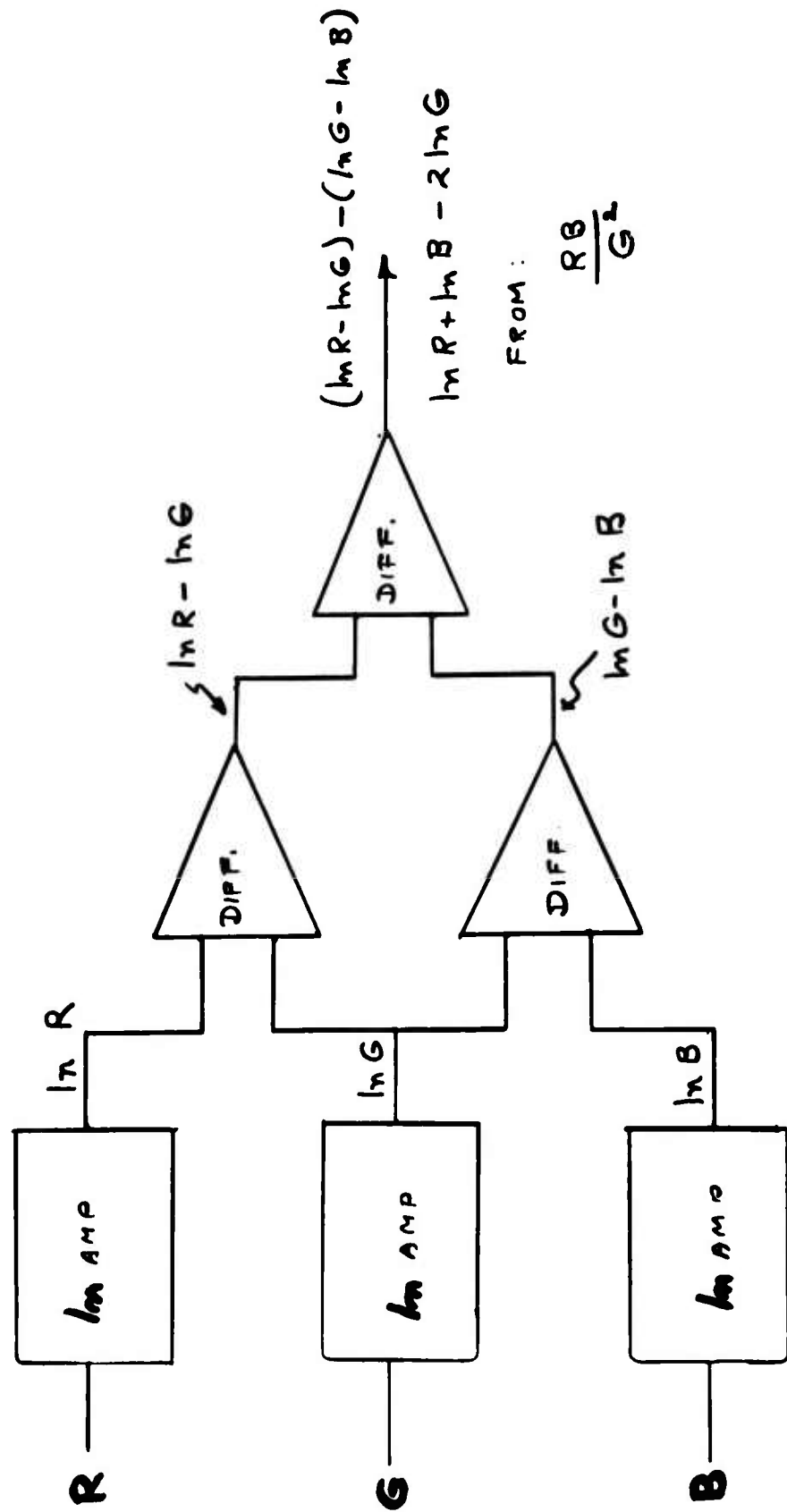
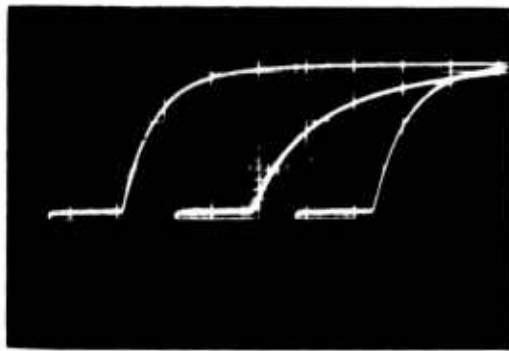
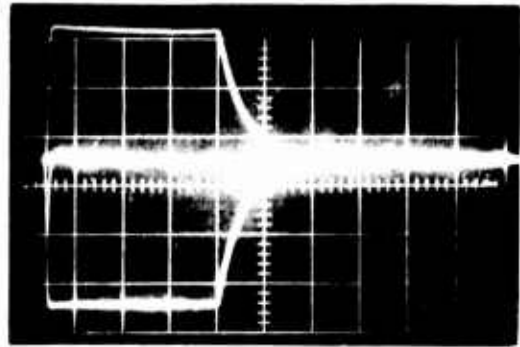


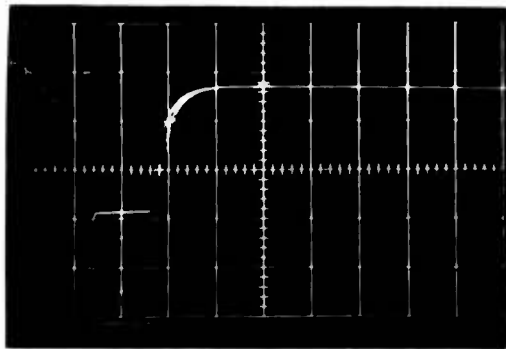
Figure A. A block diagram of the ratio forming circuit.



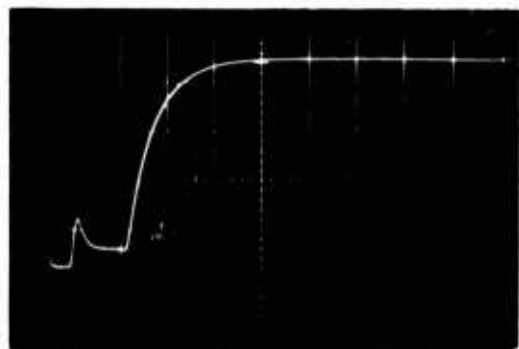
1



2



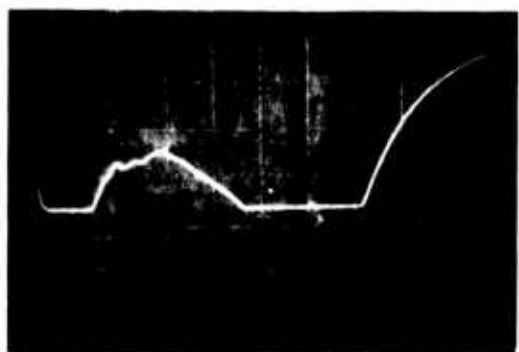
3



4



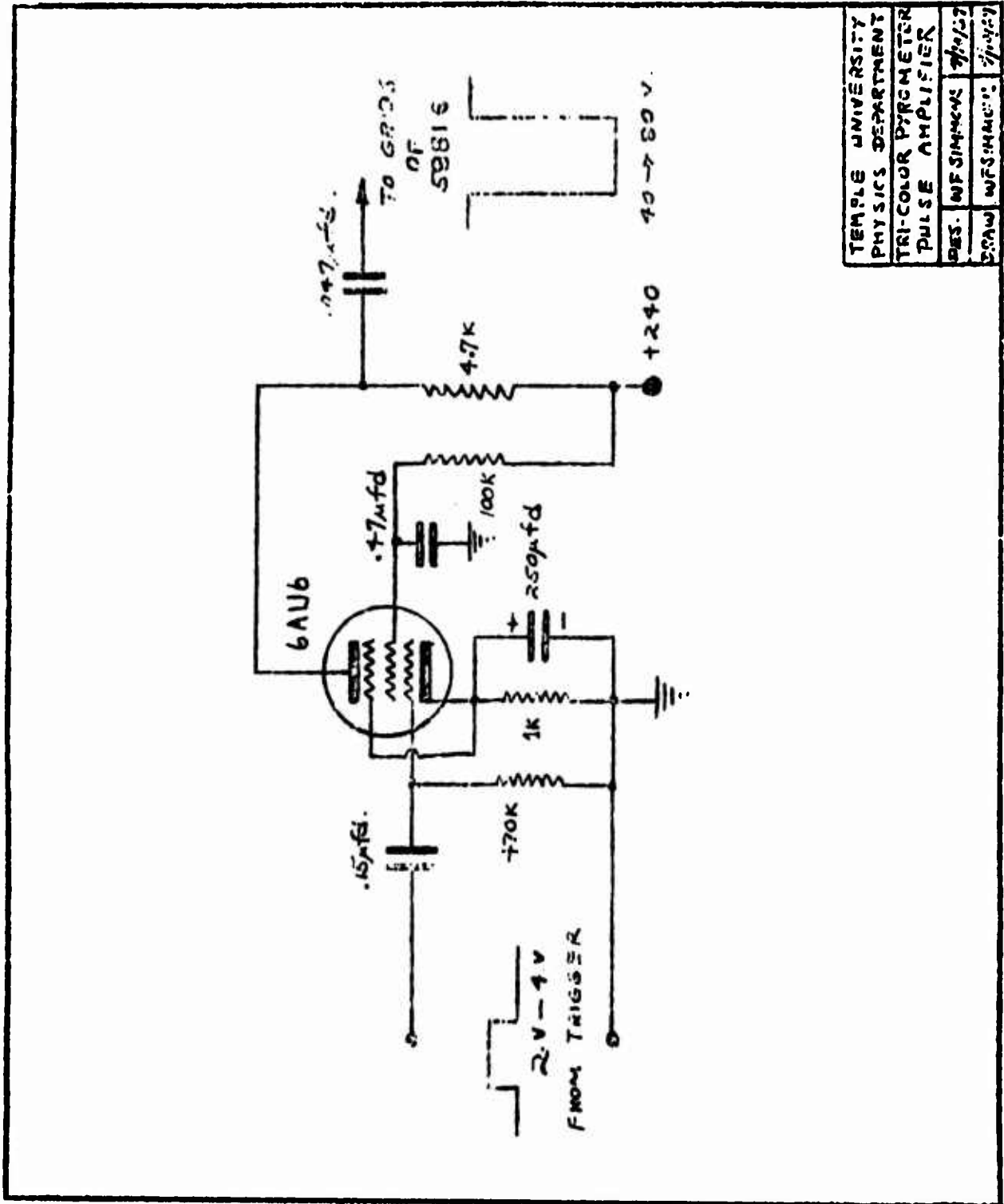
5



6

Figure B. Oscillograms for the optical pyrometer.

1. The gate voltages for the three channels.
 2. Superimposed waveforms showing the cancellation of two gates.
 3. The logarithmic response to light intensity of the photometer circuit. Filters with logarithmic changes in density were used.
 4. Response of one channel to an exploding wire. The light response is the voltage variation at the bottom of the well.
 5. Response of one channel to a flash tube.
 6. Same as 5, with horizontal axis expanded.
- All horizontal calibrations 100 microseconds/cm except for 6 which was 20 microseconds/cm.



TEMPLE UNIVERSITY	PHYSICS DEPARTMENT	TRI-COLOR PYROMETER	PULSE AMPLIFIER
DES.	WFS:MM:K	7/10/57	7/10/57
DSAW	WFS:MM:K	7/10/57	7/10/57

Figure C Gate amplifier inserted between the gate generator and the grids of the gate drivers.

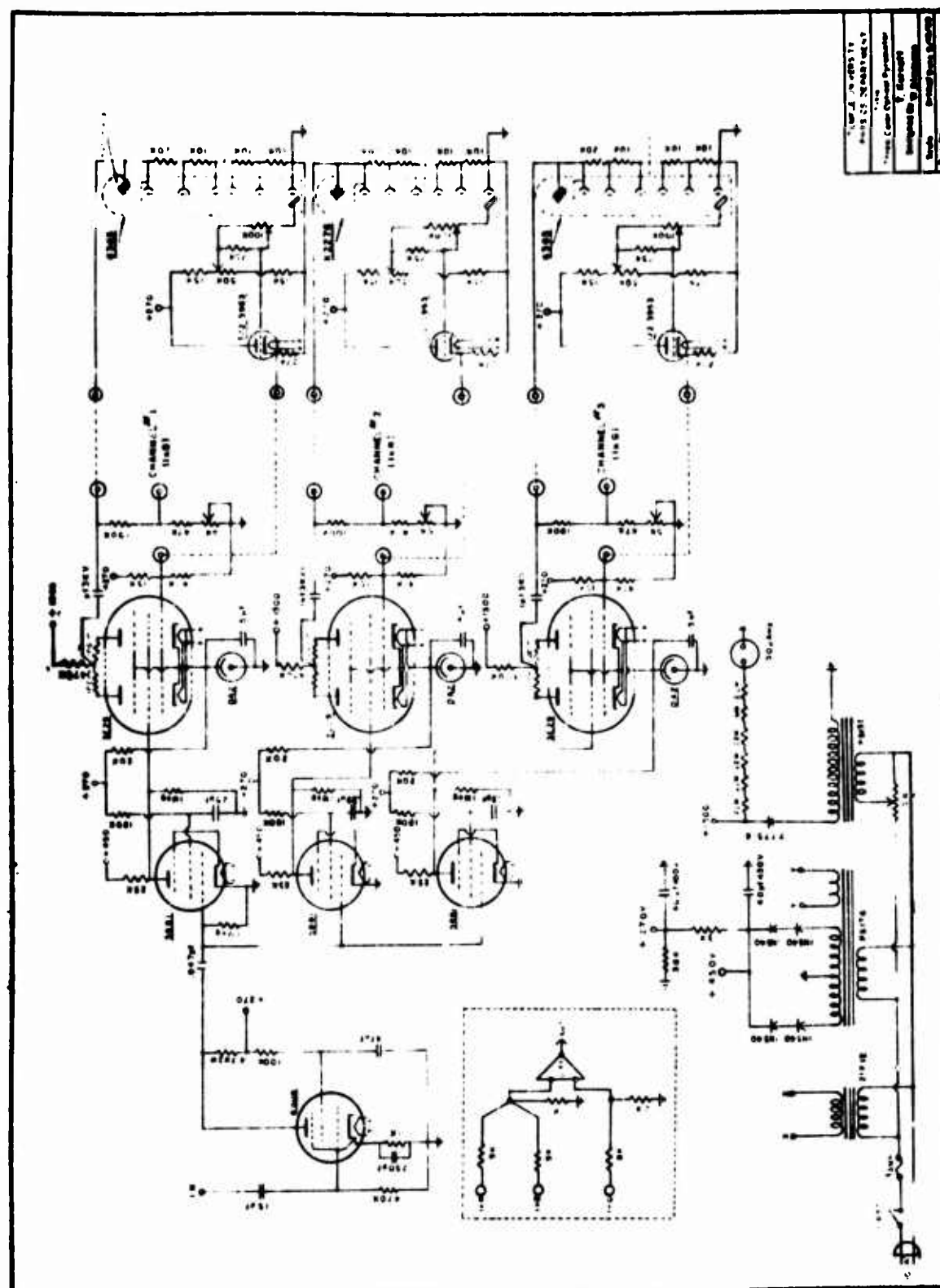


Figure D Schematic of the three-channel optical pyrometer.

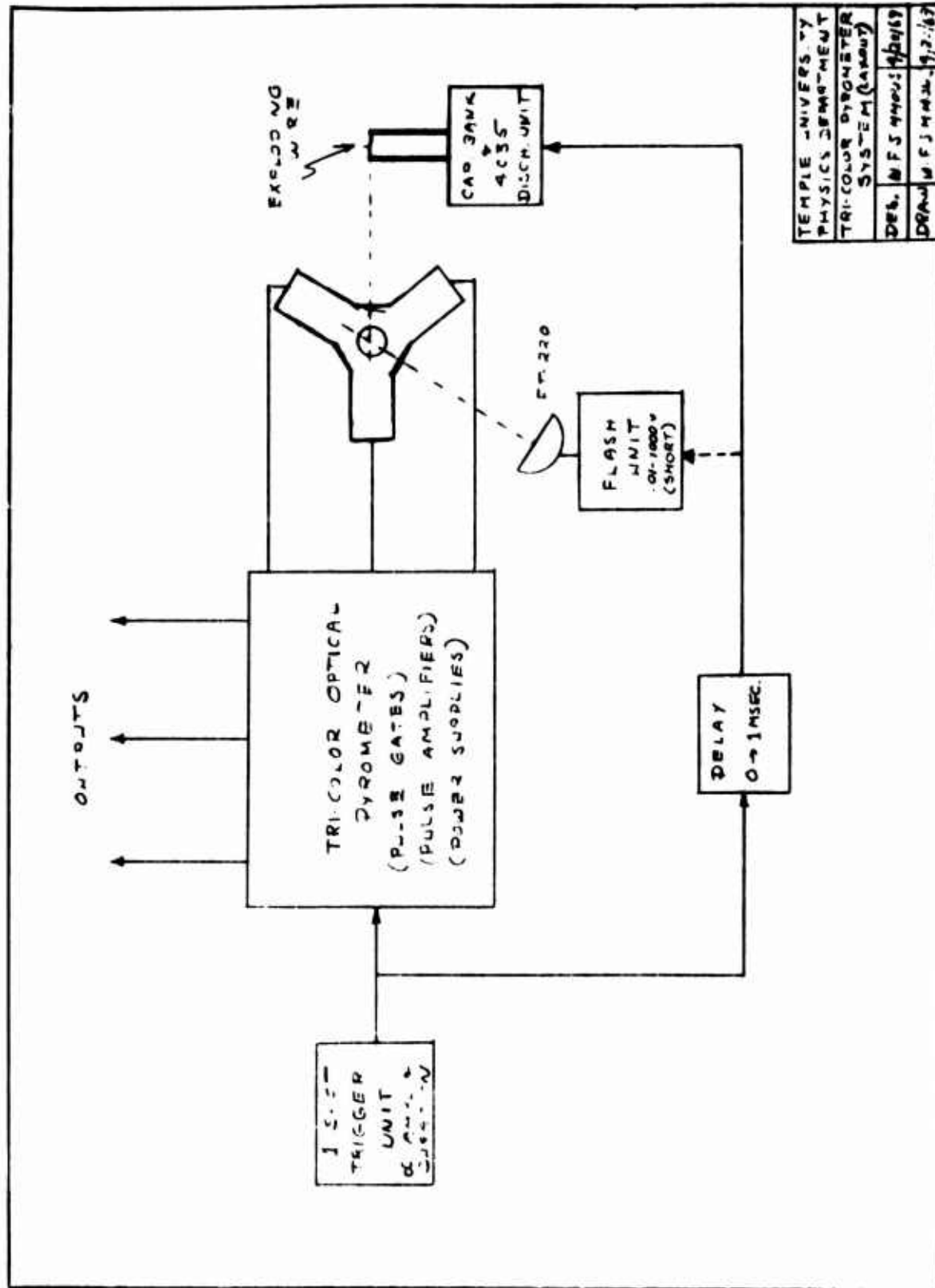


Figure E Block diagram of the system used to obtain light curves for a flash tube and exploding wire.

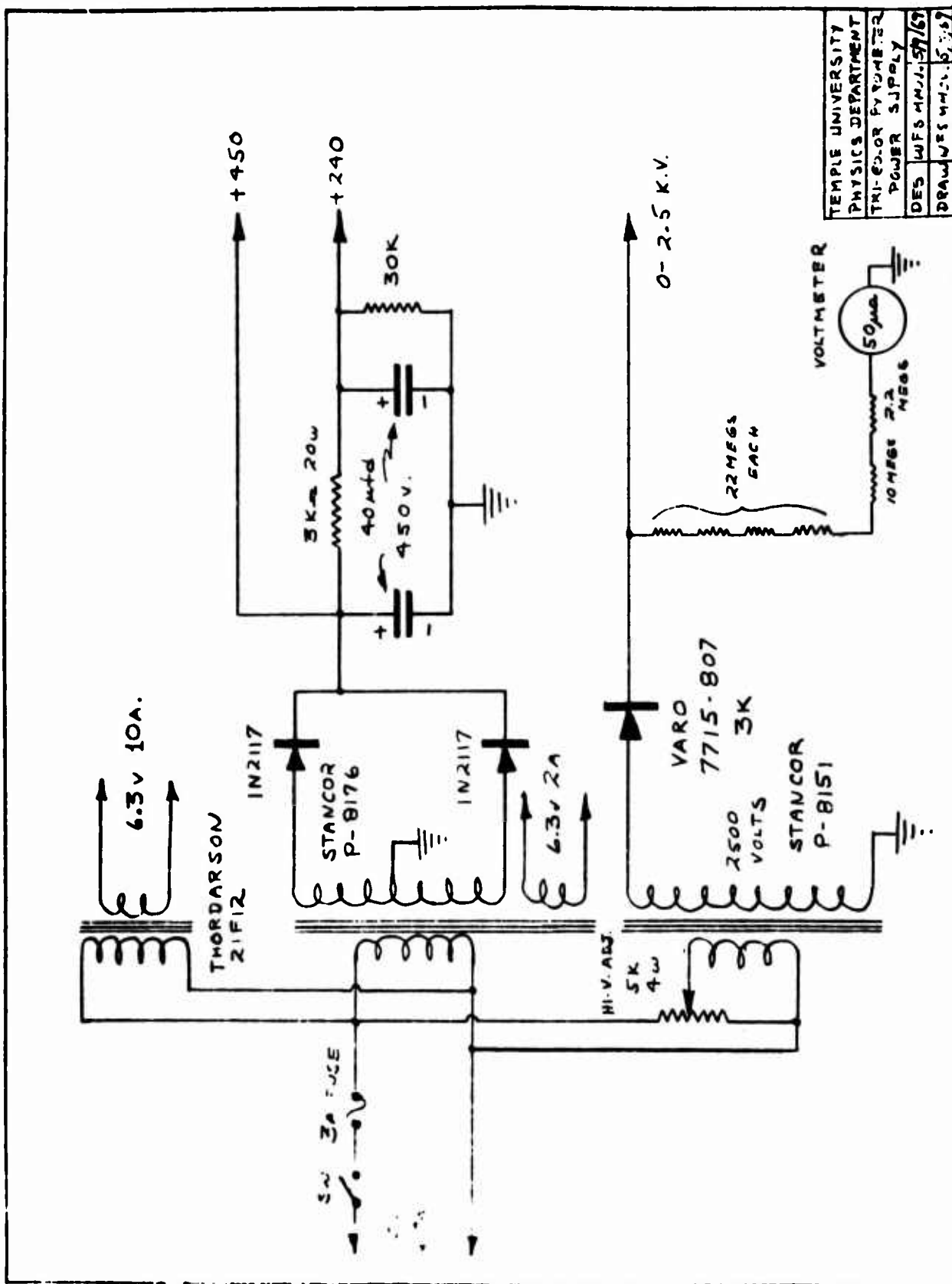


Figure F Schematic of the power supply for the three-channel optical pyrometer.

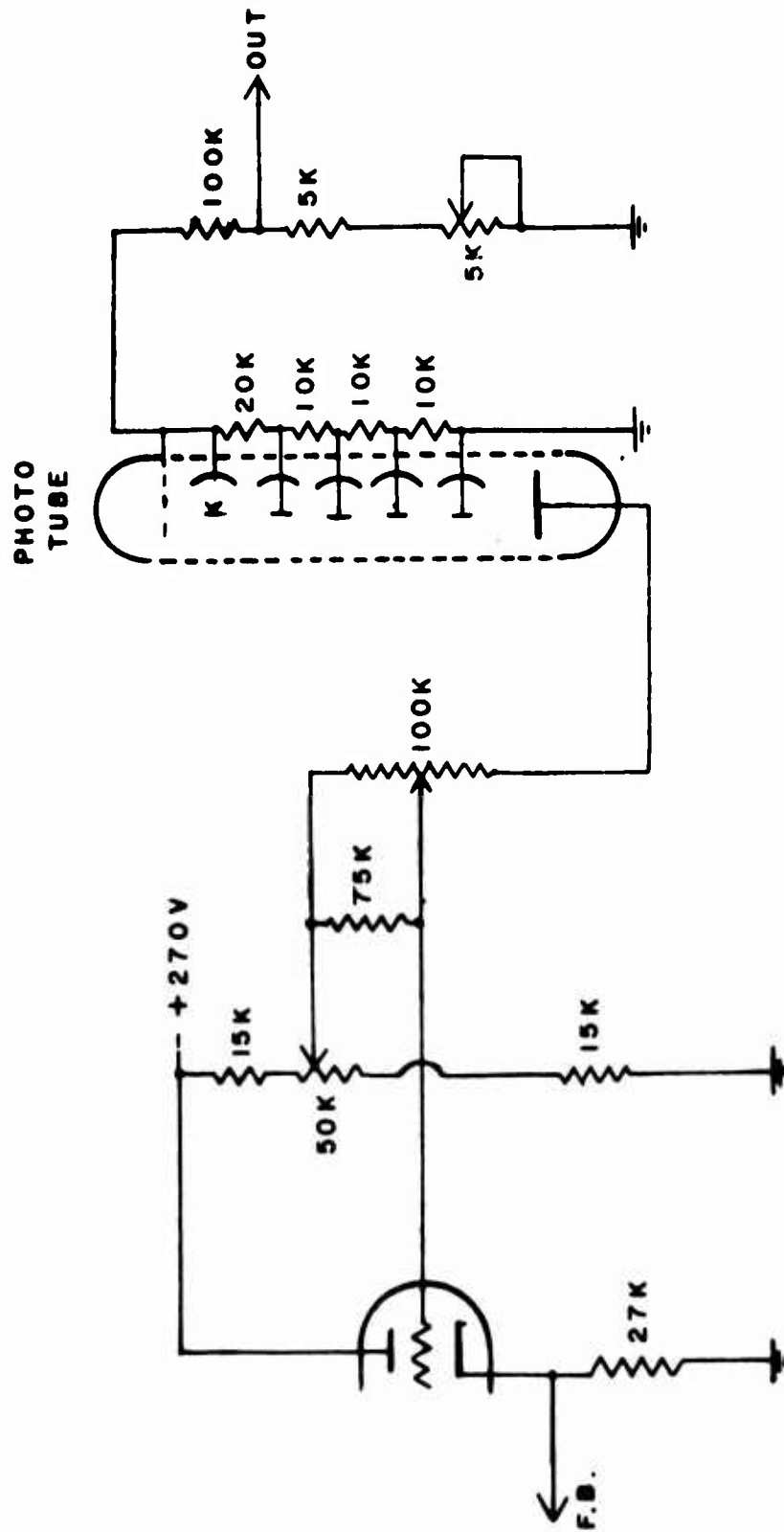
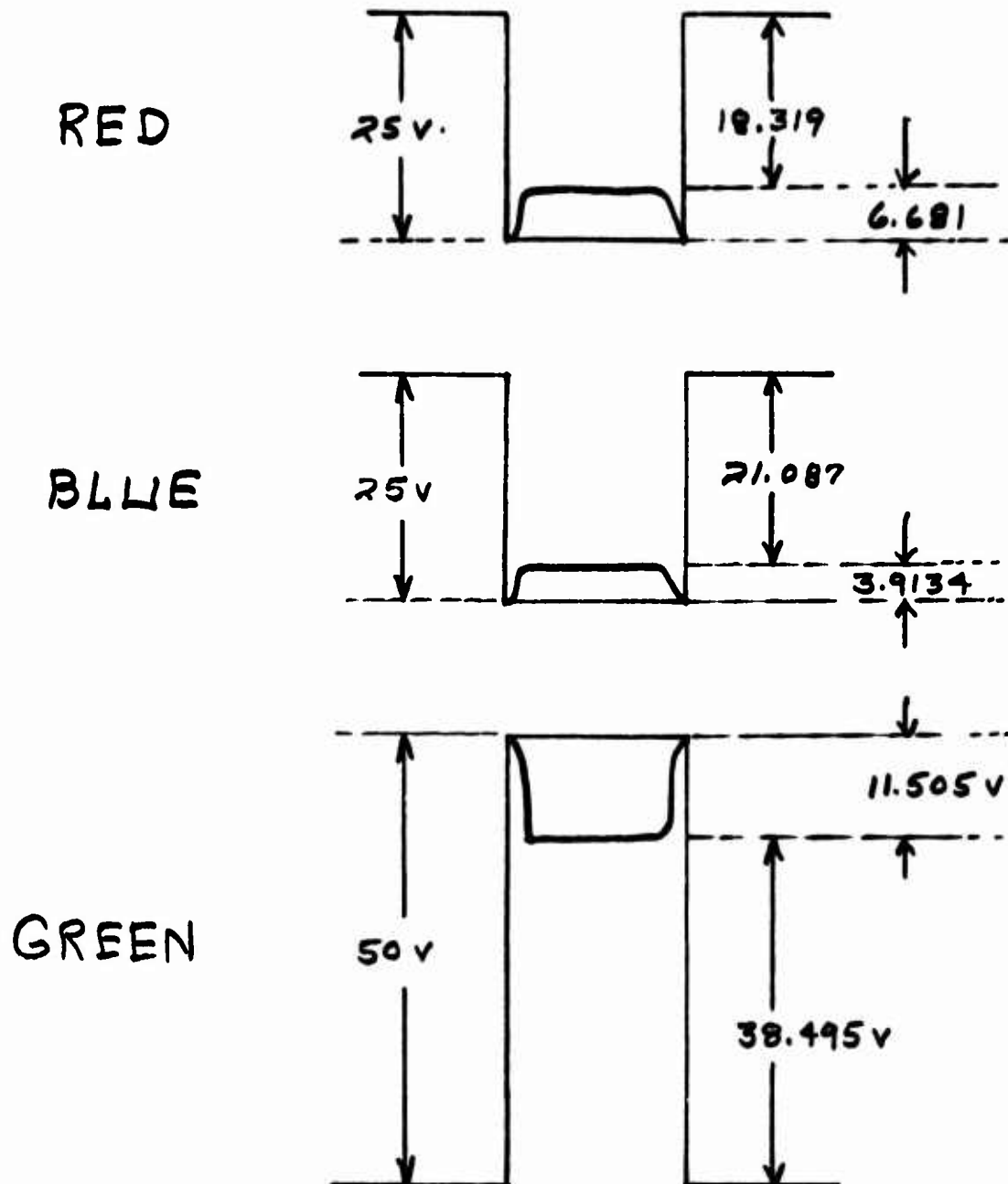


Figure G The network inserted between the photomultiplier and logarithmic amplifier to allow one to adjust gate and signal levels independently.

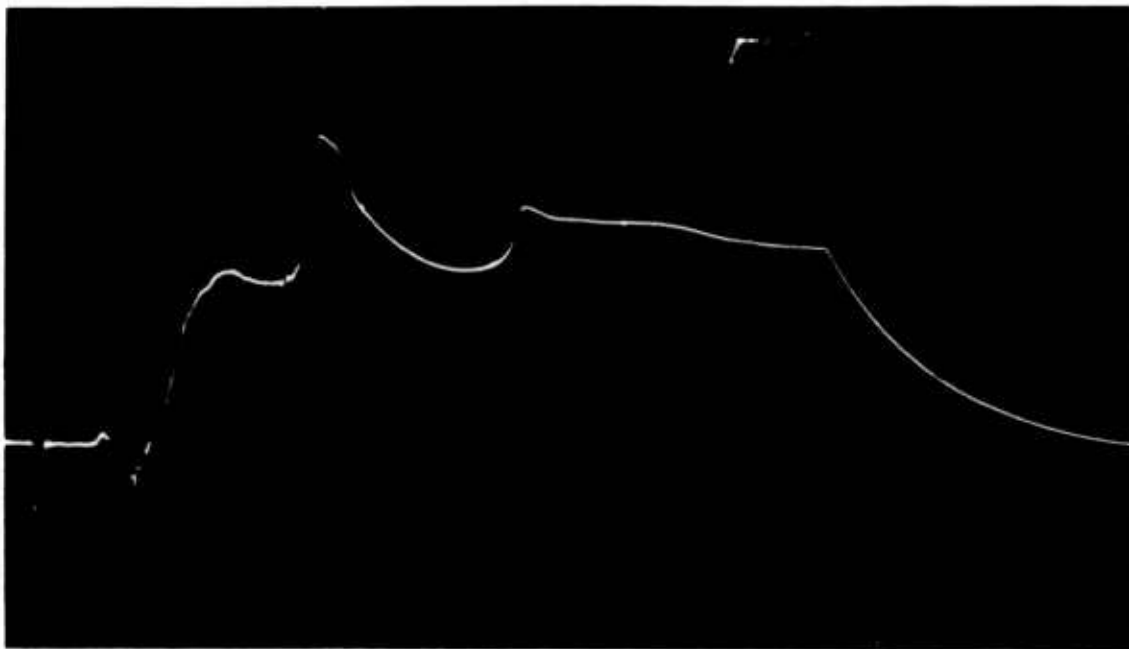
DIFFERENTIAL AMPLIFIER OUTPUT



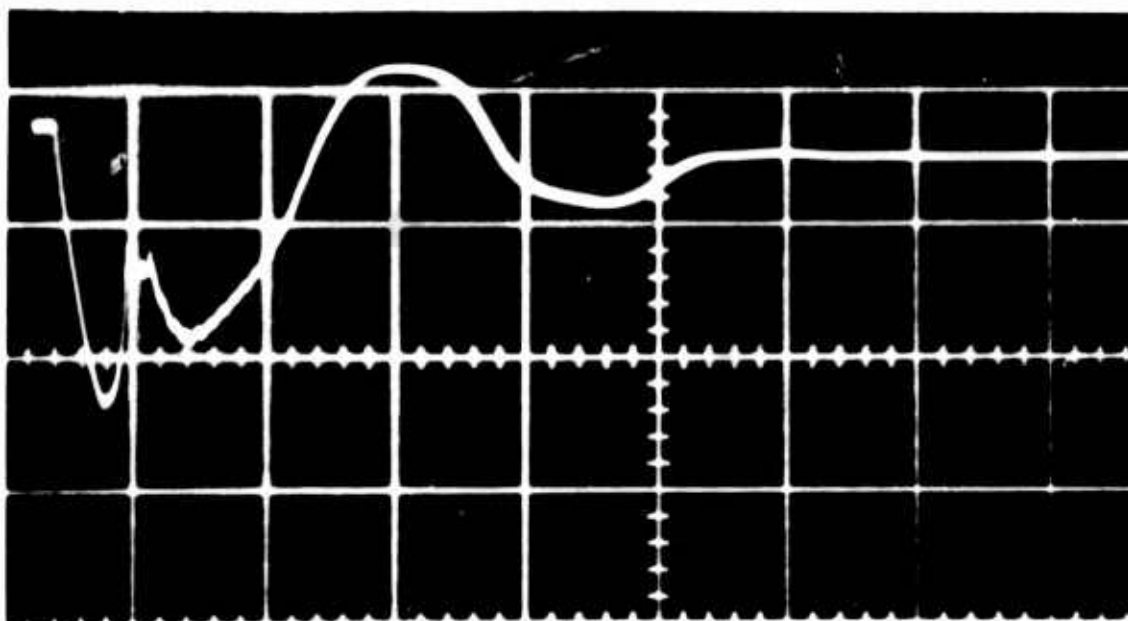
$$-18.319 - 21.0866 + 38.495 = -0.9109$$

(2800°K)

Figure H The signals presented to the differential amplifier in a static calibration for a known temperature source.



(A) Temperature 10 microsec/cm



(B) Current 10 microsec/cm

Figure I. (A) The instantaneous temperature of a 0.5 mm diam copper wire exploded at 10 kV.
(B) The corresponding current waveform for the exploding wire.

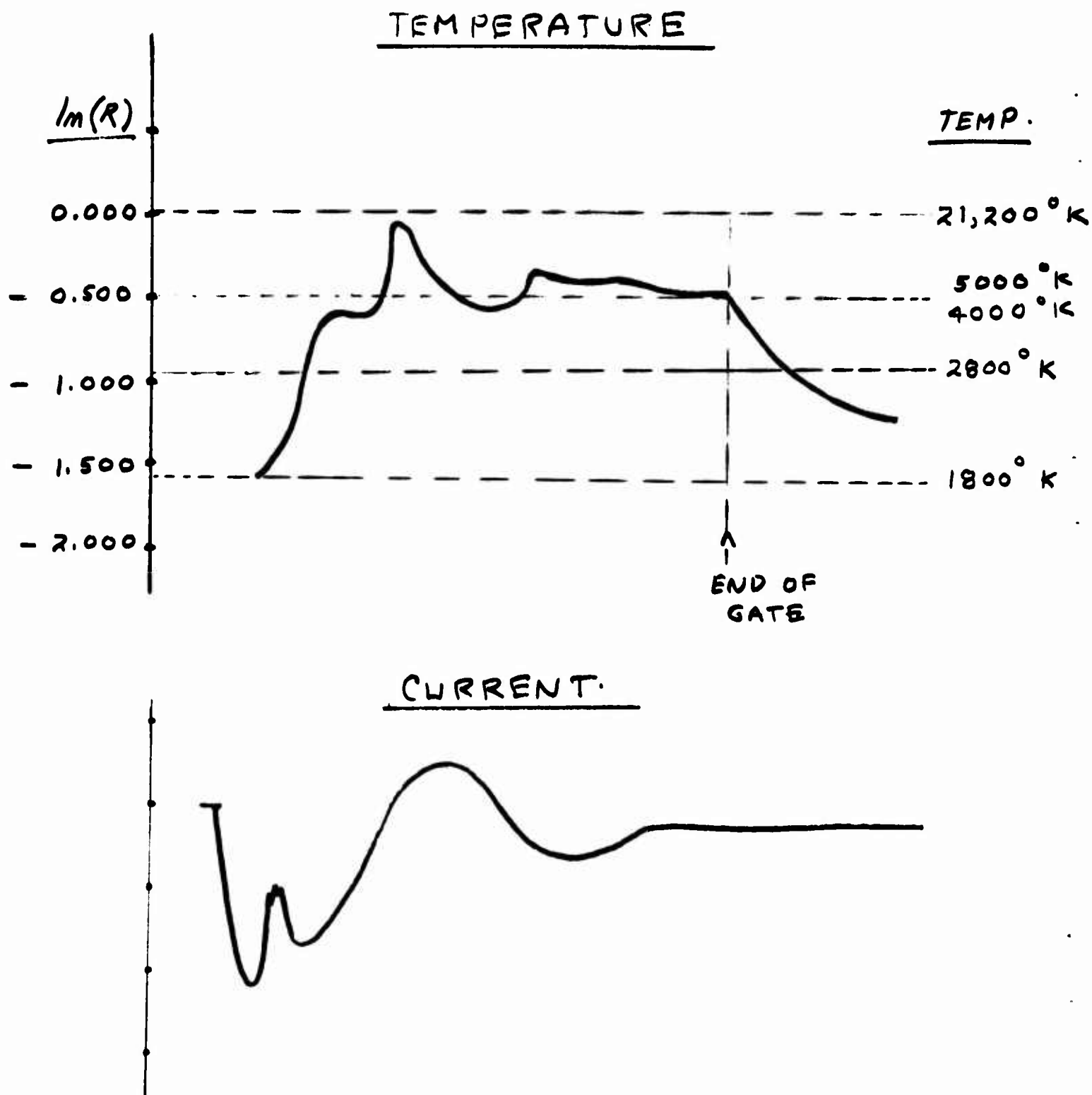


Figure J. The temperature scale superimposed on the temperature curve of Figure I. Temperatures below 1800°K were not recorded because of sensitivity problems. #24 copper wire 10 kV.

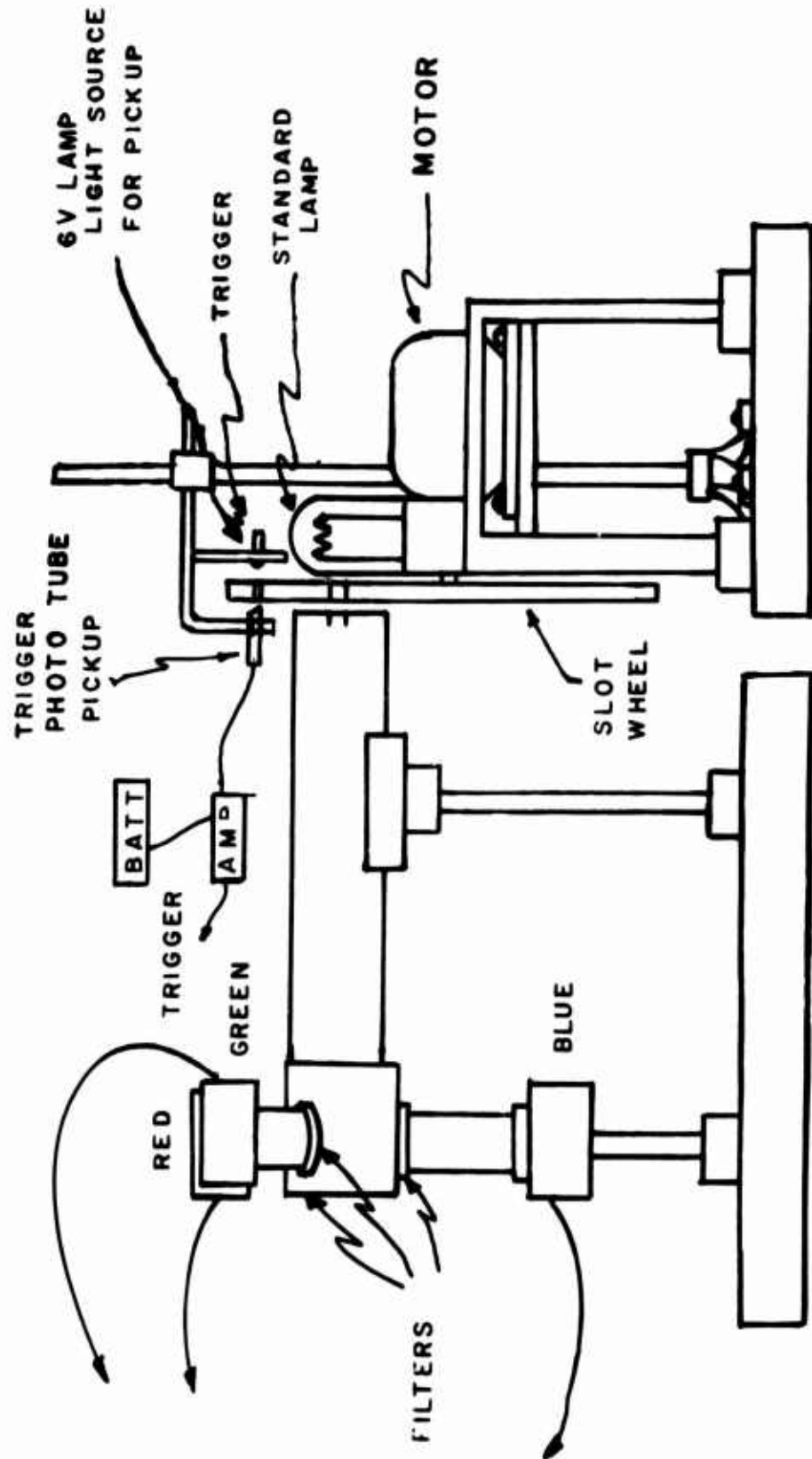


Figure K. The test stand and rotating shutter used to calibrate the pyrometer against a known temperature.

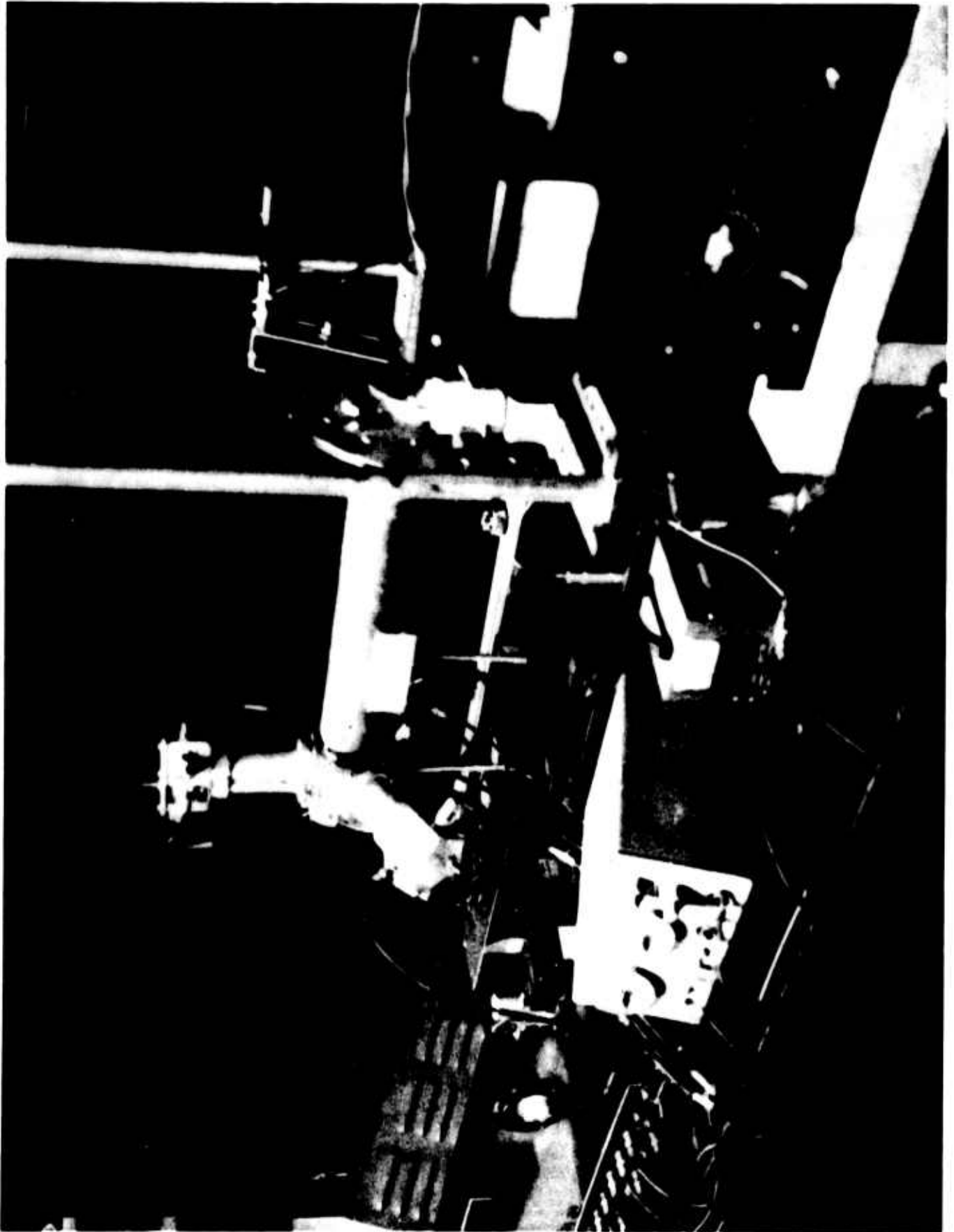


Figure L. A photograph of the pyrometer and rotating shutter test setup.

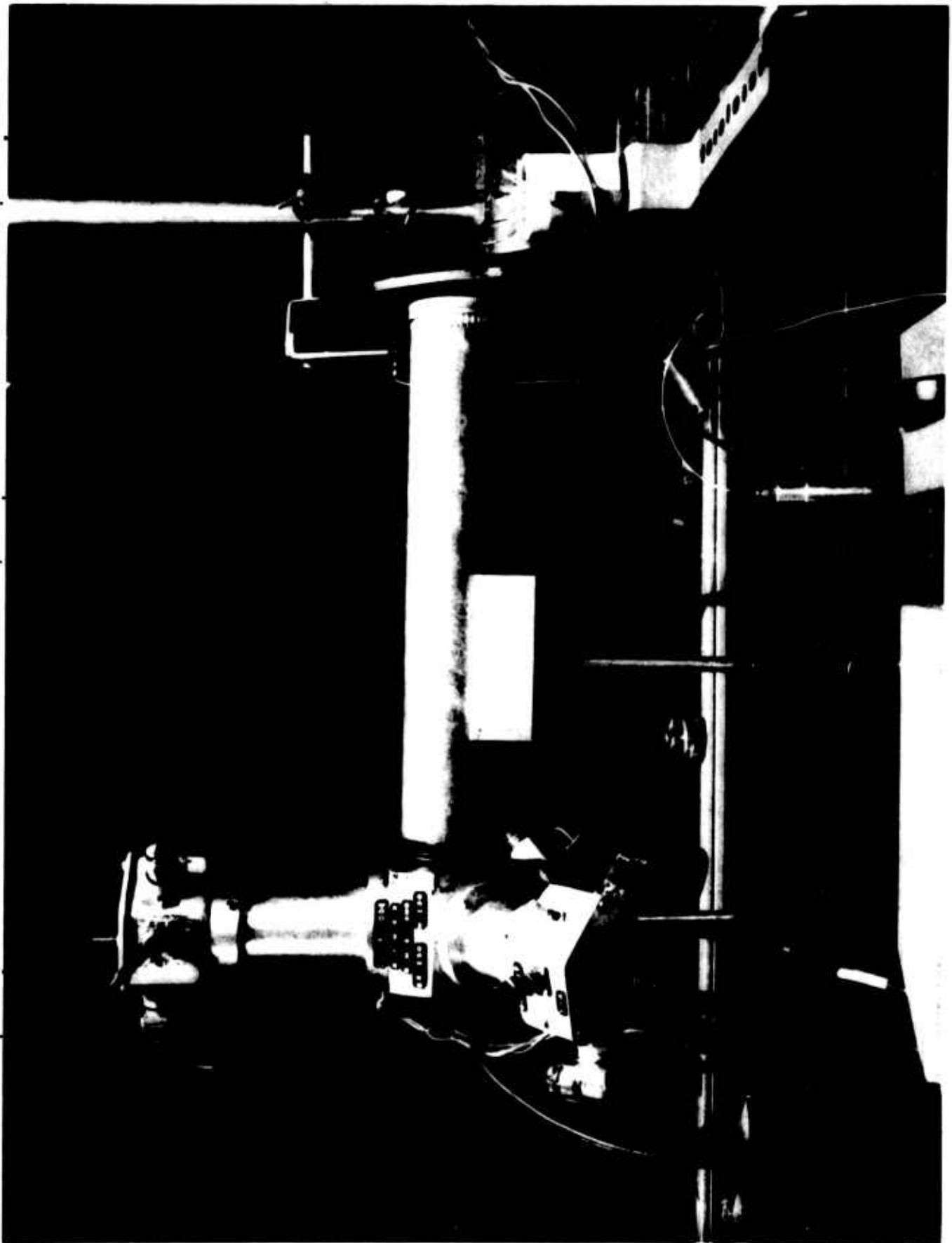


Figure M. A side view of the equipment diagramed in figure K.

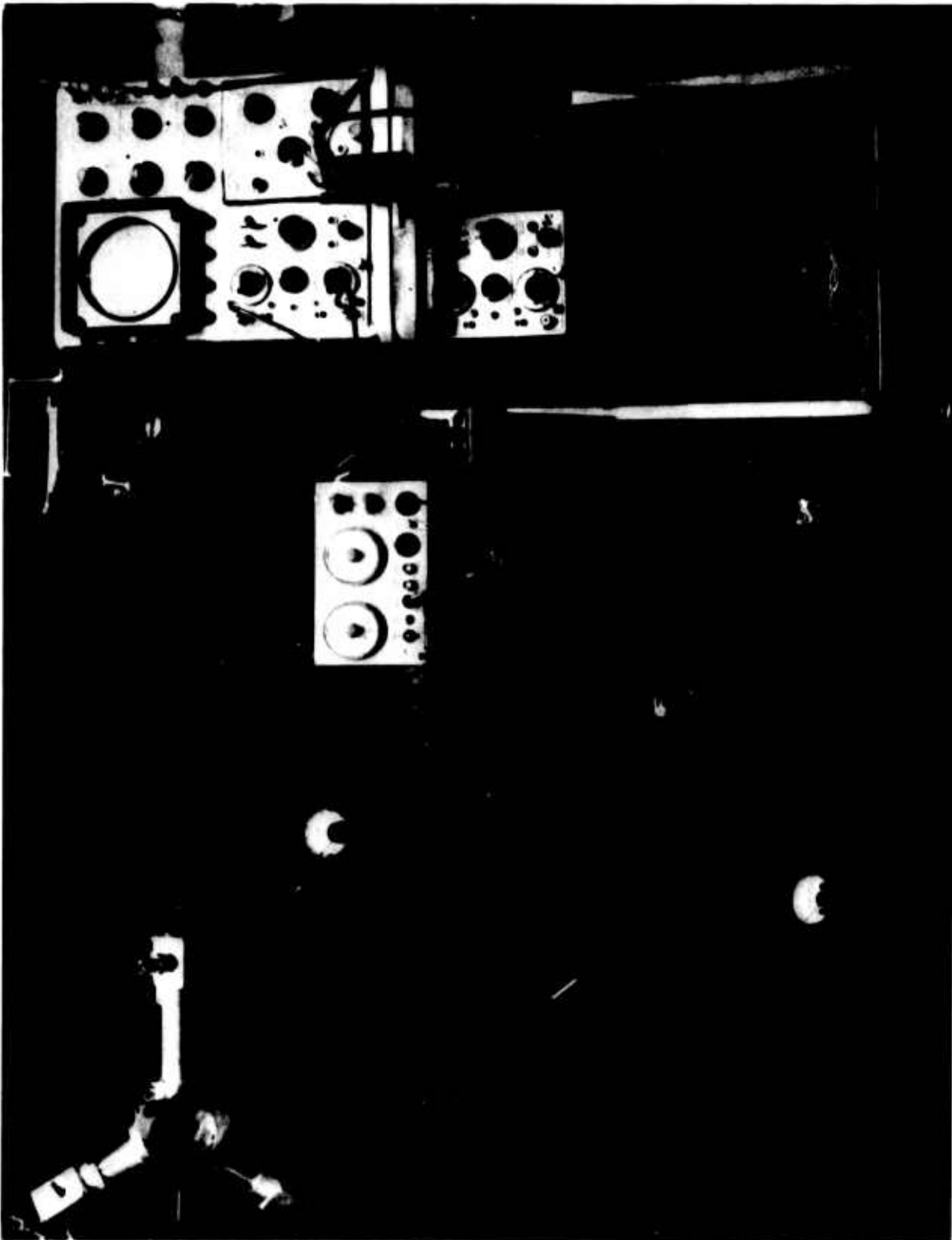
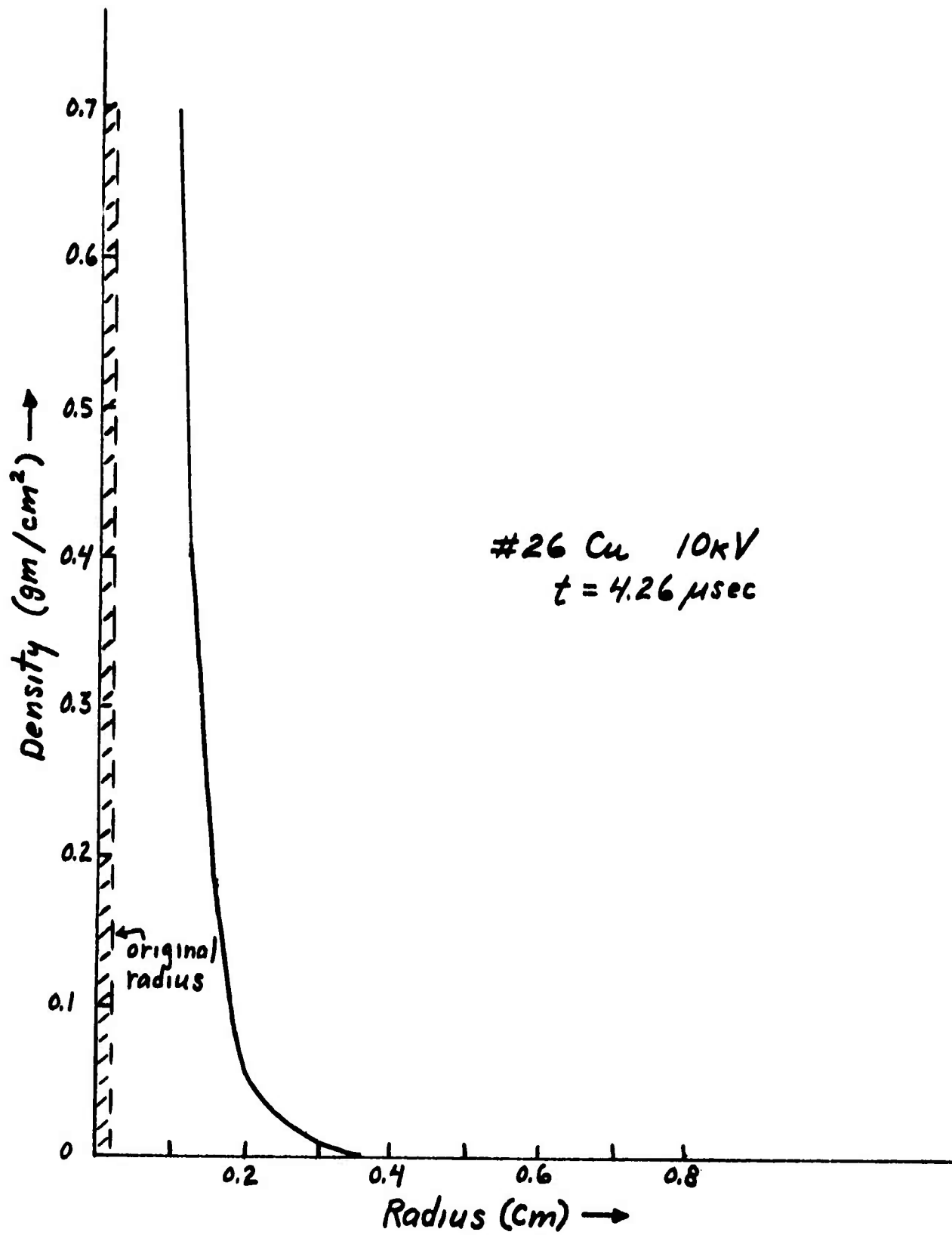


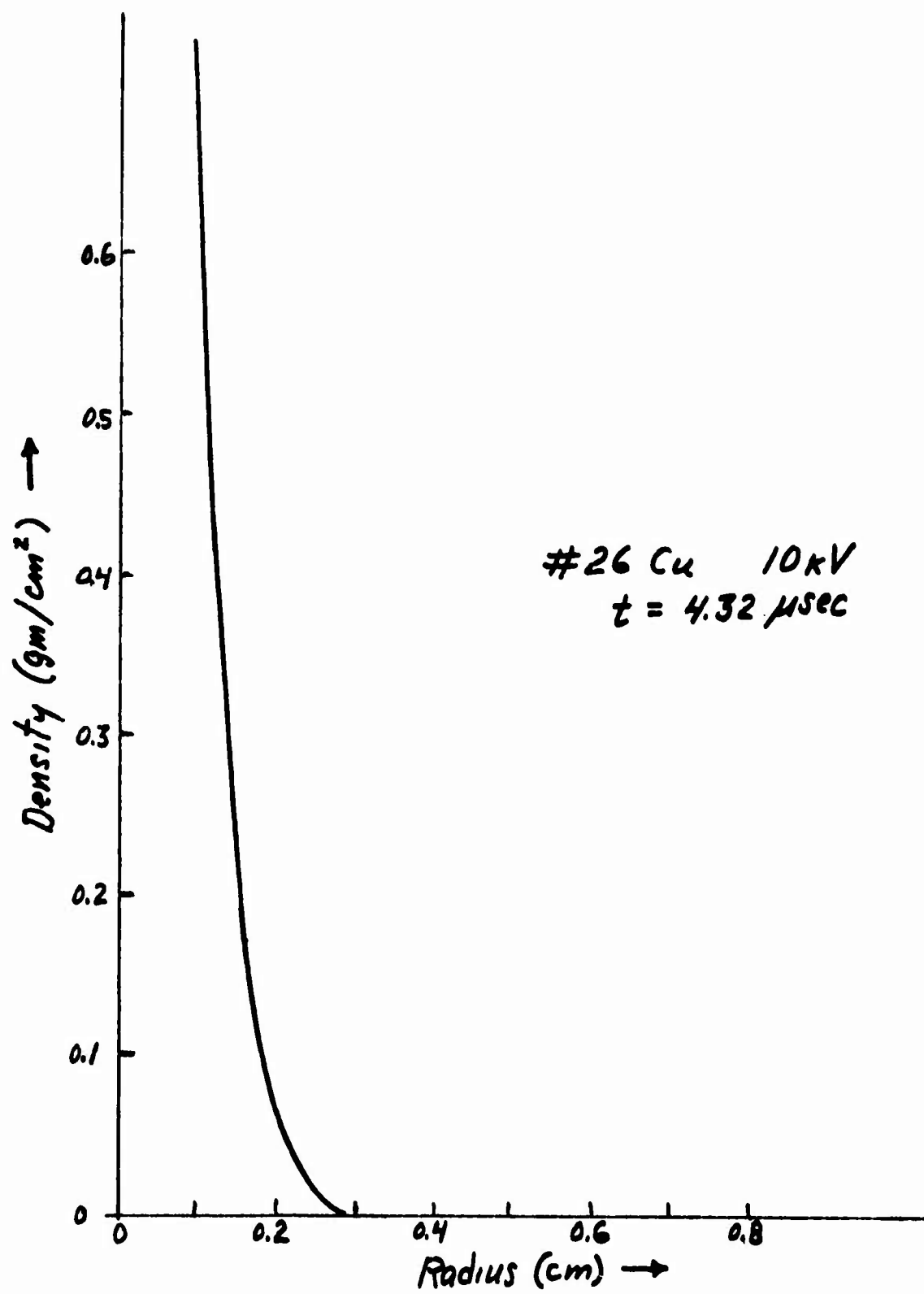
Figure N. From left to right, the optical pyrometer optical splitting unit, pyrometer chassis, gate generator, and recording oscilloscope. Units below comprise a small wire exploder used in initial tests.

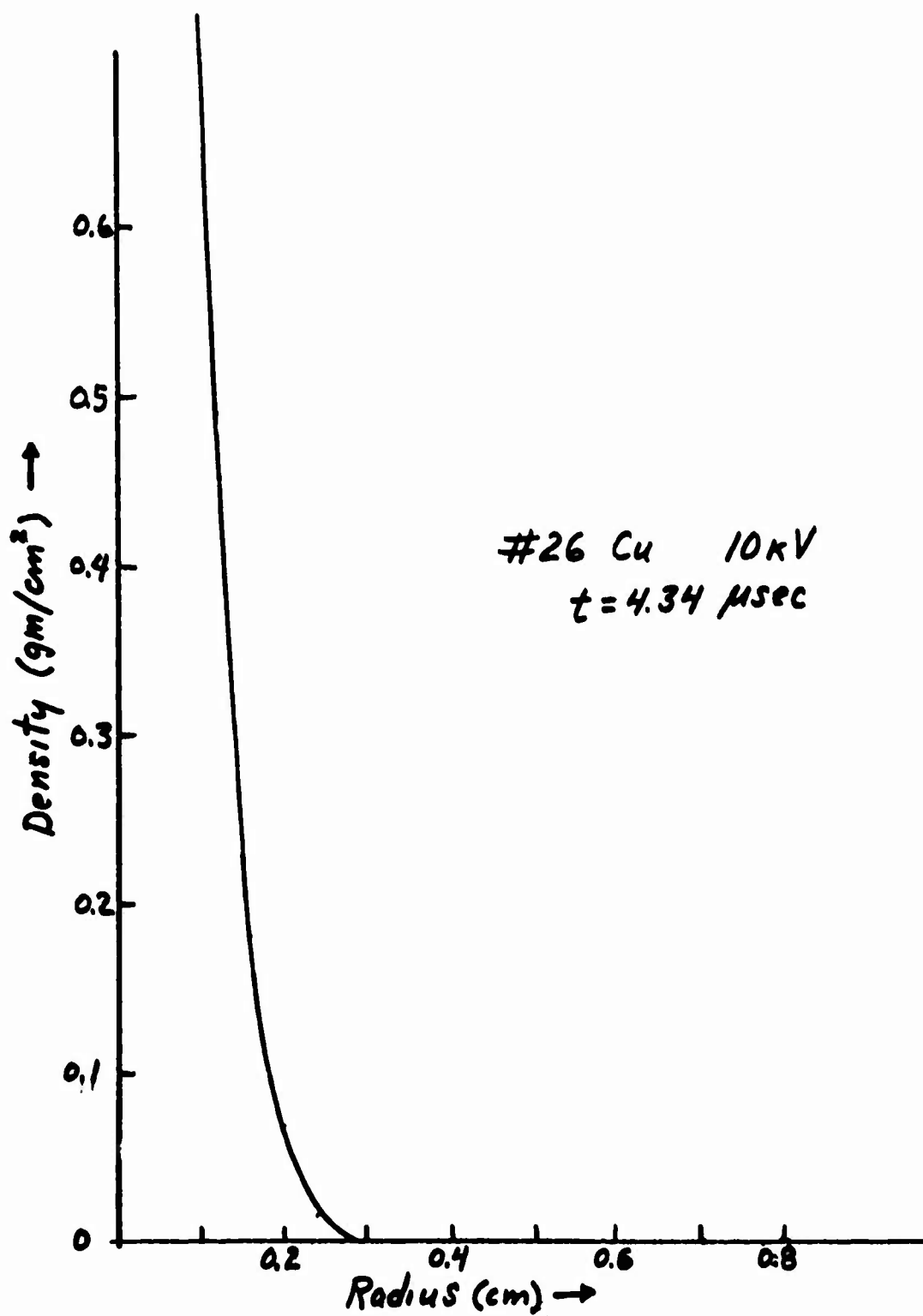
Page 81

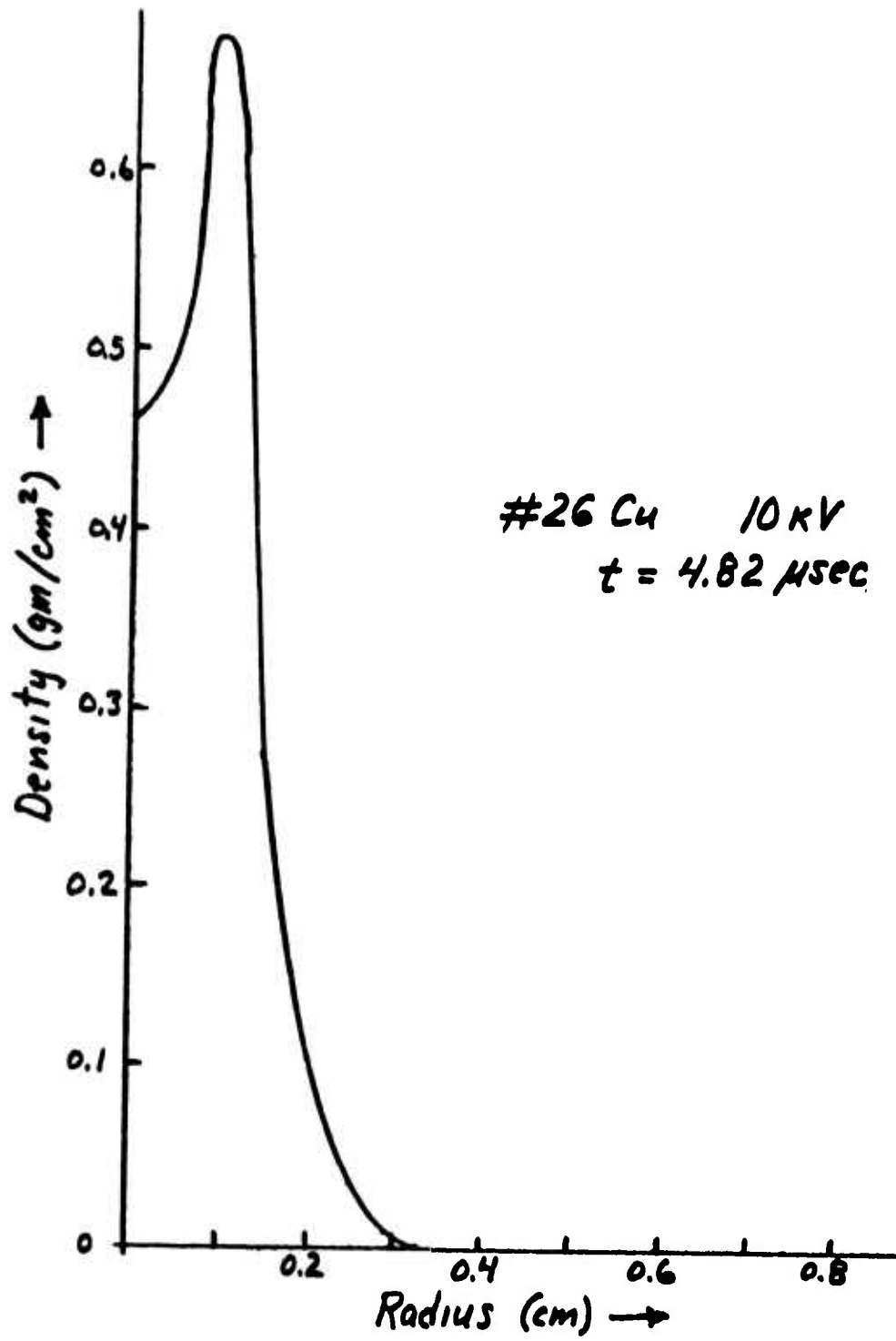
APPENDIX I

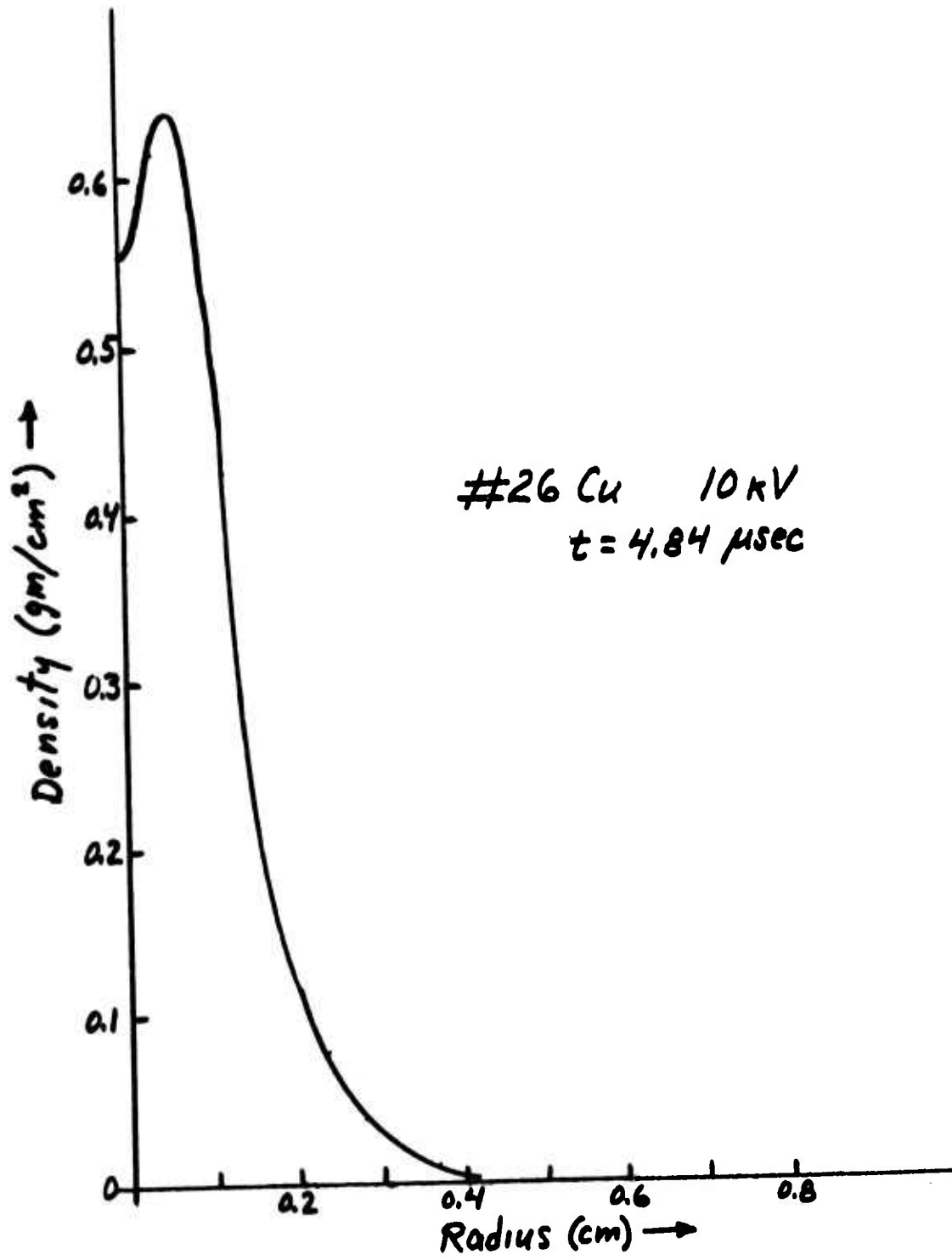
No. 26 Copper Wire 10kV Density Curves

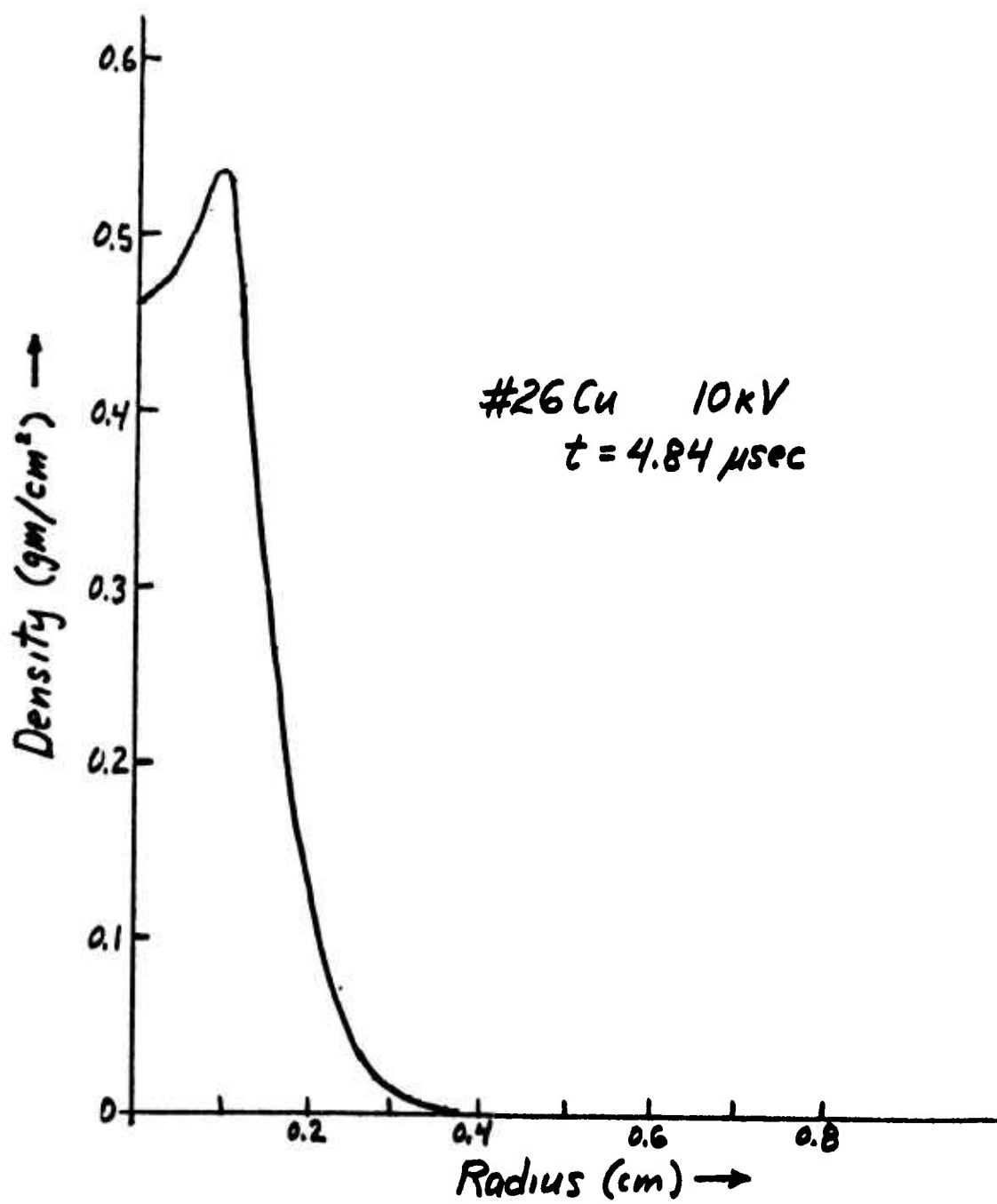


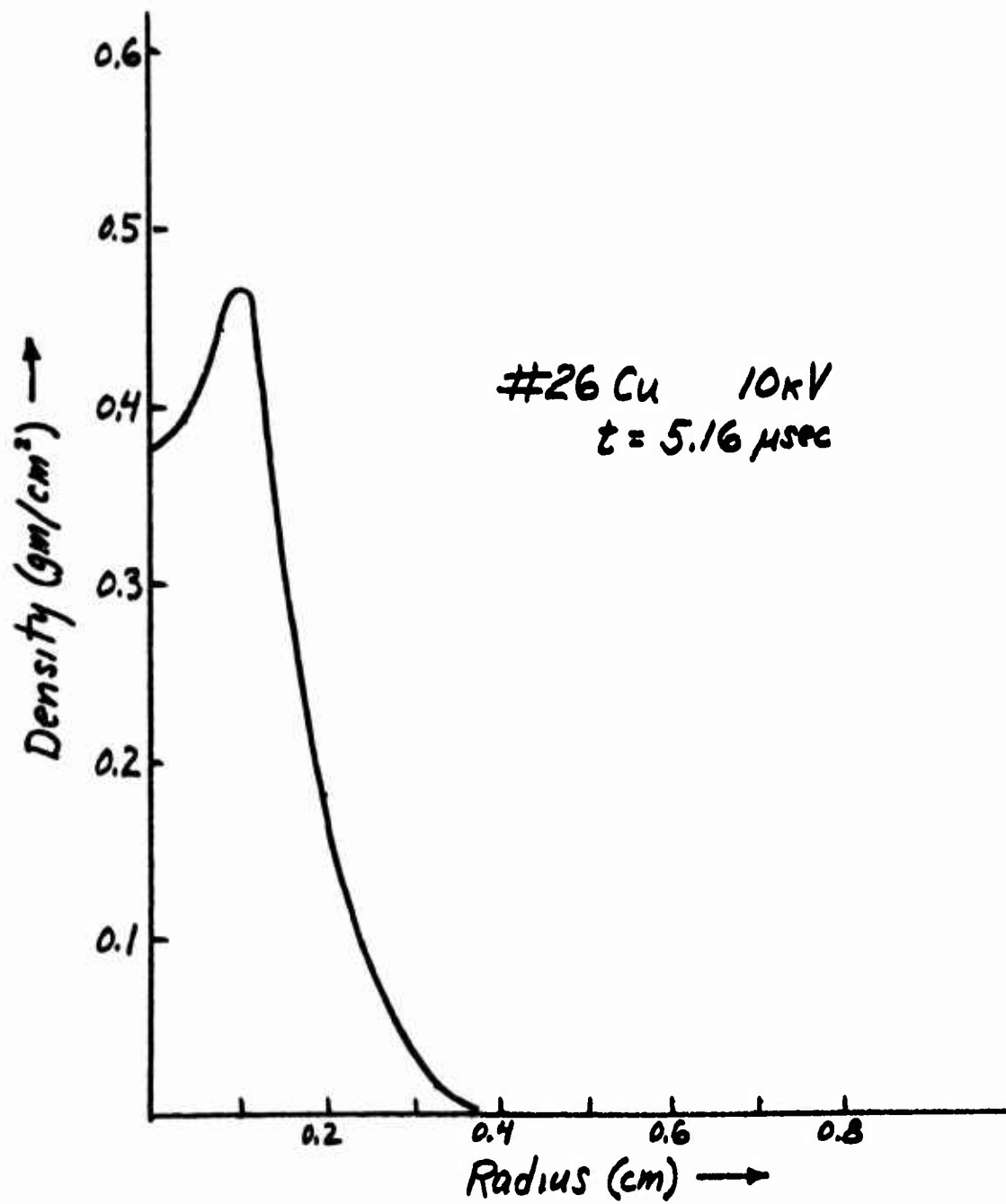


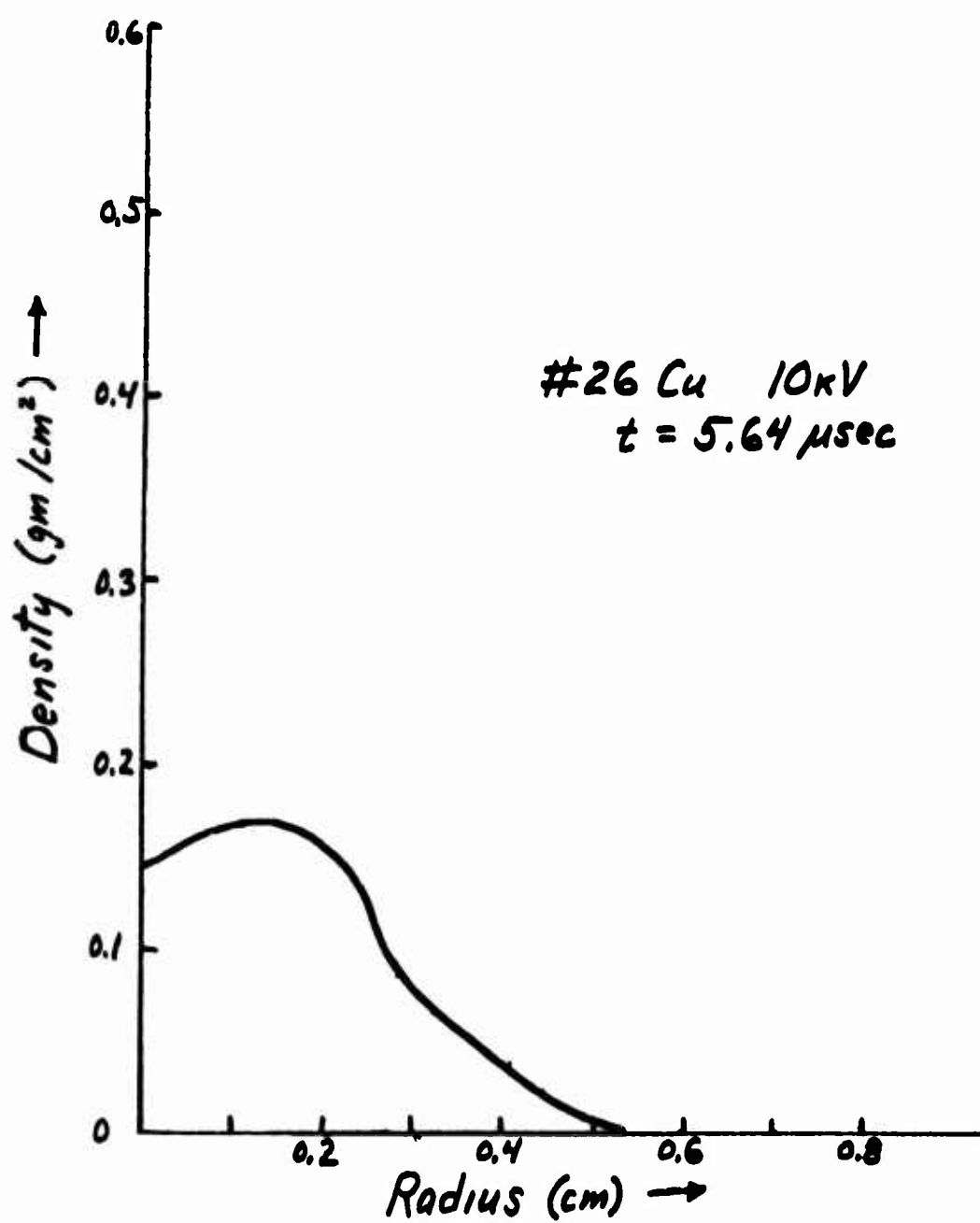


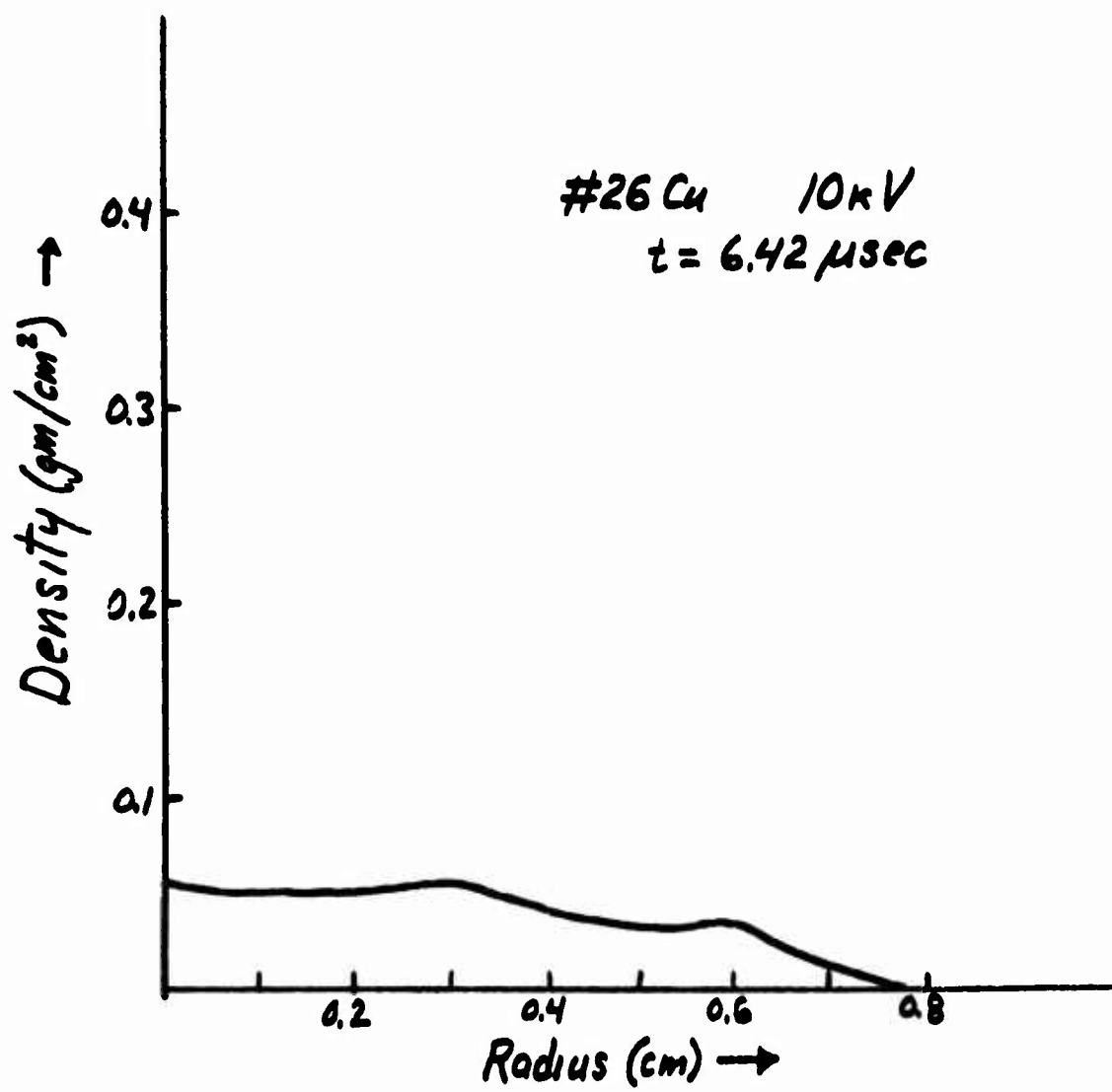








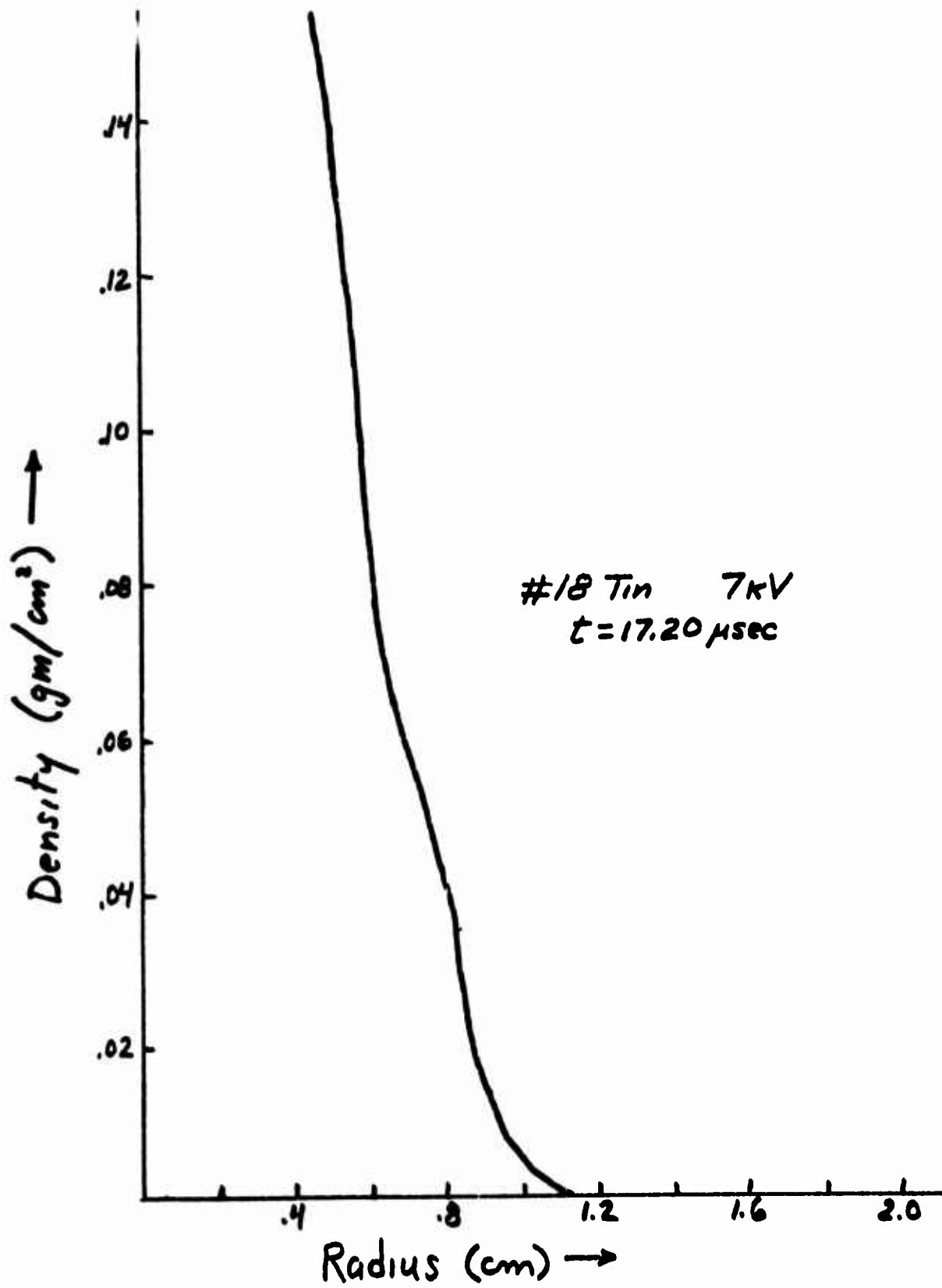


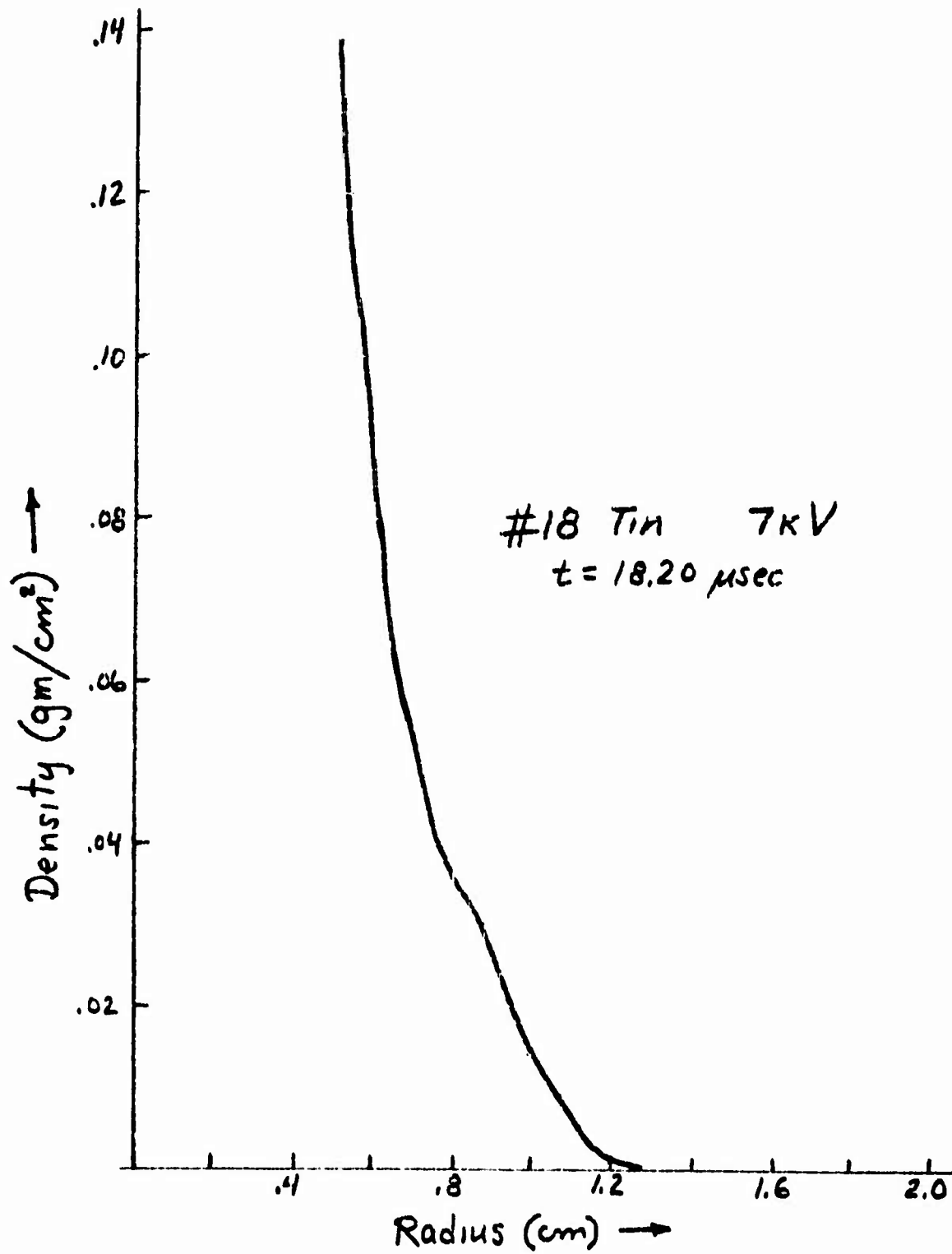


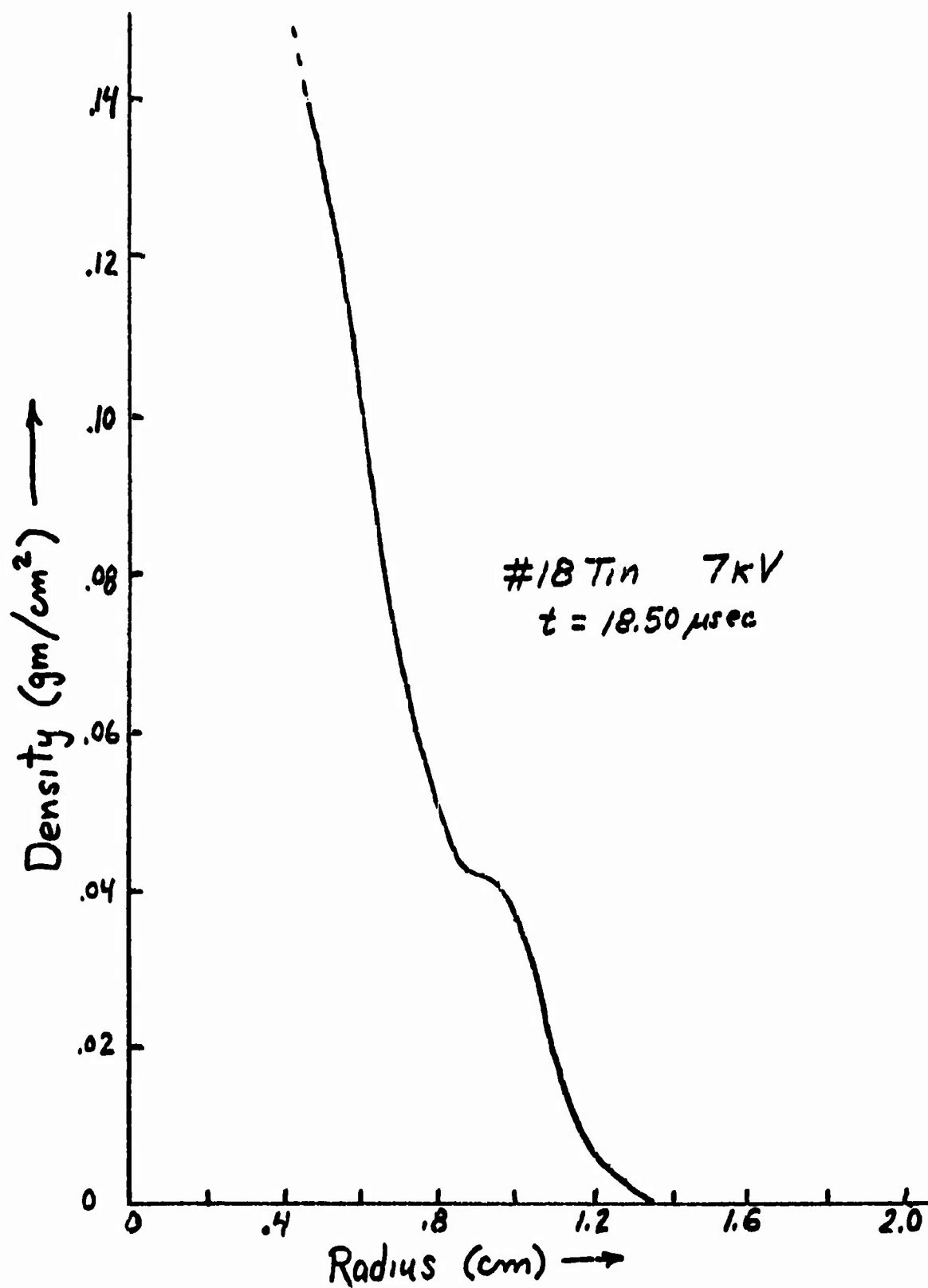
Page 91

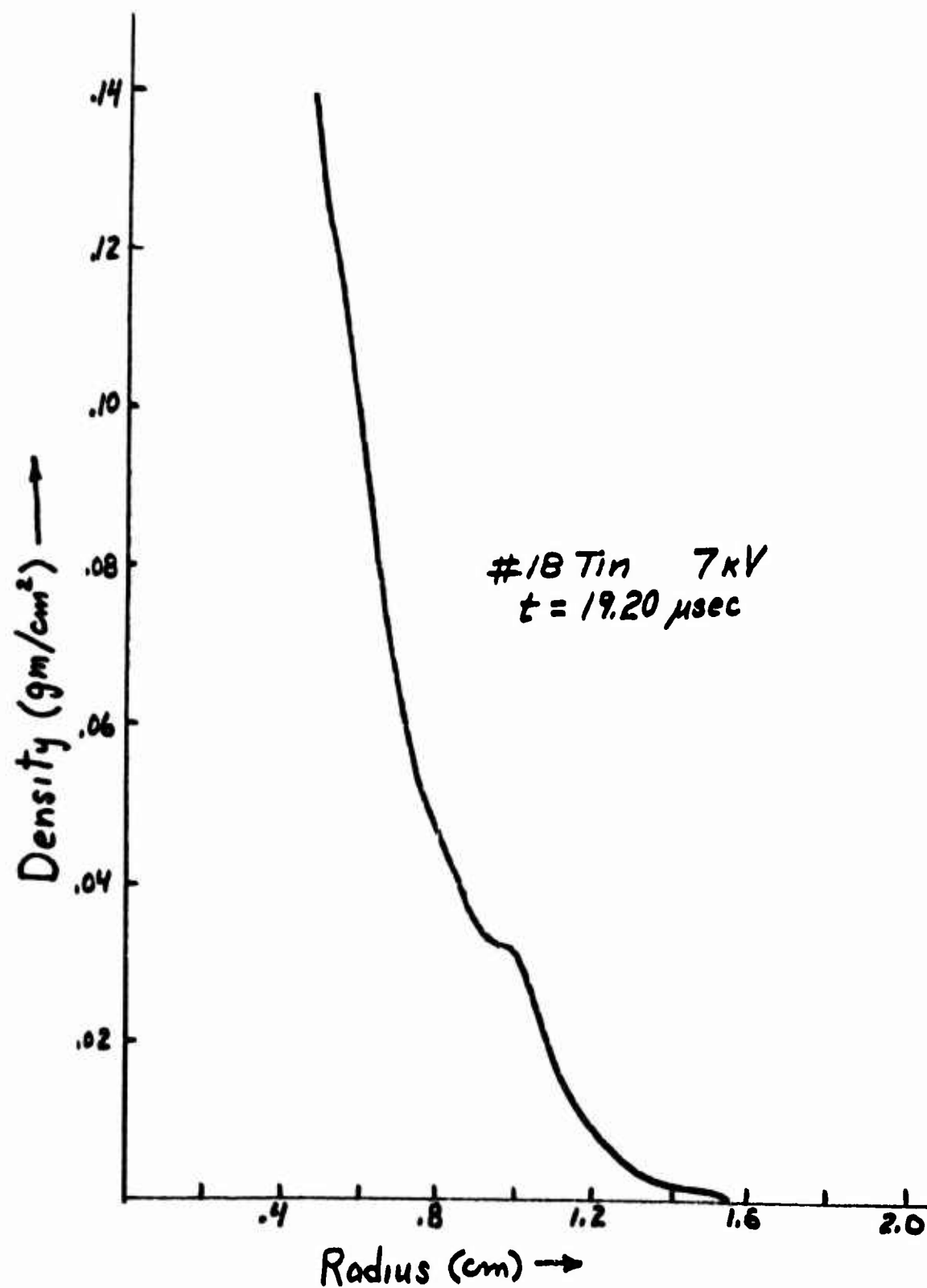
APPENDIX II

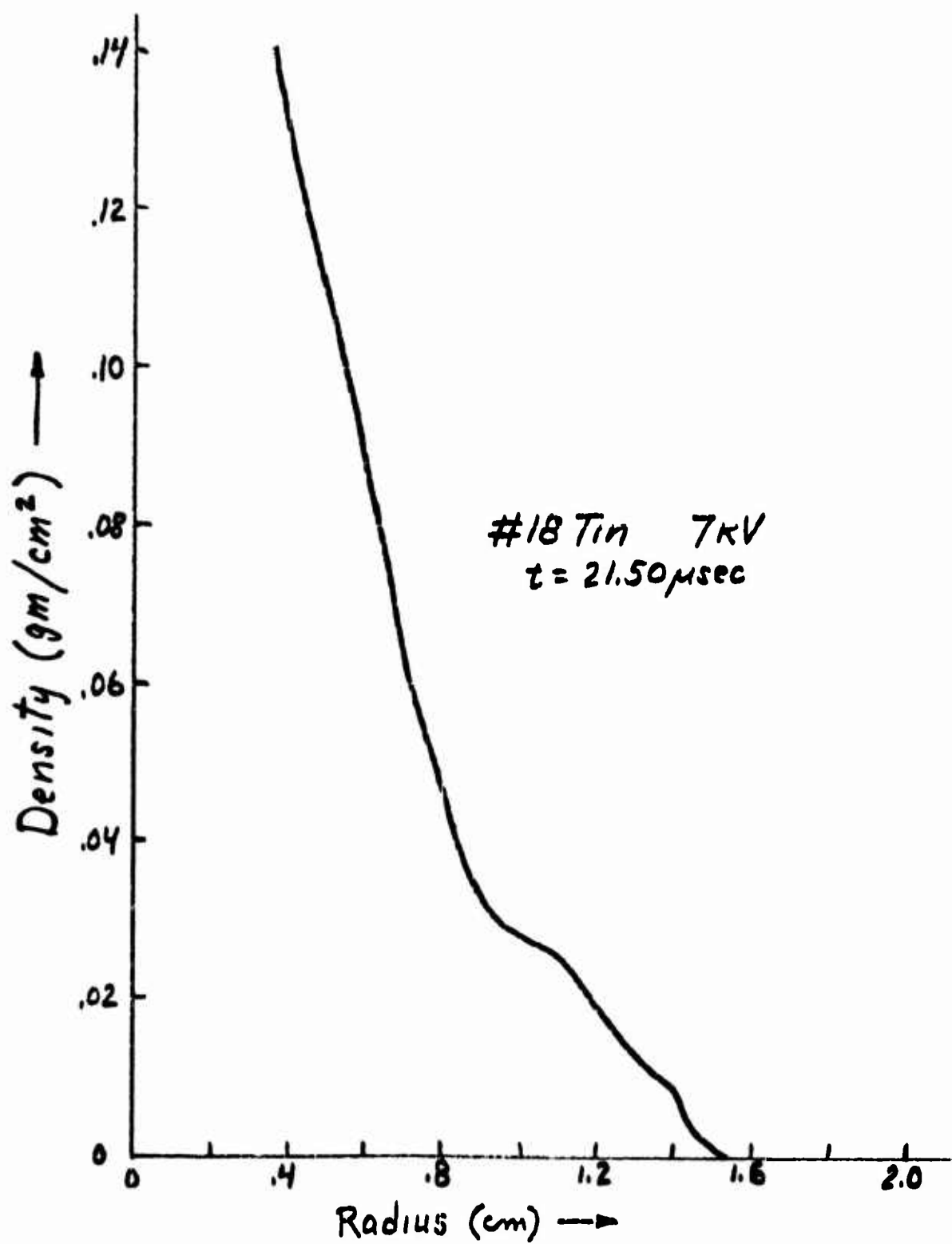
No. 18 Tin Wire 7kV Density Curves

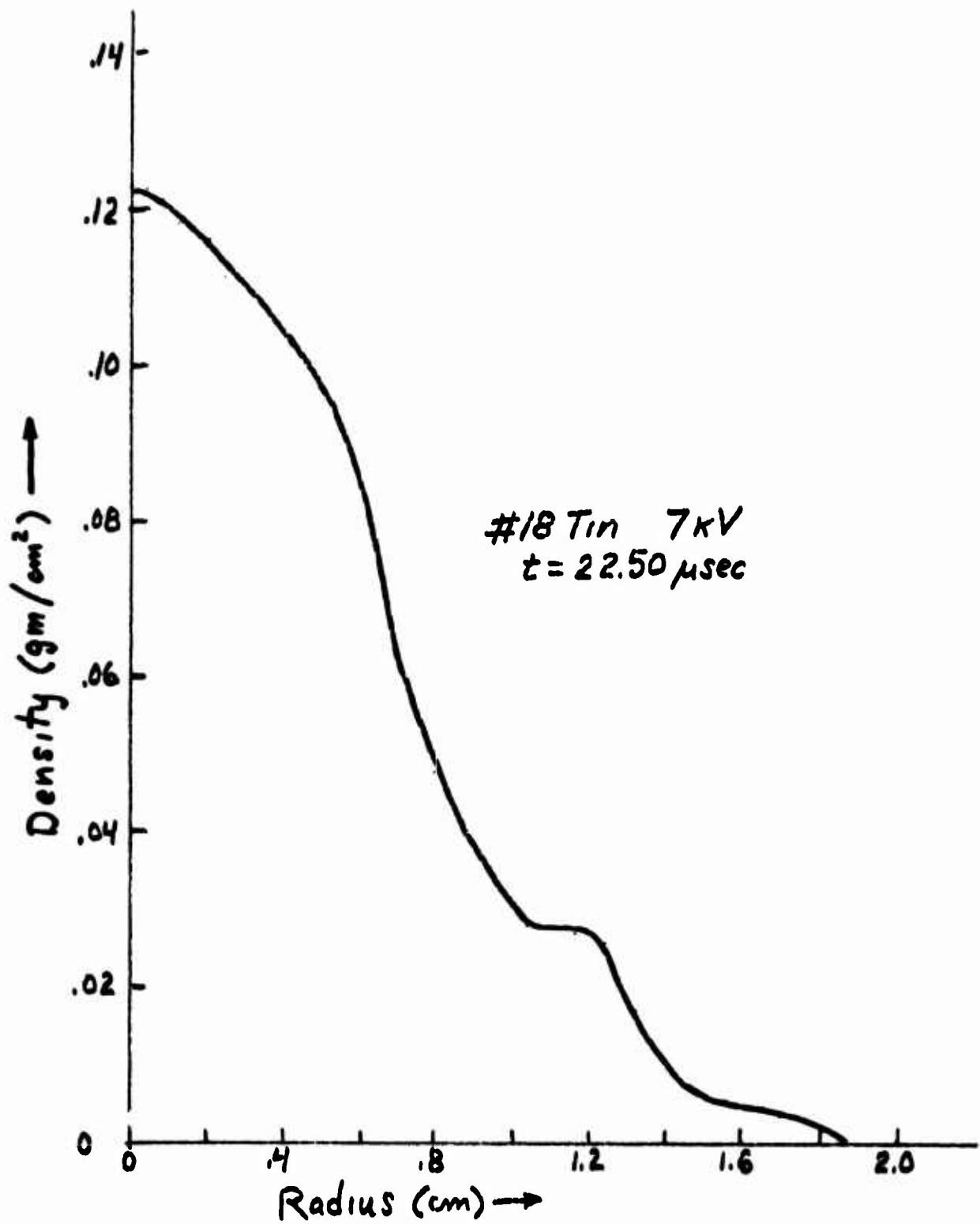


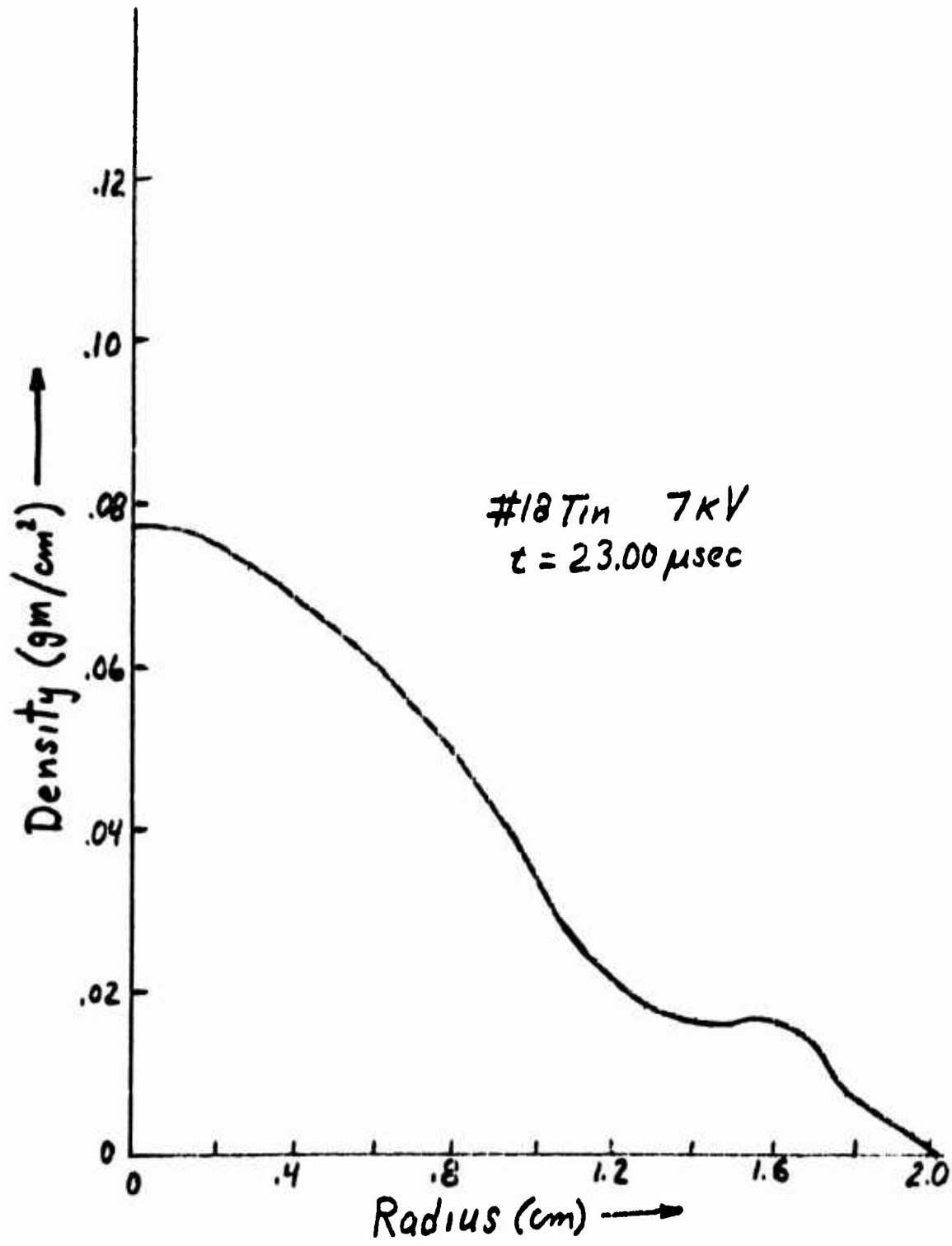


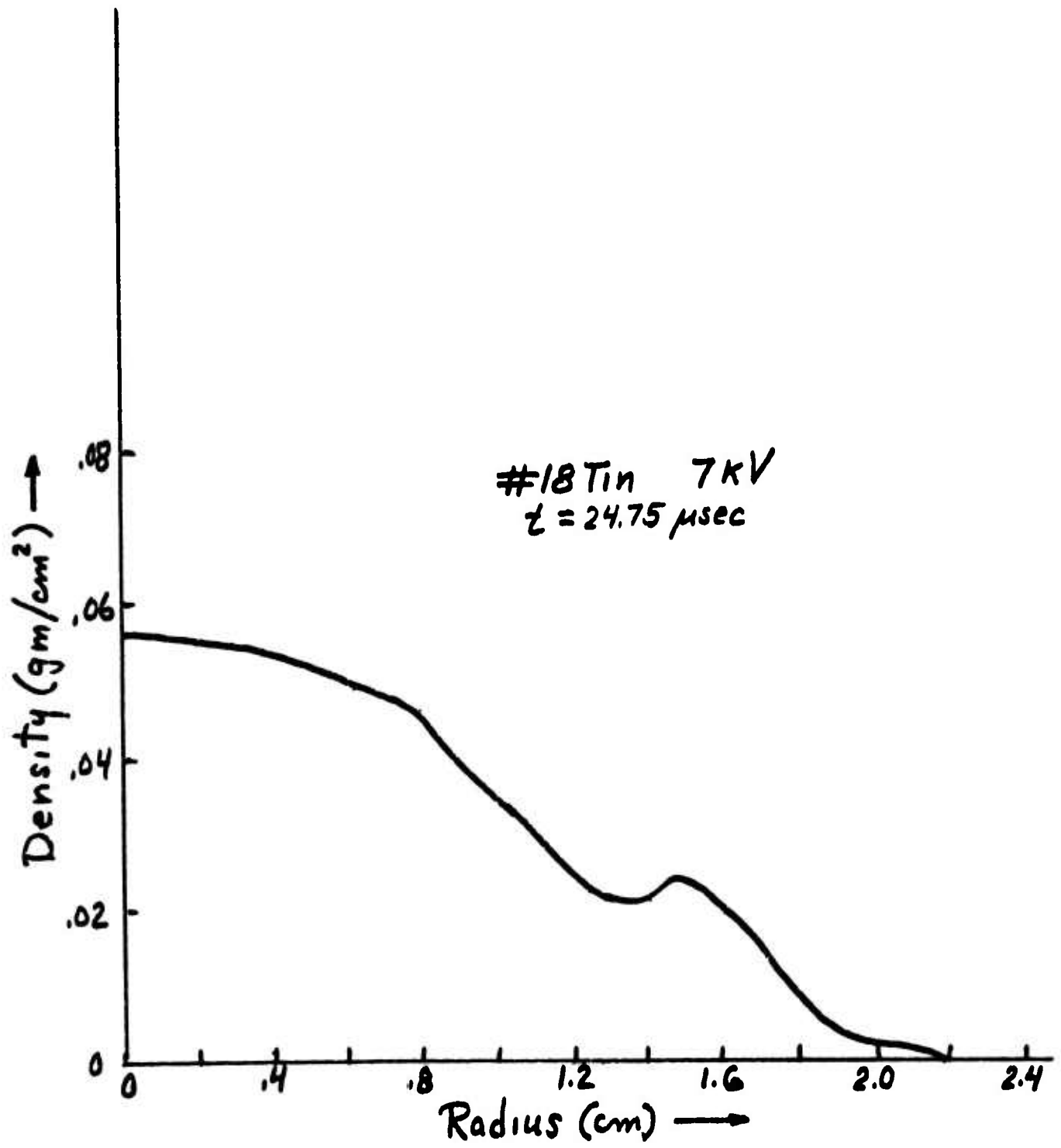


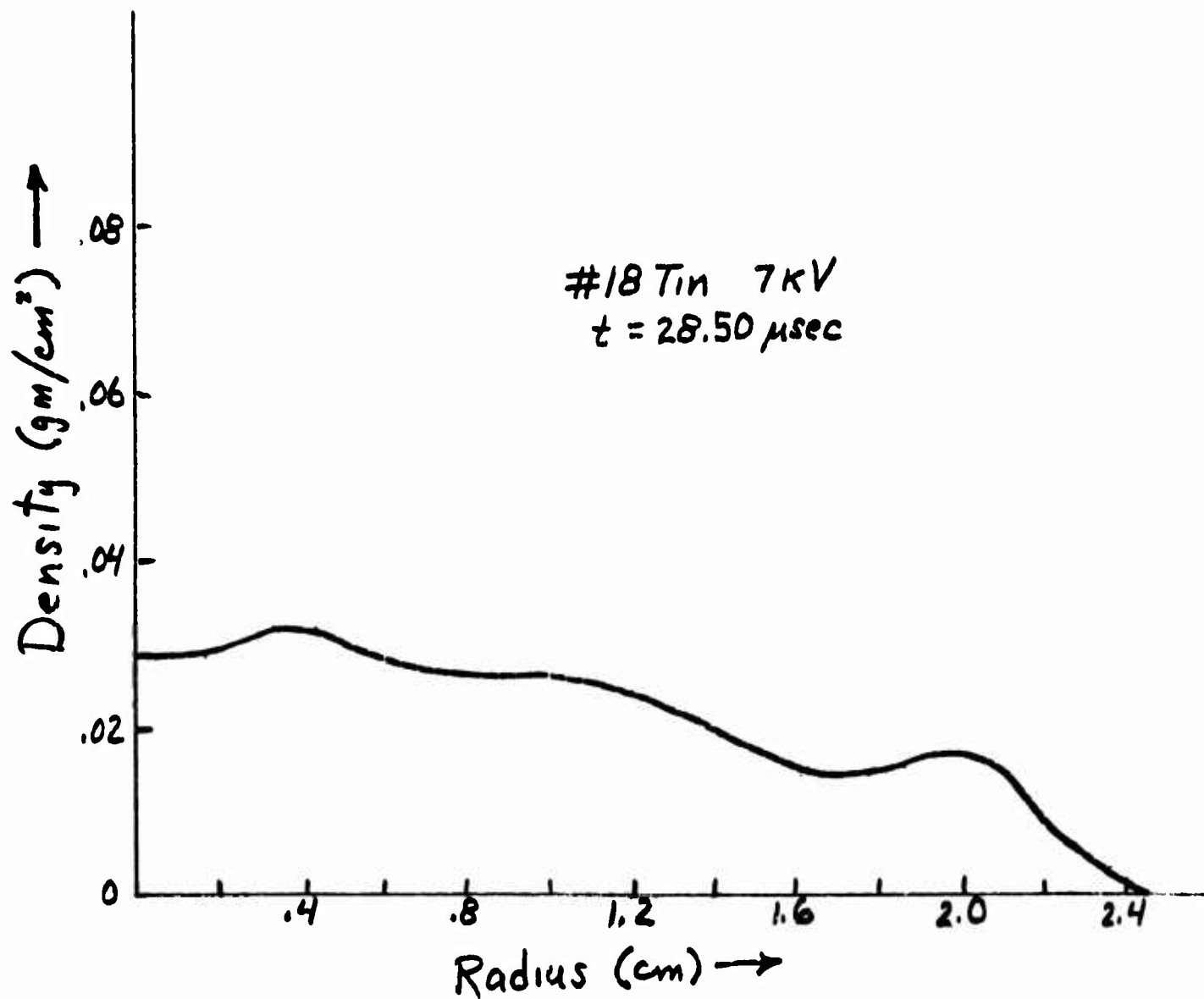


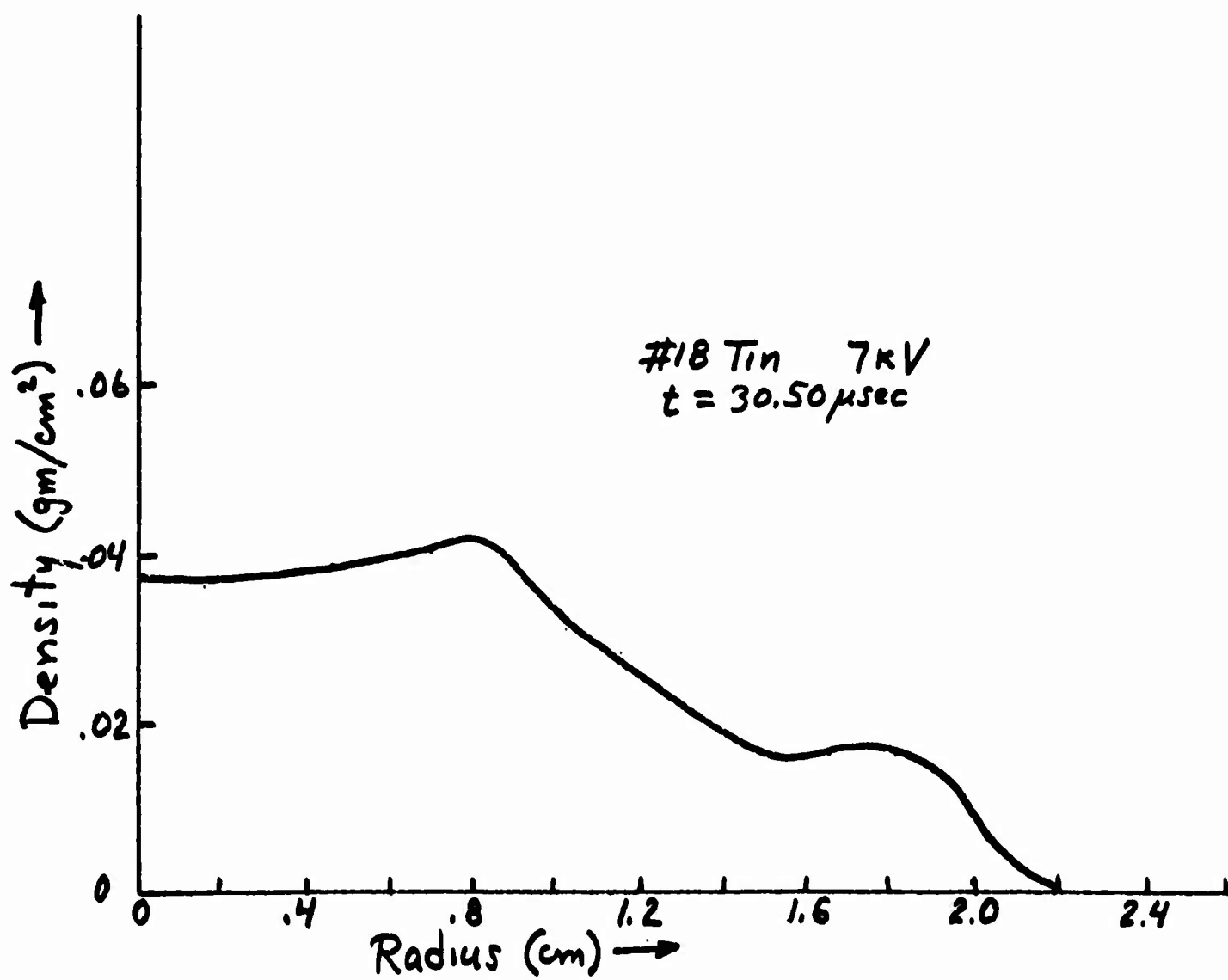


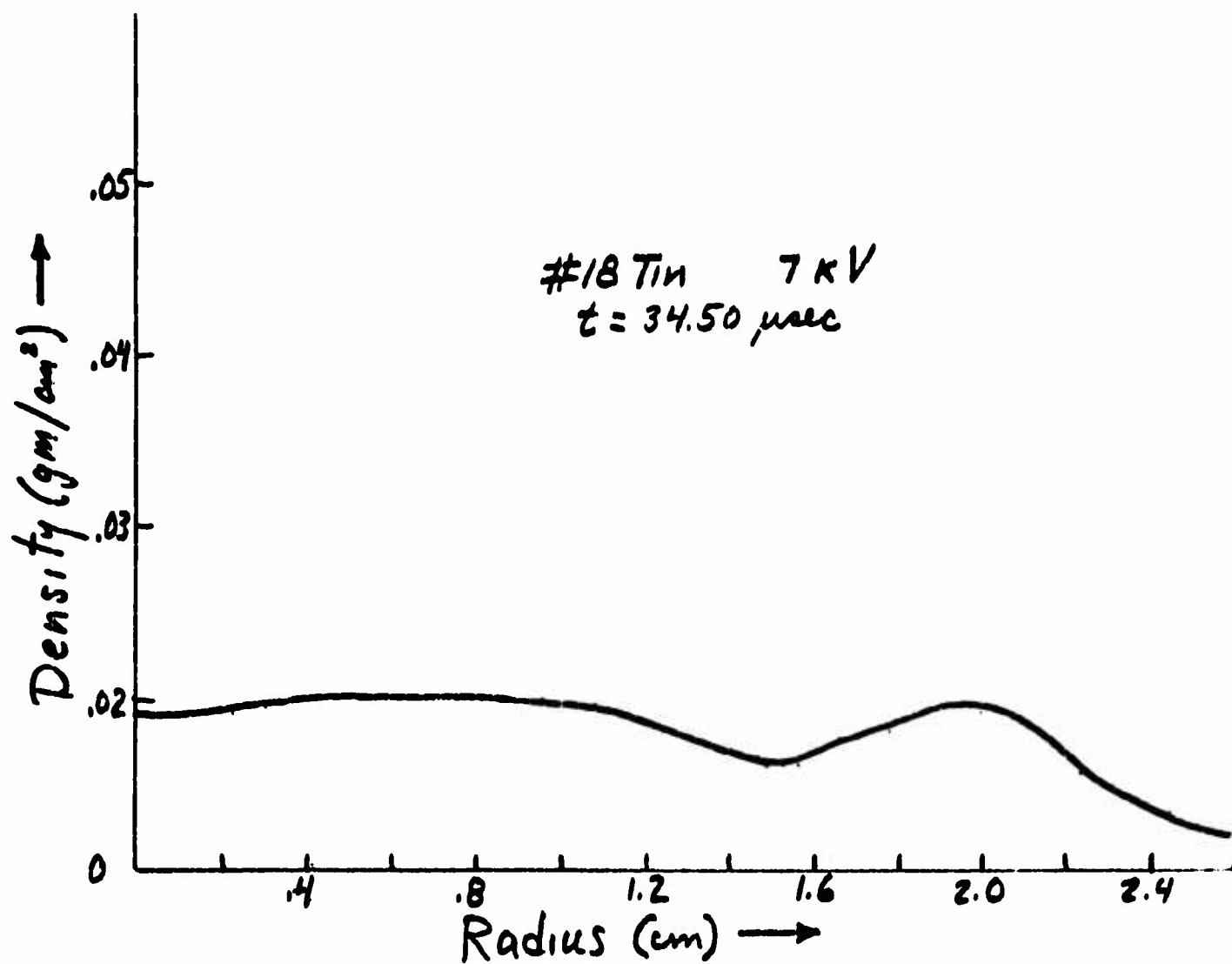








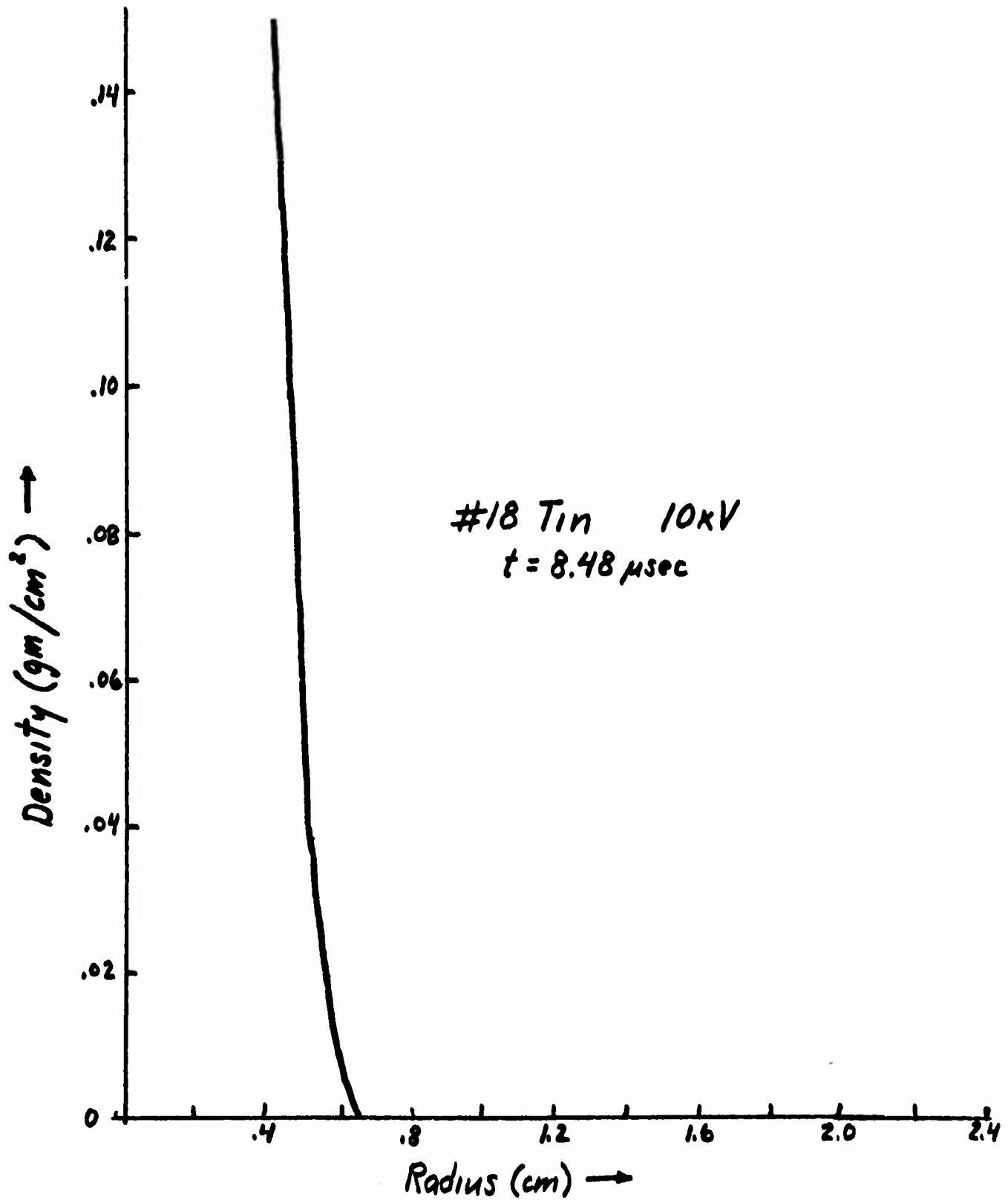


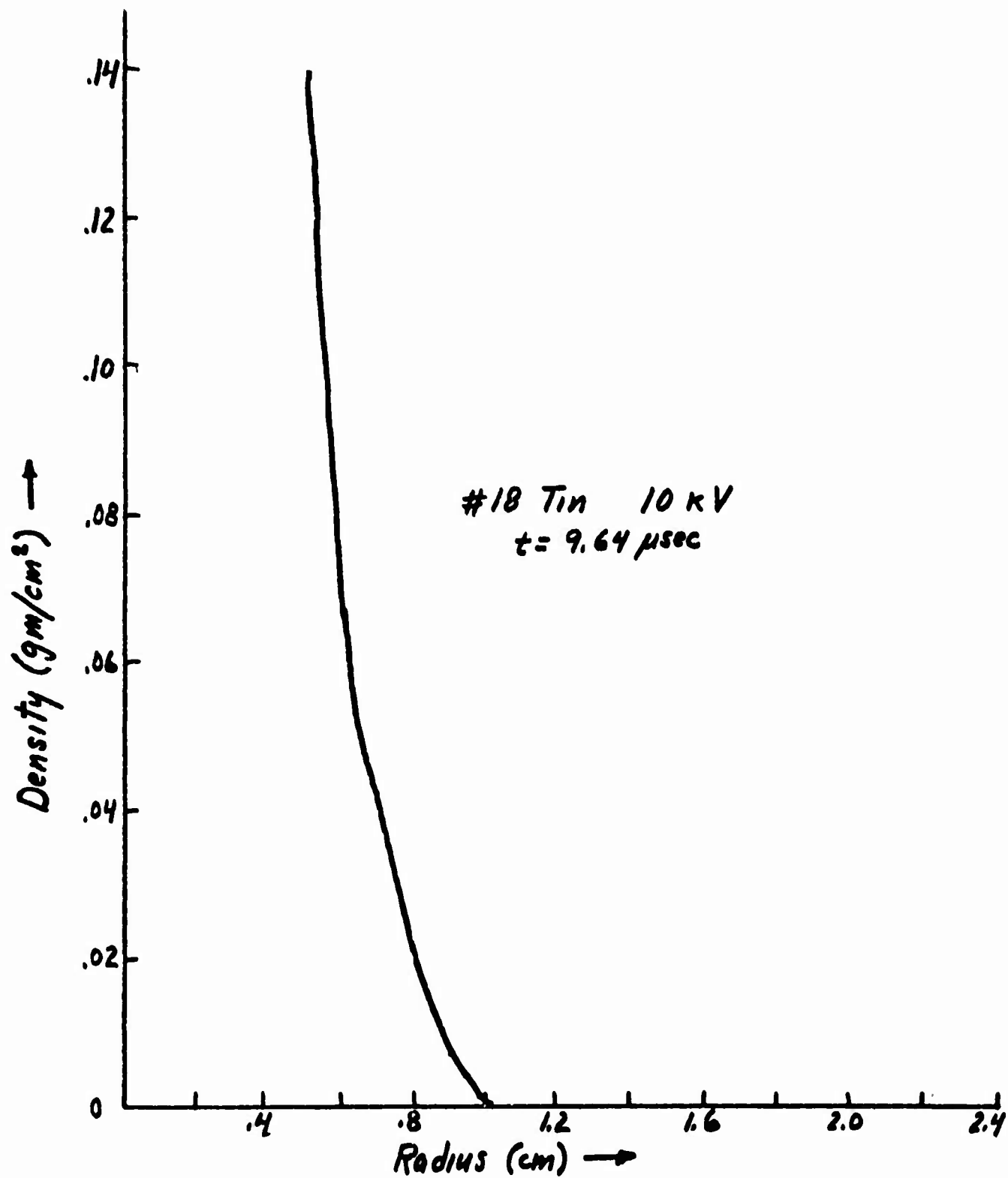


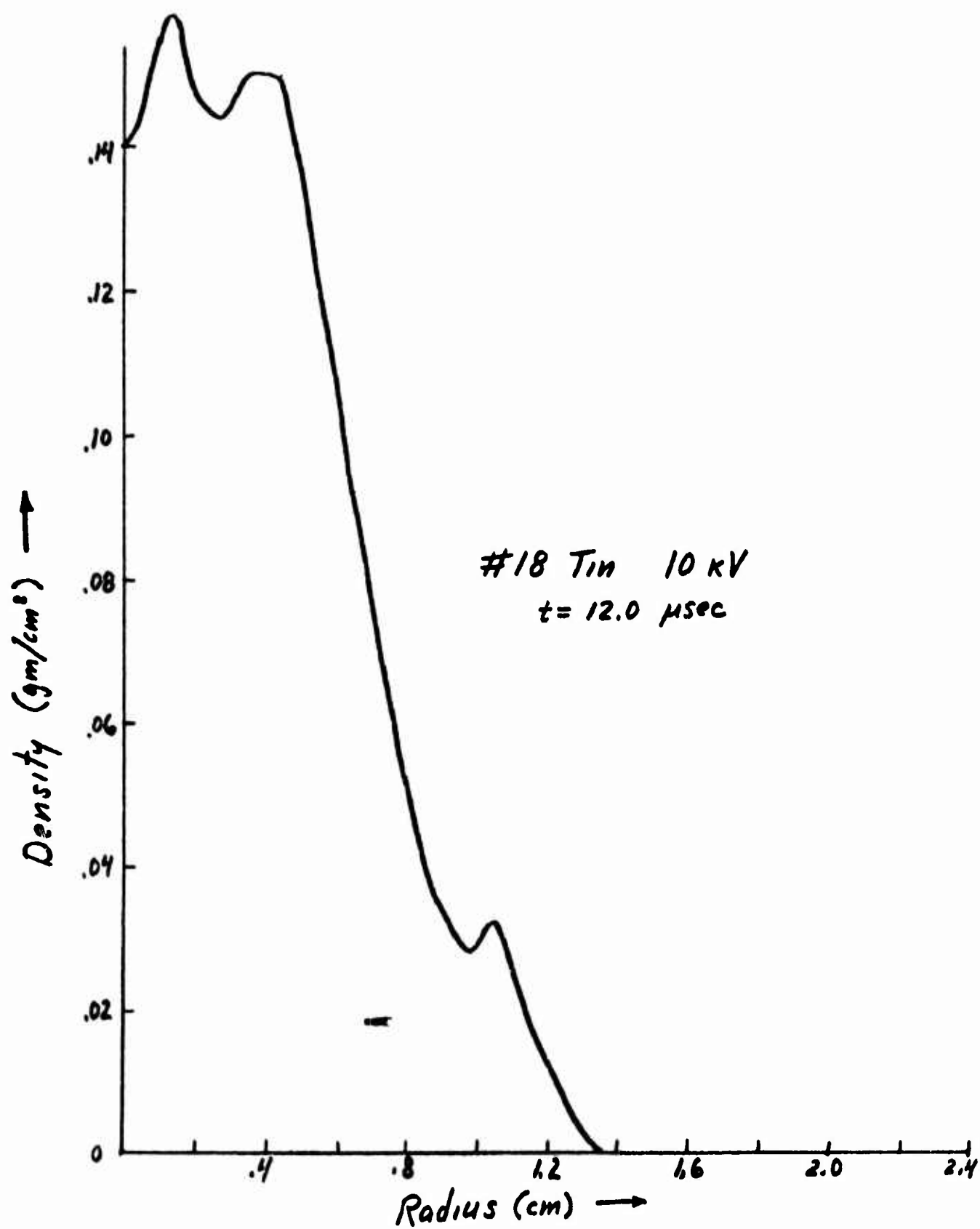
Page 103

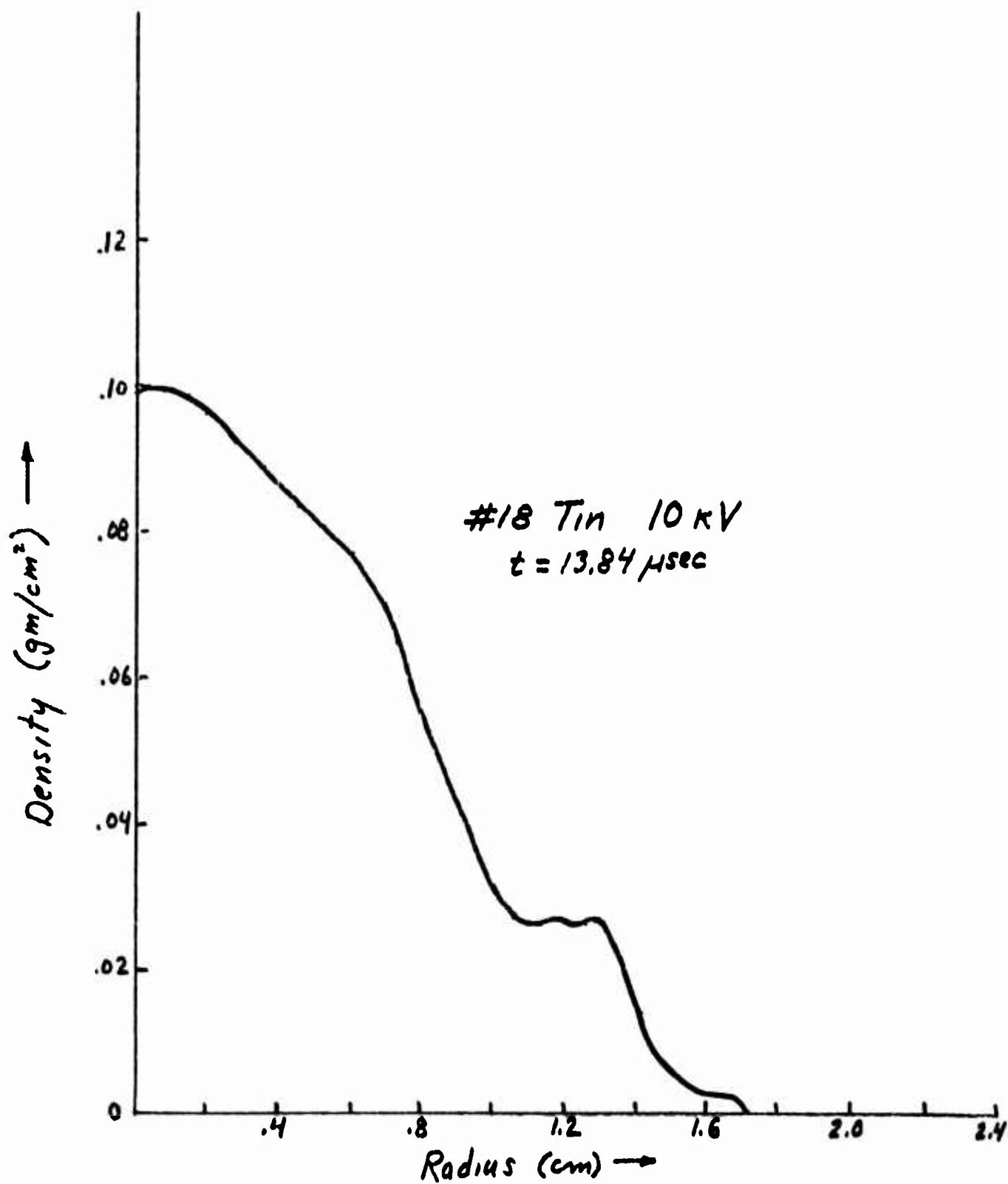
APPENDIX III

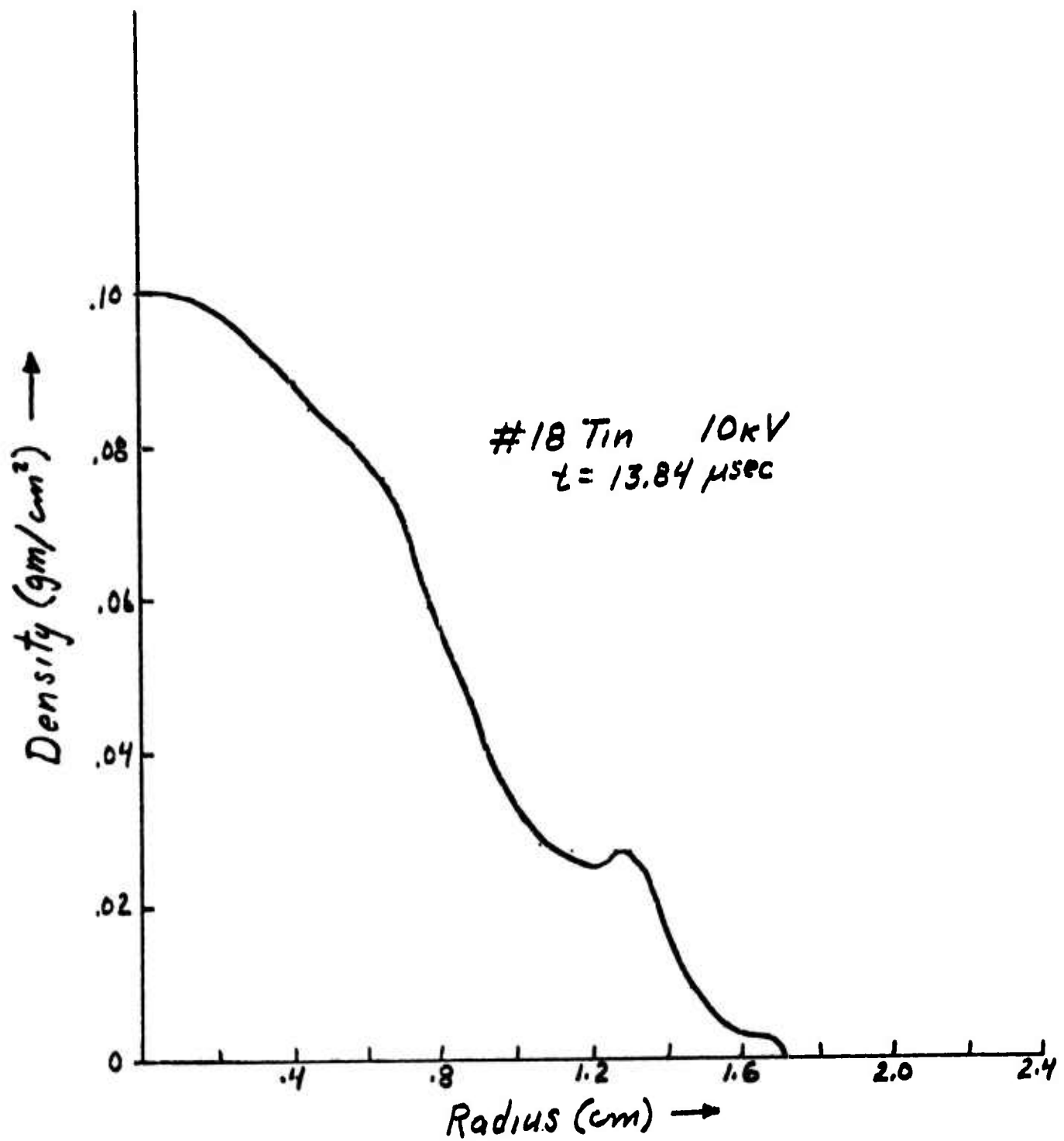
No. 18 Tin Wire 10kV Density Curves

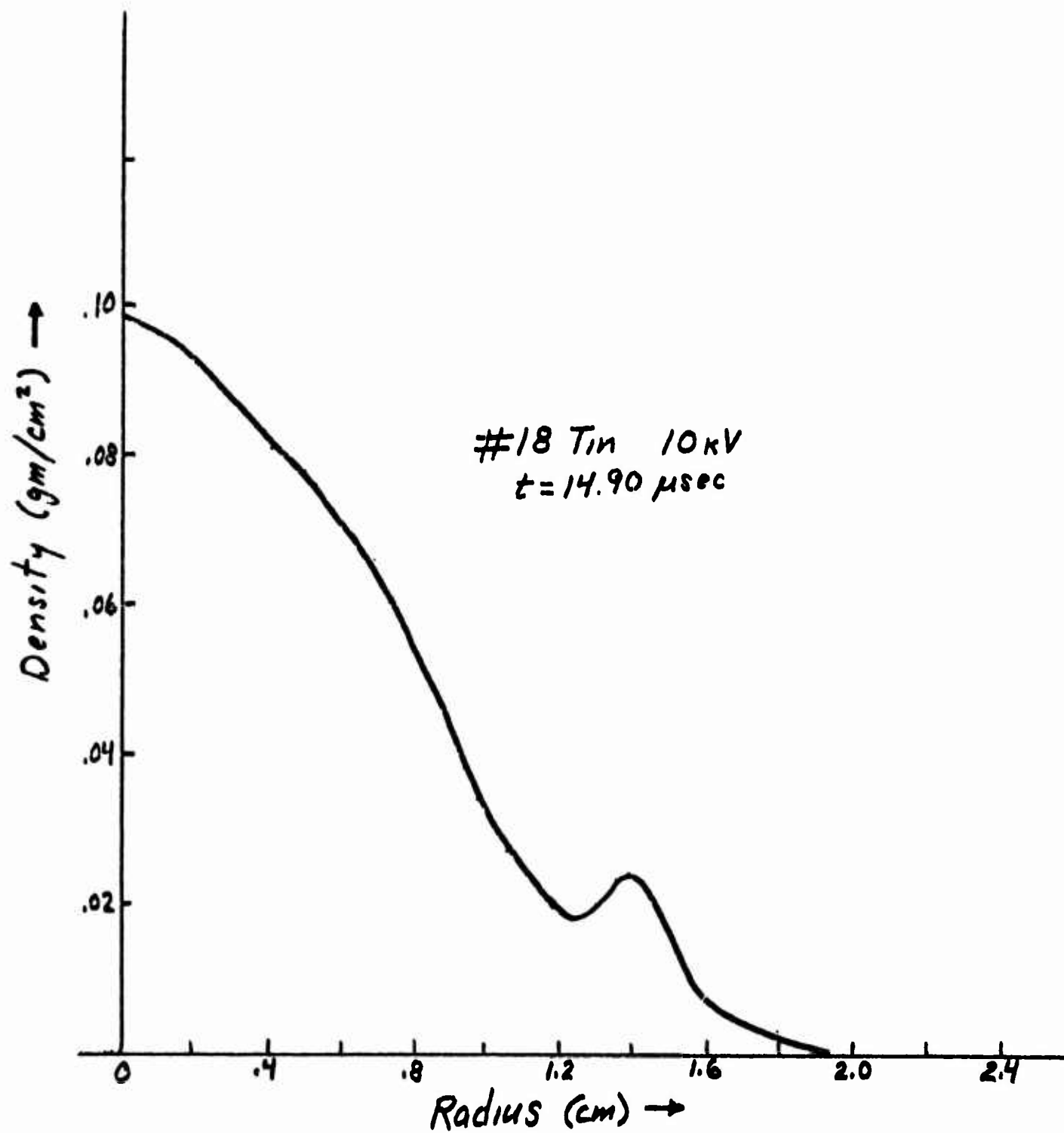


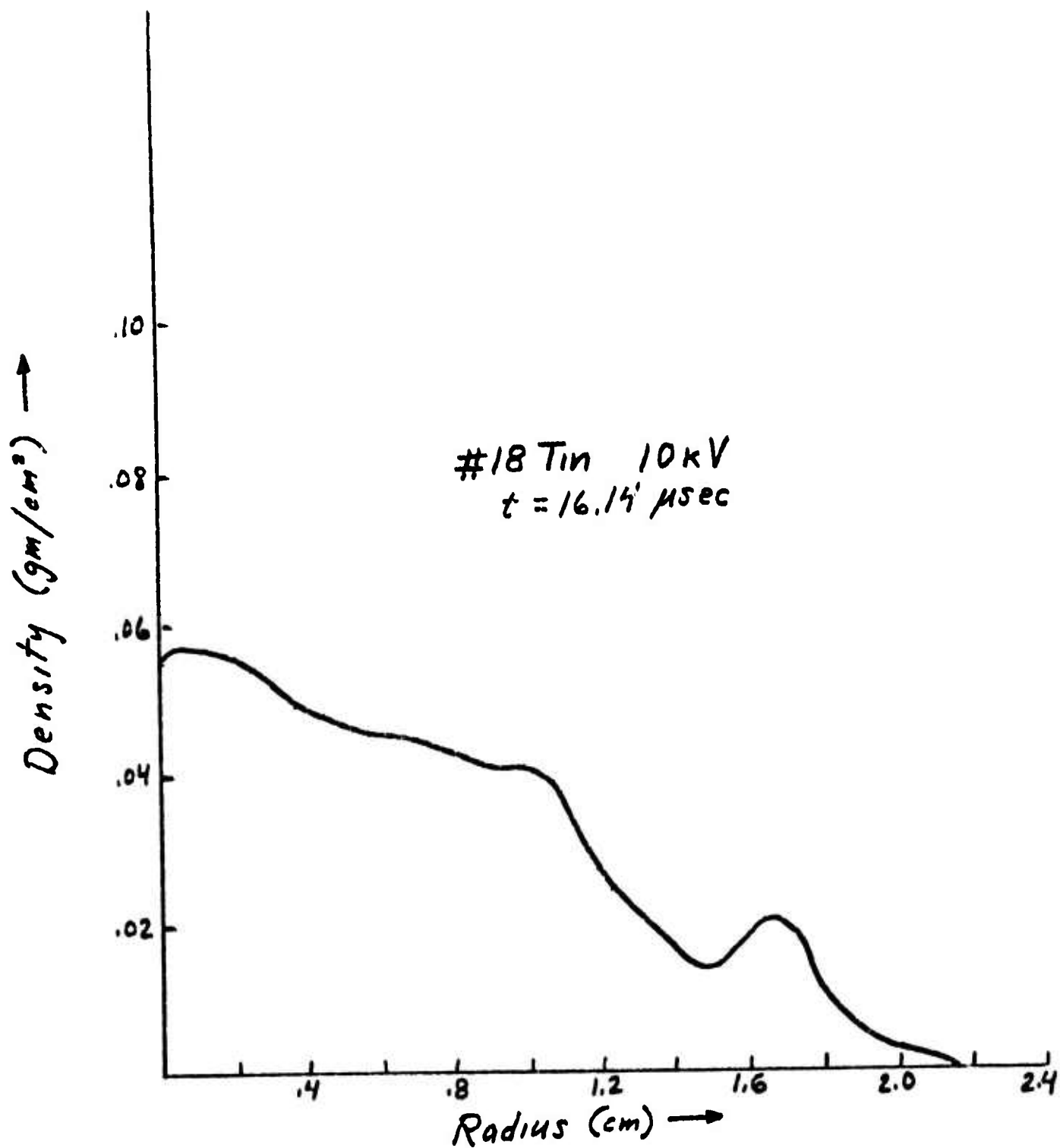


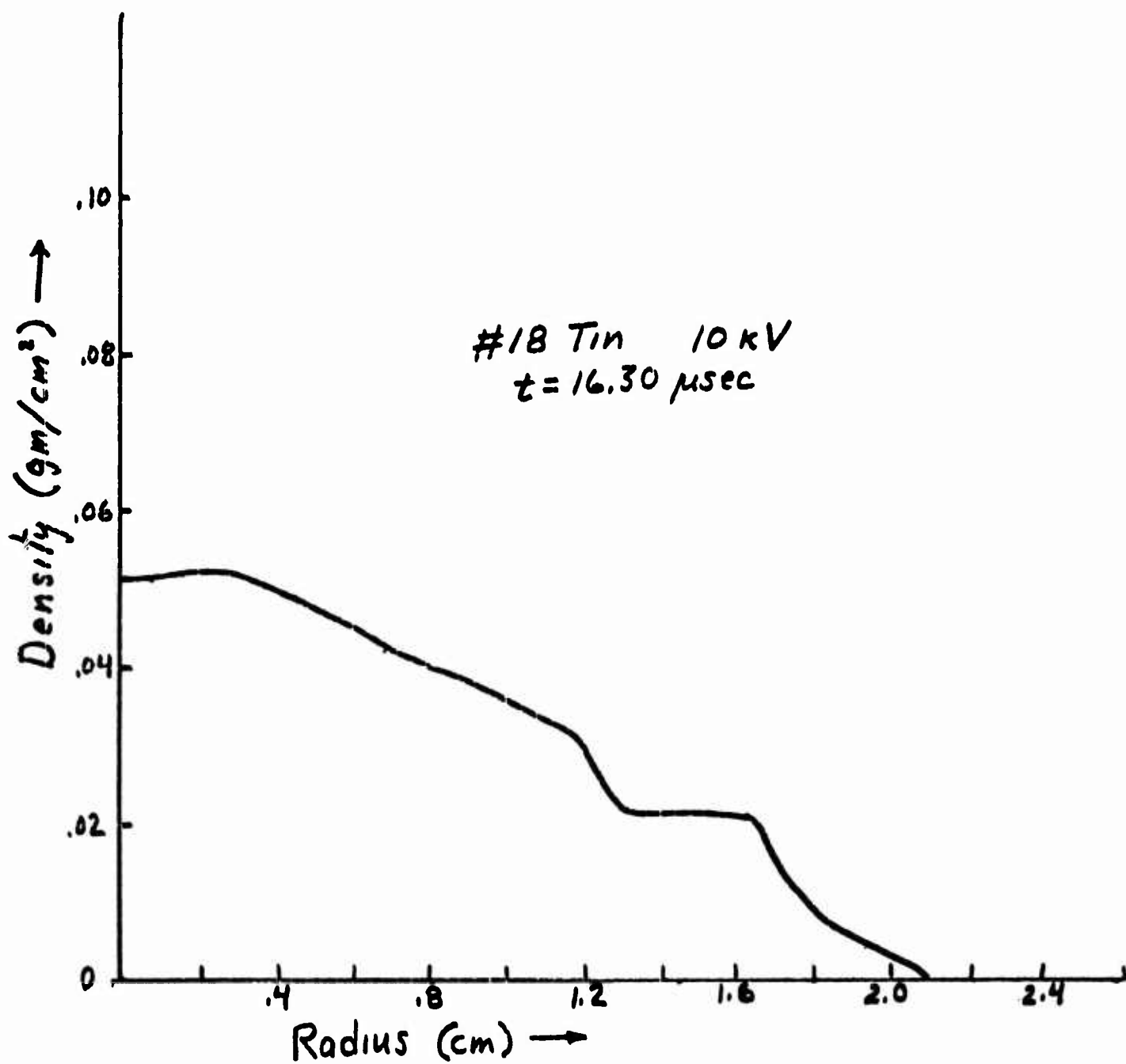


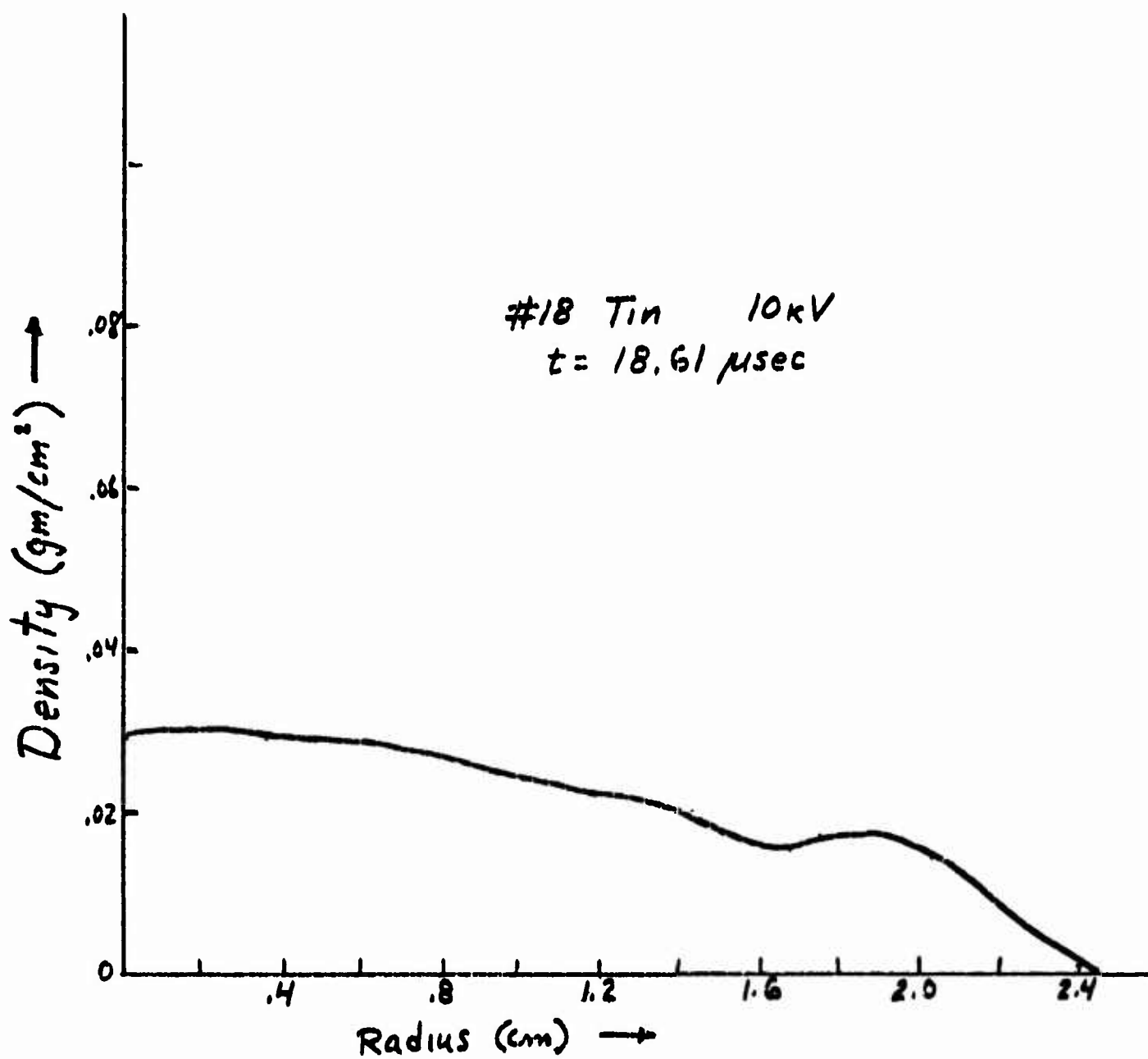


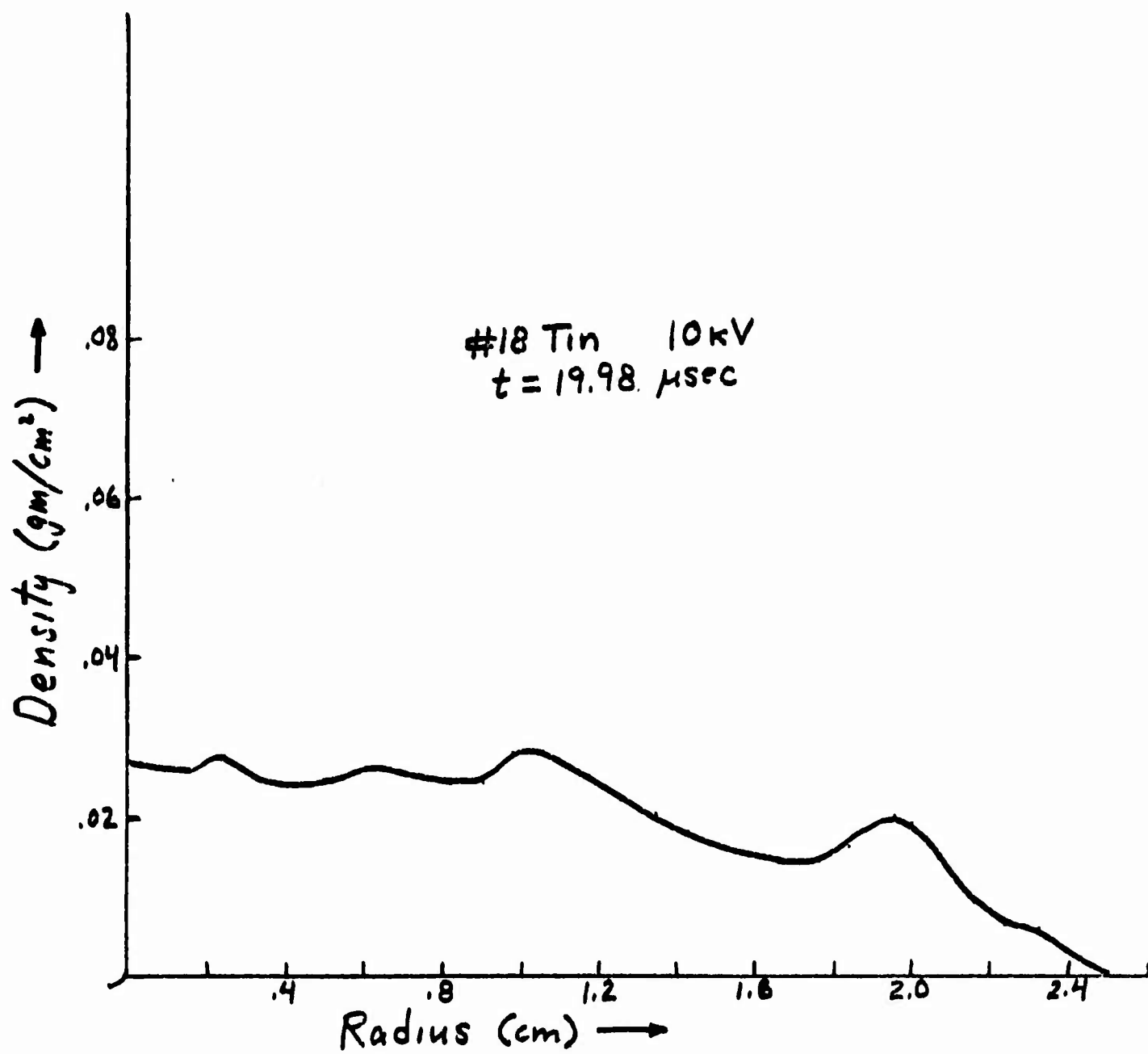


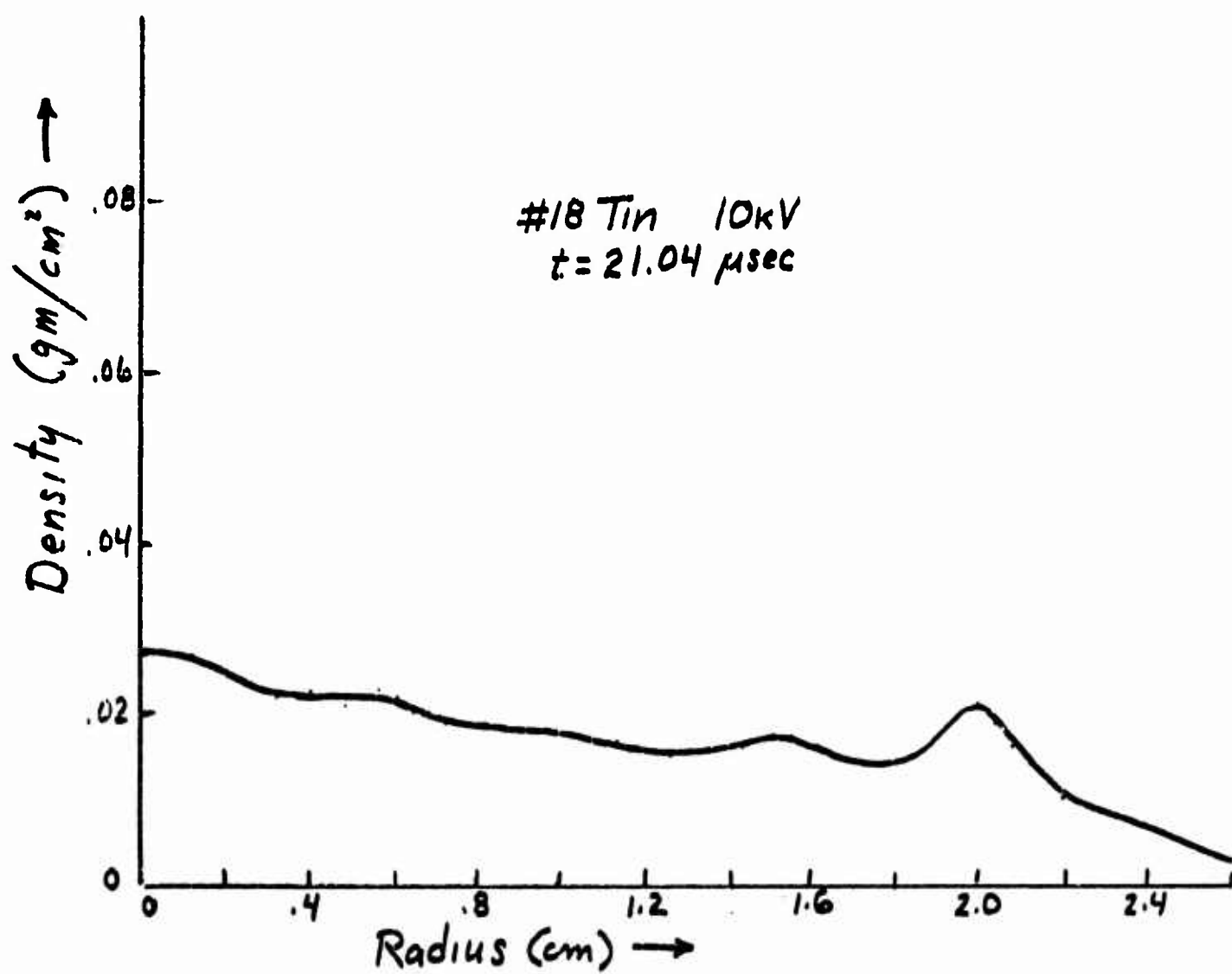












Page 115

APPENDIX IV

Equipment Setup For Vapor Density Measurements

EQUIPMENT SETUP

The experimental setup involved a twin flash X-ray unit (two flash X-ray heads), a capacitor discharge system (45 microfarads), Faraday shutter camera (Rapatron), and two oscilloscopes to monitor the current and timing pulses, as well as appropriate delay lines for various units. The block diagram is seen in figure 2. When all units have been charged to their respective voltages, a manual trigger produces a pulse which first triggers the capacitor bank, exploding the wire, then a delay line is used to trigger the X-ray unit at definite time increments with respect to the beginning of current through the wire. A similar delay is used for the pulsed optic camera. The current is measured by a calibrated Rogovski coil-RC integrator unit. Figure 1 shows the physical alignment. In A, the two X-ray tubes can be seen at "8 O'Clock" and "12 O'Clock." The Faraday shutter camera is situated at "4 O'Clock." The capacitor bank, wire holders, wires, and film cassettes are in the center of the picture. In figure 1-B, an integrated light photo of the exploding wire shows the wire site, as well as the extent of the explosion in air at 10 kV.

LIST OF ILLUSTRATIONS

- Figure 1 (A) The experimental setup for obtaining vapor density radiographs. To the left and also above are the two x-ray tubes. In the foreground the optical camera. The wire, film cassettes, and capacitor bank are in the center.
- (B) An integrated light photo of a wire explosion in air.
- Figure 2 The block diagram of the experimental setup for obtaining instantaneous density measurements for an exploding wire.

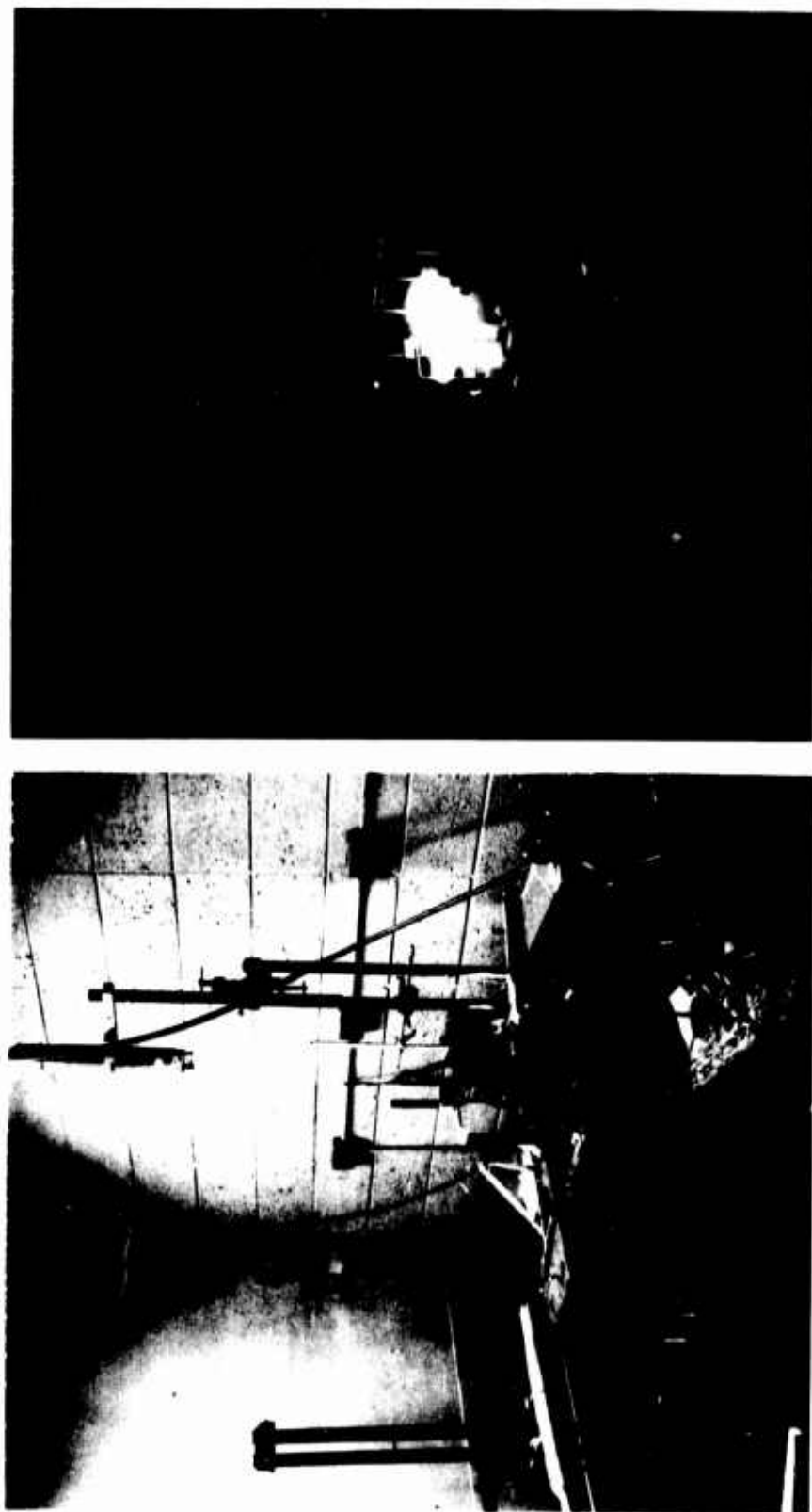


Figure 1. (A) The experimental setup for obtaining vapor density radiographs. To the left and also above are the two x-ray tubes. In the foreground, the optical camera. The wire, film cassettes, and capacitor bank are in the center.
(B) An integrated light photo of a wire explosion in air.

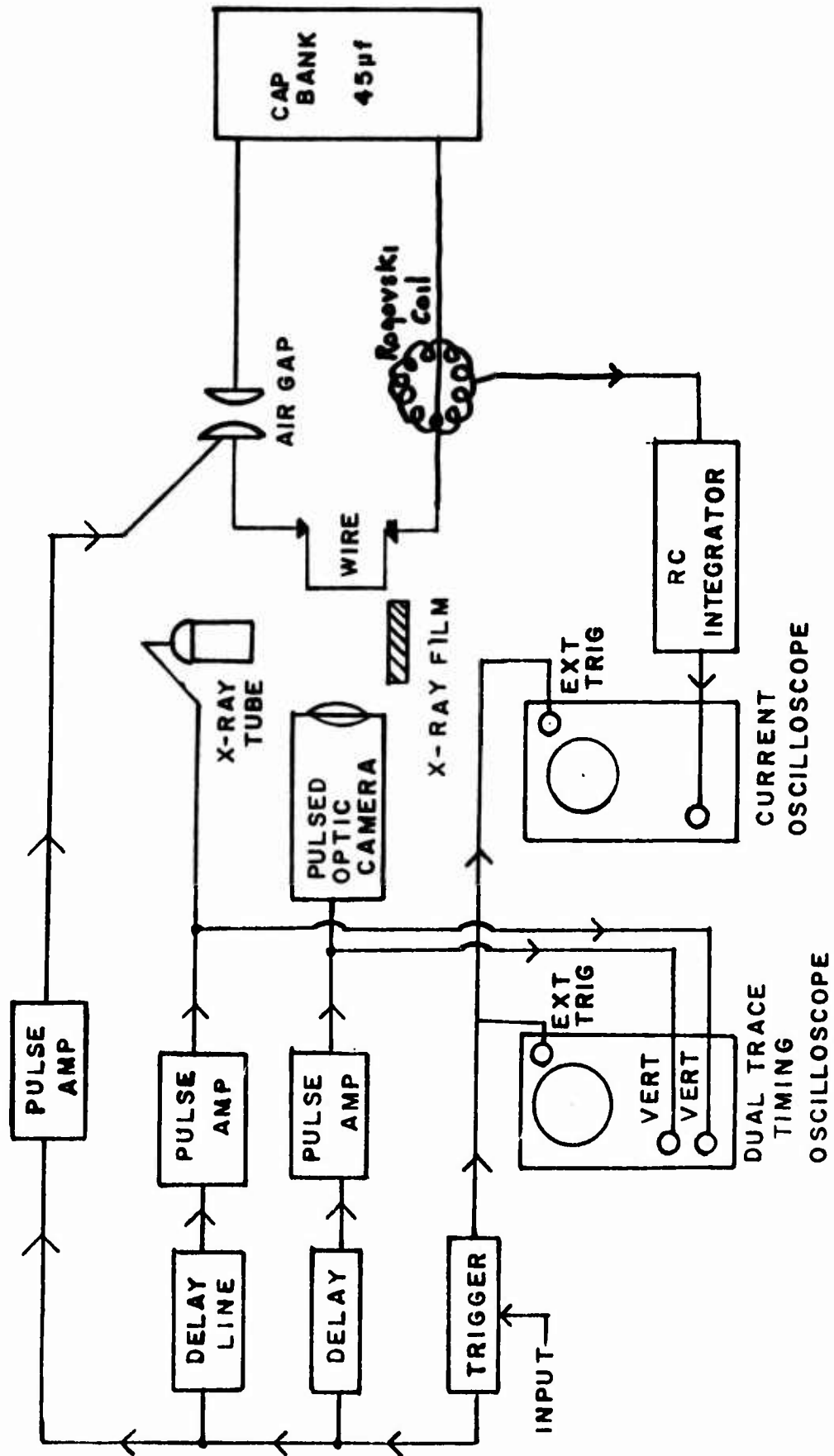


Figure 2 The block diagram of the experimental setup for obtaining instantaneous density measurements for an exploding wire.

Page 120

APPENDIX V

RELATED CONTRACTS AND PUBLICATIONS

APPENDIX V Related Contracts and Publications

1. T. Korneff et al, "Study of High Energy, High Density Discharges and High Temperature Measurements as Applied to Exploding Wires", AFCRL-67-0276, Final Report, May 1967.
2. Chern, D. C. and Korneff, T. "Current Distribution for Wire Exploded in Vacuo, Exploding Wires Vol. 4, Plenum Press, 1968.
3. Chern, D. C. and Korneff, T. "Current Distribution for Wire Exploded in Vacuum" AFCRL-68-0328, Scientific Report No. 1, May, 1968.
4. Chern, D. C., "Current Distribution for Wire Exploded in Vacuo", Master's Thesis, Temple University, 1967.
5. Goronkin, H., "Striations in EWP", AFCRL-68-0671, Scientific Report No. 2, Oct, 1968.
6. Goronkin, H. "Striations in Fast Wire Explosions", J. Appl. Phys. 39 11, Oct., 1968.
7. Korneff, T. and Chace, W., "A Study of Exploding Wires by X-rays Directed Parallel to the Wire Axis", Paper presented at APS meeting, Washington, D. C., 1969.
8. Korneff, T. and Chace, W., "A Method of Determining Density-Radius Relations During Wire Explosions", Unpublished. Submitted to Rev. Sci. Instr., March, 1970.
9. Korneff, T., "The Density of Copper and Tin Vapor as a Function of Time in EWP Experiments", Paper presented at APS meeting, Chicago, Jan., 1970.
10. Bohn, J. L. "Research Directed Toward the Attainment and Utilization of High Temperatures-Spectrophotometric Determination of High Temperatures" Scientific Report, AFCRC Contract No. 19(604)-3076, Nov. 1960.
11. Zatzick, M.R. "Instrumentation for Geophysics and Astrophysics" AFCRC-TR-58-275, No. 11, Sept. 1959.

unclassified

Security Classification

DOCUMENT CONTROL DATA - R&D

(Security classification of title, body of abstract and indexing annotation must be entered when the overall report is classified)

1. ORIGINATING ACTIVITY (Corporate author) Temple University of the Commonwealth System of Higher Education Philadelphia, Pennsylvania 19122		2a. REPORT SECURITY CLASSIFICATION unclassified	
		2b. GROUP	
3. REPORT TITLE EXPLODING WIRE PHENOMENA			
4. DESCRIPTIVE NOTES (Type of report and inclusive dates) Scientific. Final. 1 March, 1967 through 28 February, 1970. Approved 28 April 1970			
5. AUTHOR(S) (Last name, first name, initial) Theodore Korneff William Simmons Herbert Goronkin			
6. REPORT DATE 31 March, 1970		7a. TOTAL NO. OF PAGES 122	7b. NO. OF REFS 33
8a. CONTRACT OR GRANT NO. F19628-67-C-0250		9a. ORIGINATOR'S REPORT NUMBER(S)	
b. Project, Task, Work Unit Nos. 8608-04-01			
c. DoD Element 61102F		9b. OTHER REPORT NO(S) (Any other numbers that may be assigned this report) AFCRL-70-0224	
d. DoD Subelement 681311			
10. AVAILABILITY/LIMITATION NOTICES 1 - This document has been approved for public release and sale; its distribution is unlimited.			
11. SUPPLEMENTARY NOTES TECH, OTHERS		12. SPONSORING MILITARY ACTIVITY Air Force Cambridge Research Laboratories (CRF) L. G. Hanscom Field Bedford, Massachusetts 01730	
13. ABSTRACT This report describes: A. Experiments to determine the shunting effect of occluded and self generated vapor produced by an exploding wire in a vacuum. B. The investigation of the striation mechanism in exploding wires. (These striations have been examined by high speed sequential framing camera to see if they have an axial drift.) C. Calculations on the order of magnitude of the Hall energy. (Results show that for a given sample, about 13% more energy is required to melt the sample than is accounted for in simple thermodynamic arguments.) D. The development of an experimental flash x-ray technique for determining the instantaneous density of the vapor produced by an exploding wire. E. The development of a three-color optical pyrometer with fast response time. (The unit, in breadboard form, has been calibrated, and used to obtain preliminary results from exploding wires. The results are expressed in the form of a trace on a cathode ray oscilloscope, whose vertical displacement is proportional to the temperature.)			

unclassified
Security Classification

14 KEY WORDS	LINK A		LINK B		LINK C	
	ROLE	WT	ROLE	WT	ROLE	WT
Exploding Wire Hall Effect Pyrometry Radiograph, Flash Striations in EWP X-rays, Flash						

unclassified
Security Classification